Marie Skłodowska-Curie Actions
(MSCA) Innovative Training Networks
(ITN) H2020-MSCA-ITN-2019

861079 – NextMGT

(Next Generation of Micro Gas Turbines for High Efficiency, Low Emissions and Fuel Flexibility)

Report on performance optimisation of MGTs

Deliverable No. 15
Relative number 1.2
Public deliverable

Date: 20/12/2022
Lead Beneficiary: AUTH

This project has received funding from the European Union's Horizon 2020 research and innovation programme under Marie Sklodowska-Curie grant agreement No 861079

Contents

Executive summary

This deliverable summarizes the work performed within “NextMGT” project until month 36 (December 2022), and more specifically it covers the progress of work package one (WP1) regarding the performance optimization of micro-gas turbines. “NextMGT” is a European funded project that focuses on the development of the technical expertise and scientific knowledge which enables a substantial enhancement in understanding the fundamental design and operation aspects of next generation micro-gas turbines towards to a successful commercialisation.
In the first chapter, an introductory literature review relevant to each early-stage researcher’s (ESR’s) scientific topic is presented.
The second and third chapters focus on the optimisation methods in component-level and system-level respectively that have been applied by each ESR of WP1 along with the significant contribution of ESR 8 from WP2.
Finally, in chapter 4, the most spectacular outcomes from each ESR are analysed together with the scheduled future work.

1. Micro gas turbines – Operation and developments

Micro gas turbines (mGTs) are small devices converting the energy stored in the fuel into mechanical energy, which drives an electrical generator through a shaft assembly. Even though, no formal terminology exists, two criteria are usually used to include the term "micro" in front of a Gas Turbine (1) the electrical power output of the machine ranges between 15 and 500kWe [1-3] and (2) the machine needs to run at high rotational speed up to 120, 000 rpm [4]. Nevertheless, earlier in the development of mGTs, some authors like Pilavachi [5] proposed a dissociation between the microturbines (< 150kWe) and the mini turbines (< 1MWe). Also, the second criterion used for the terminology is of minor importance compared to the nominal power requirement.

Modern mGT systems, utilized in decentralized power generation, typically use the recuperated Brayton cycles. The layout of these cycles is presented in Fig. 1.1. There, fresh ambient air first undergoes compression through a centrifugal compressor component [6]. The compression ratio is usually around $3 - 5$ [7] even in two stages layout [8]. Then, the compressed air is preheated before entering the combustion chamber through the heat exchanger which recovers a substantial amount of energy from the exhaust gas. The recuperator is one of the most important components of the mGT as it almost doubles the efficiency compared to a simple Brayton cycle layout [7]. The combustion chamber is a lean pre-mix type [9]. Inside this component, the preheated compressed air is mixed with a fuel (mixtures of natural gas normally in gaseous form). The highly diluted mixture with a fuel/air ratio $f < 0.01$ for rich natural gas corresponds to a fuel/air equivalence ratio < 0.15 [10]. The turbine inlet temperature (TIT) is far lower compared to large gas turbines usually below 950°C [7] because cooling requirements (e.g. blade cooling) are both economically and technically difficult to achieve at the mGT scale [11]. The flue gases are expanded through a radial turbine where the required mechanical and electrical loads are produced. The temperature drop after the expansion is generally not superior to 300°C and the turbine outlet temperature (TOT) is usually limited to a maximum of 650°C, to protect the materials of the recuperator hot side. The expanded gas passes the recuperator hot leg to achieve waste heat recovery. So finally, the exhaust gas temperature is between 250°C and 300°C [7].

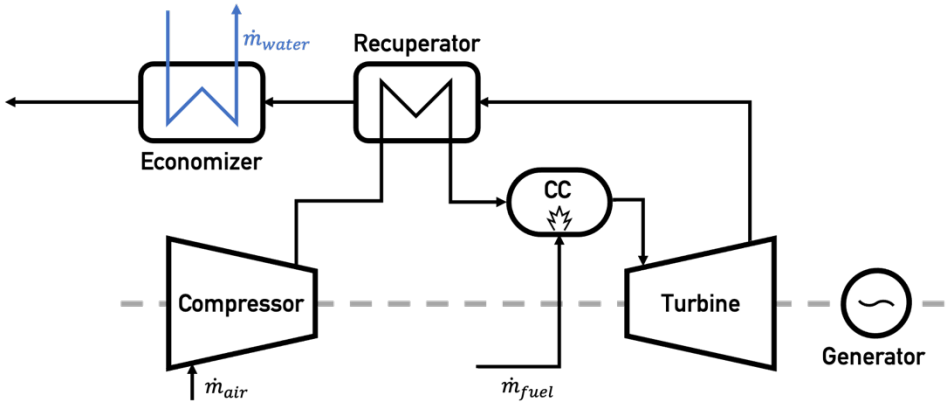

Figure 1.1 - Recuperated Brayton cycle configuration which is the typical layout of mGTs

mGTs present numerous advantages over their main competitor, the Internal Combustion Engines (ICE). The ones that are regularly reported in the literature can be listed below:

- **A suitable candidate for small-scale Combined Heat and Power (CHP) applications:** As the waste heat is stored in the exhaust gas and has a relatively high temperature (between 250°C and 300°C [7]), mGT is an excellent candidate for small-scale CHP. In the ICE, the waste heat is split between the exhaust gas, the cooling water and the lubrication oil. As a result, it loses the potential to heat water through an economizer [12]. It is reported that small-scale CHP units that utilize mGT as a prime mover typically achieve more than 80% total efficiency (30% electricity production, 50% heat production) [13].
- **Low pollutants emissions:** Turbec, which first manufactured the T100 engine (before Ansaldo Energia acquired the rights of this machine), announced emissions [NOx] @15%O2 < 15ppm and [CO] @15%O2 < 15ppm at full load [14]. These performances were assessed by other

authors for natural gas [15], but also for alternative biomass-derived low calorific fuels [16].

- **Fuel flexibility:** Numerous studies have shown that mGT is capable to run with a wide range of alternative fuels. Theoretical and experimental studies were conducted on the control of externally fired mGTs (EFmGTs). Although "dirty fuels", such as coal and biomass, cannot all be considered renewable fuels, EFmGTs allow us to exploit them without the need for gasification. Their works aimed at limiting high-risk issues of thermal stresses on the exhaust side of the recuperator, that appear with the use of external combustion and dirty fuels. Nevertheless, the poor technical and economical performances have limited their diffusion in the market, despite their ability to use renewable fuels, such as biomass [17,18]. More recent works of Calabria et al. studied the combustion process in mGTs with Computational Fluid Dynamics (CFD) at part load operation using fuel with synthetic gas (syngas) and hydrogen-methane blends, in comparison with natural gas. They showed that low loads and low calorific fuels generate stability and emissions issues in the combustion and also suggested a design to enable the utilization of liquid fuels [19].

1.1. Alternative and hybrid cycles

In the current chapter, it is also necessary to mention the growing interest in the employment of mGTs in alternative and hybrid Brayton cycles which are applied in distributed power generation.

1.1.1. 2-spool mGT

Jaatinen-Värri et al. proposed a design and a control strategy for a two-spool 400kW mGT. This application presented performance comparable to ICEs with increased efficiency even in part load. The inclusion of an intercooler between the two Compressors improved the efficiency of the High-Pressure Compressor (Fig. 1.2). Moreover, the two generators of this cycle are not mounted in the same shaft which allowed the engine to operate with different shaft speeds and increased the electrical efficiency at part-load conditions [8,20].

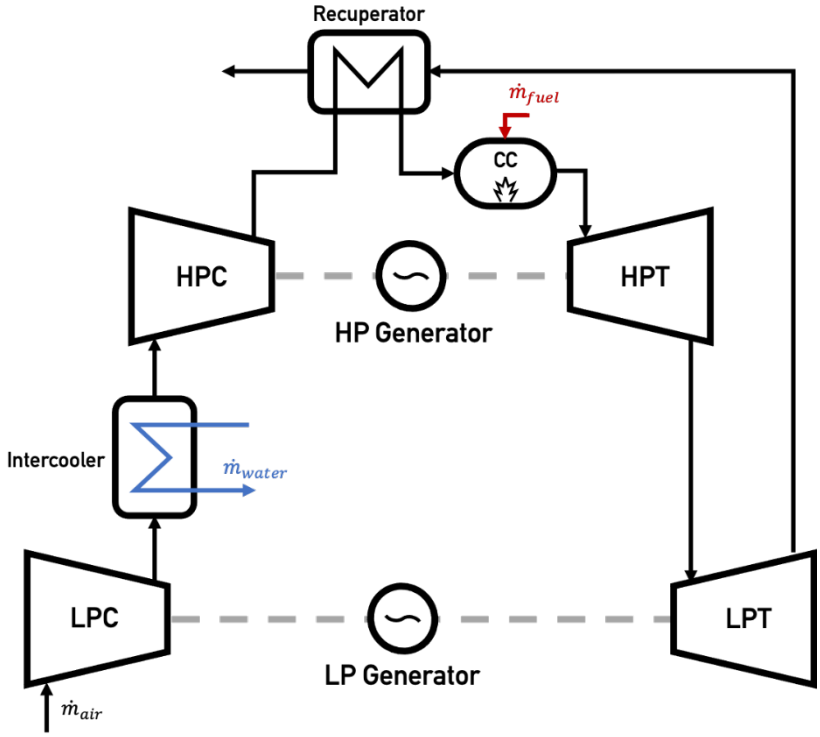

Figure 1.2 - Schematic representation of the 2-spool mGT. The main differences form a typical mGT is the inclusion of an Intercooler and the Low-Pressure (LP) and High-Pressure (HP) shafts.

1.1.2. Inverted Brayton Cycle mGT

The main issue in manufacturing a unit that produces relatively low electrical power (in the range of 1 to 10kWe) is the increased seal and tip leakages and the difficulty to achieve high pressure ratios. An alternative mGT cycle that could present some solutions at low power demands is the Inverted Brayton Cycle (IBC). As it is shown in Fig. 1.3, the components are relatively identical to those used in a BC but the order in which the flow passes through each component is different. Instead of firstly being compressed to a higher pressure than the ambient, the flow goes directly through the Combustion Chamber (CC) at ambient conditions. Then follows the expansion in the turbine. Hence the working pressure of this cycle is below the atmospheric. The above-mentioned drawbacks in downsizing a Gas Turbine (GT) are could theoretically be avoided in an IBC based system. The inverted configuration allows to avoid these typical losses when downsizing a conventional mGT as they depend mainly on the volumetric flows and the low pressure level of the IBC results in high volumetric gas flows. The volumetric flows of IBC stay constant when downsizing from a BC to an IBC while the mass flow varies depending on the pressure level [22]. Therefore, German Aerospace Centre (DLR) numerically and experimentally investigated this technology [22,23] Agelidou et al. Presented the thermodynamic feasibility of inverting a conventional mGT to be operated in IBC mode by demonstrating an operational

test rig. However, it is shown that the mechanical and heat losses have a high influence on the performance and economic efficiency of the system [23].

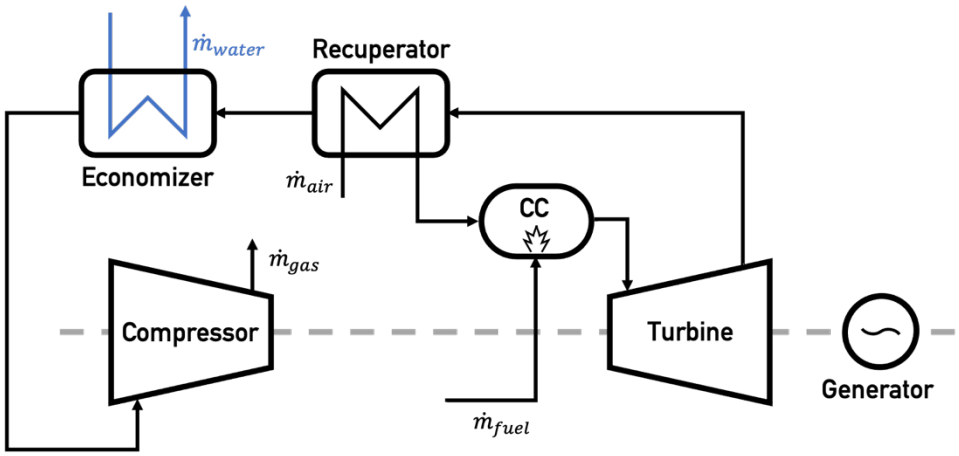

Figure 1.3 - Inverted Brayton Cycle configuration of an mGT. The air firstly passes through the CC and the exhaust gases leave the cycle at the Compressor outlet.

1.1.3. micro Humid Air Turbine (mHAT)

A prototype of the mHAT has been constructed at VUB, Belgium [24]. The concept of this cycle seems very appealing to increase the efficiency of the CHP at periods of low heat demand due to its simplistic implementation. Different concepts of humidification and injection locations (i.e. before or after compressor, directly inside combustion chamber) have been applied and the inclusion of an air saturator at the compressor outlet was finally adopted [2, 15]. The main advantage of the mHAT cycle is the ability to exploit larger waste heat from the recuperator compared to an engine operated with dry air. Mixing the air with water before the recuperator decreases substantially the compressor outlet temperature which increases the available waste heat that can be used. Secondly, the massflow of the gases after the injection is increased which results to lower work demand from the compressor at constant power. Figure 1.4 shows the layout of the mHAT prototype constructed at VUB. De Paepe proved the potential of mHAT as more than 4% absolute increase in efficiency was experimentally observed [15].

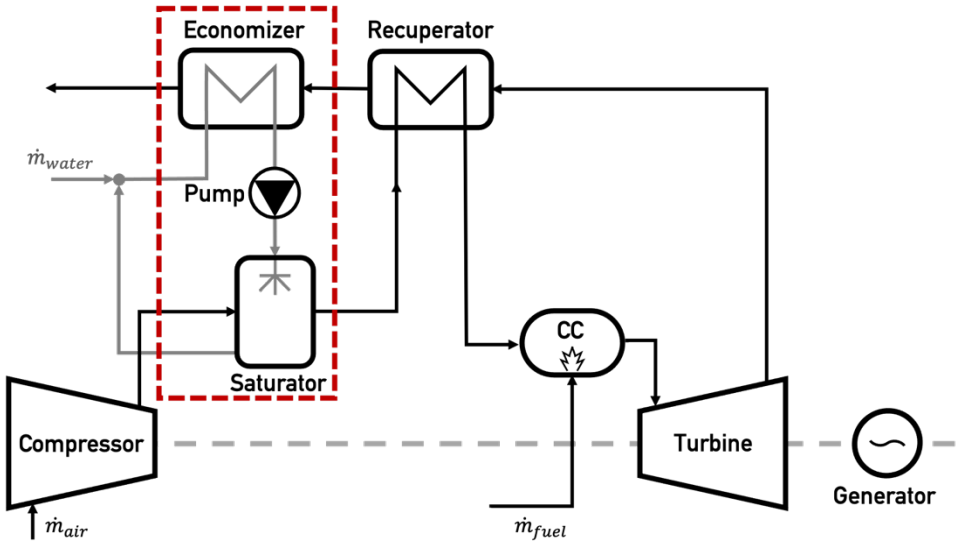

Figure 1.4 - The layout of the mHAT cycle installed at VUB, Belgium. The new components are the the Pump which recirculates the injected water and the saturator that mixes saturated steam with the working fluid.

1.2. Turbomachinery components

1.2.1 Introduction

The compressor is one of the most significant parts of a turbomachinery system. In axial compressors, the higher the required pressure ratio the higher the number of compressor stages. Decreasing the stage number by raising the stage pressure ratio has always been a research object while the main goal is to build a smaller, compact and high-performance compressor stage. A potential compressor configuration, which meets the aforementioned requirements, could be a centrifugal / radial compressor. The pressure rise in a radial compressor is done because of the large radius change of the fluid between inlet and outlet. The pressure ratio of a single stage centrifugal compressor corresponds to several axial compressor stages. However, the high turn of the flow at the impeller exits and the existence of the diffuser, to recover the flow dynamic pressure, create high losses. Thus, a typical centrifugal compressor has lower adiabatic efficiency compared to an axial one. This disadvantage is more dominant when the application is small gas turbine applications like micro gas turbines.

1.2.2 Centrifugal Compressor Performance

The impeller is the main part of the compressor which transfers energy to the fluid. The fluid passes through the inlet, which is located at a specific radius, and leaves the impeller at a different one. Depending on the given external torque, the rotor changes the fluid momentum. This section provides all the required performance parameters of a centrifugal compressor.

Slip factor

One of the most significant performance parameters of a centrifugal rotor is the slip factor. It expresses the amount of energy that an impeller can transfer to the fluid. Considering the ideal case of a rotor with infinite number of thin blades, the flow will exit the passage following the impeller blade angle. However, this does not happen in reality. The rotor has a specific number of blades with specific thickness. Thus, the fluid leaves the rotor at an angle which is different from the blade one. Figure 1.5 shows how the fluid deviates from the ideal case.

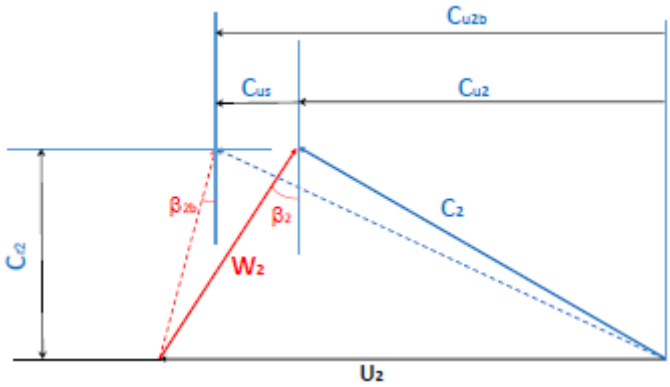

Figure 1.5 Velocity deviation at impeller outlet

Slip factor expresses the flow deviation and can be calculated by the following equation:

$$\sigma = \frac{C_{U2}}{C_{U2b}} \quad (1.1)$$

C_{U2} and C_{U2b} are the tangential component of the outlet velocity and the tangerial velocity, and they are related to the relative flow angle and relative blade angle, respectively. Based on figure 1.5 and implementing some geometric relations, the following equation can be resulting.

$$\sigma = 1 - \frac{C_{US}}{C_{U2b}} (1.2)$$

Wiesner et al. [13] proposed an empirical correlation for slip velocity.

$$C_{US} = \frac{U_{2\sqrt{cos\beta_{2b}}}}{Z^{0.7}} \quad (1.3)$$

The slip factor can be defined as:

$$\sigma = \frac{\sqrt{cos\beta_{2b}}}{Z^{0.7}(1-\varphi_2 tan\beta_{2b})} \quad (1.4)$$

Pressure Ratio

The compressor performance can be evaluated using the pressure ratio parameter. It expresses the ratio between the outlet and inlet pressure and based on the thermodynamics can be defined as:

$$PR = \frac{P_{02}}{P_{01}} = \left(\frac{T_{02is}}{T01}\right)^{\frac{\gamma}{\gamma-1}} \quad (1.5)$$

Flow coefficient

The actual mass flow rate of a given impeller at a known rotational speed can be expressed by flow coefficient.

$$\varphi = \frac{\dot{m}}{\rho\, \omega\, \pi\, r_2^3} \quad (1.6)$$

Efficiency

To take account the divergence of the iso-pressure lines, polytropic efficiency is used to evaluate the compressor performance. This is a comparison between the real enthalpy rise and the ideal one. The following equation calculates the polytropic efficiency.

$$\eta_P = \frac{\ln\left(\frac{P_2}{P_1}\right)}{\ln\left(\frac{T_2}{T_1}\right)} \frac{\gamma-1}{\gamma} \quad (1.7)$$

1.2.3 Motivation and State of the Art

Designing a new generation compressor for a micro gas turbine (mGT) generates many challenges. Keeping the mass flow rate constant while decreasing the geometrical dimensions of the component makes the mGT operate at a higher rotational speed. This results in the Reynolds number decreasing, which in combination with the higher ratio of boundary layer thickness over hydraulic diameter between two blades, increases the vane blockage. The immediate effects of this rise are a higher total pressure loss and a reduced pressure recovery. Moreover, the 100% increase in relative tip clearance and the low performance of the diffuser in low Reynolds number flows reduces even more the overall efficiency of the compressor stage.

Previous works shown that contra-rotating configuration have some advantages and can be a potential solution on the current challenges. Generally, a counterrotating turbomachinery improves the pressure ratio and at the same time decreases the weight and the size. This configuration is widely implemented in axial compressor, however the works in centrifugal rotors are limited. Thus, implementing the idea of designing a contra-rotating radial compressor can shape and affect the new generation of compressors. In this work, the design procedure of a contra-rotating radial compressor is described in detailed. Numerical analysis are conducted in order to assess the proposed design. The produced results we commented in order to understand the advantages and disadvantages of this novel configuration.

1.3. System integration and monitoring

1.3.1. Introduction

To provide secure, reliable, clean, and sustainable energy, a broad portfolio of energy conversion and storage technologies will be required. This is likely to include nuclear power generation, concentrated-solar power plants, and hydrogen power plants, along with new technologies improving overall energy efficiency, as well as continued use of fossil fuels, ultimately with carbon capture and storage. Due to the inevitable phases of low energy input from renewables, thermal power plants will be suitable for load control and backup power if sufficient storage capabilities are not available. The fossil power stations will be utilized only for the periods when wind and sun are absent [25]. Utilizing large thermal power plants for standby functions will be accompanied by considerable operation costs.

Currently, the energy supplement in the world is dominated by fossil fuels and there are numerous functioning power plants and substantial fuel resources available. Therefore, even though they are the undesired sources of long-term ambitions of GHG reduction, it seems impossible for them to be phased out by the mid-century. According to recent research, 37% of global CO_2 emissions are attributed to some industrial sectors such as iron, steel, and cement sectors. Therefore, fossil fuel-based power plants are difficult to eliminate [26]. Consequently, it is important to develop technologies that permit fossil-fueled plants to operate as low-emission power generators.

Another fuel resource for power plants is biomass, the most important renewable energy source which covered nearly 60% of renewable-based power production in Europe in 2016 [27]. On average, in industrialized countries, biomass contributes about 9–13% to the total energy supplies, but in developing countries, the proportion is less than 7% [28]. The electricity and heat producers of future power production systems must be able to function with carbon-neutral or carbon-free fuels, such as biofuels, hydrogen, or ammonia. While redeveloping large-scale fuel-flexible power plants is expensive, building small-scale power generation technologies which can operate with a range of fuels are technically and economically feasible.

It is anticipated that the future structure of power generation will appear in a similar layout as depicted in Figure 1.6. The power supply system will be a combination of big and small generators, where the small ones supply local power demands, and the big stations are for the system backup and are equipped with carbon capture and storage.

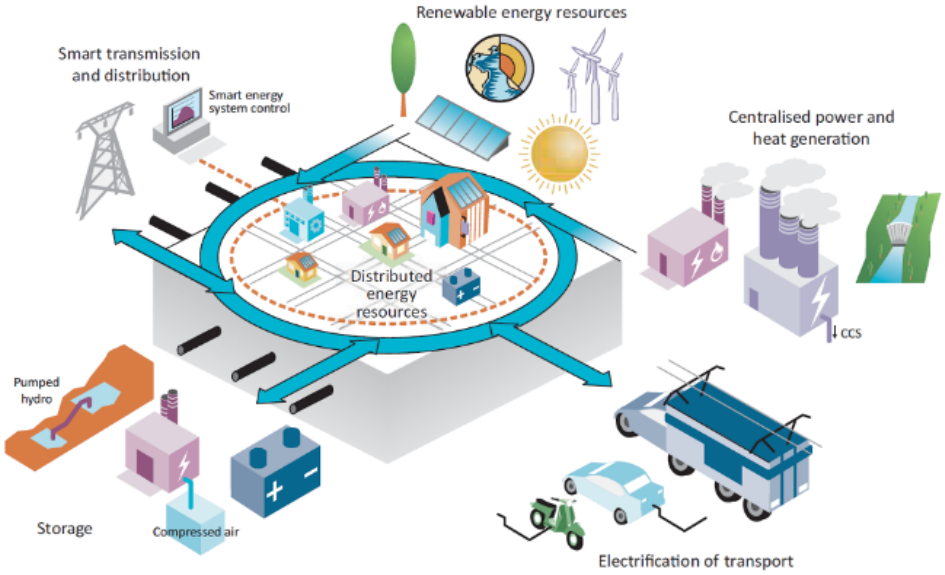

Figure 1.6 – The integrated and intelligent electricity system of the future [29]

In the new scheme of power generation, the local power supply is called a microgrid (MG) which binds together to organize the local balance of the power system. If a microgrid cannot achieve the balance, then it will get power from the neighbor microgrid or the strong backup system to assure constant frequency [30].

Figure 1.6 shows a “smart grid”, a combination of local networks with active consumers and

small storage, a strong backbone network, and powerful generators. The buildings, as one of the main consumers of electricity in today's platform, will play an active role in the system, where they become flexible storage or even a supplier for the grid [31].

Microgrids are a group of interconnected loads and distributed energy resources within defined electrical boundaries, which act as a single controllable entity with respect to the grid. It can be connected and disconnected from the grid since it is capable of operating in both grid-connected and islanded modes [32]. Microgrids have been researched for decades [33], however, increasing penetration of distributed energy resources (DERs) into the existing power sector is raising the motive to develop advanced technologies for MG power generation units [34]. Besides the global warming effects, the increasing penetration of DER is attributed to fossil fuel shortage and political instability in the major energy-supplying countries [32]. Moreover, production costs for developing distributed energy resources declined due to technological improvements, hence the renewable energy sector has witnessed a boom in the past decade [32]. In the decentralized scheme, low power loss in the transportation of electricity due to the proximity of the production unit to the consumer is another attractive feature promoting it. Advanced MG systems will improve energy security and provide power that is efficient, reliable, and clean [35]. The international energy policies toward less GHG emissions are other key drivers for promoting renewable energy targets and DER, changing the MG role from a secondary energy source to a primary energy supply [33].

The rapidly increasing trend of microgrid integration into the electricity grid presents technical barriers and problems such as voltage stability, distribution system operation, control, and protection [36]. Technical challenges have been investigated for over a decade, and now can offer a stable and smoother energy supply [32]. However, the operation and maintenance of MG power units show improvement prospects for more reliable power generation.

1.3.2. Changing Role of Electric Power

The main sectors of the final energy consumption of EU-27 in 2018 were in the areas of residential (26.1%), transport (30.5%), and industry (25.8%) [37]. Figure 1.7 illustrates the share of different sectors in final energy consumption for EU-27 countries in 2018. The urbanization of the world is in progress which has a significant influence on energy demand. In developing countries, today more than 50% of the population are living in urban areas (Table 1.1), whereas in industrialized regions such as Europe already 77.5% has been reached. In industrialized countries, the electrification rate is more than 95% in urban areas (100% in the EU), but it is only about 60 to 70% in rural areas. One can say that urbanization is linked to electrification [38].

Table 1.1 – Urbanization rate in percent of the total population in developing countries and industrialized countries [38].

	1950	1960	1970	1980	1990	2000	2010	2020	2030	2040
DC	18.0	21.7	25.3	29.6	35.1	40.2	45.3	50.5	56.0	61.6
IC	52.5	58.7	64.6	68.8	71.2	73.1	75.0	77.5	80.6	83.5

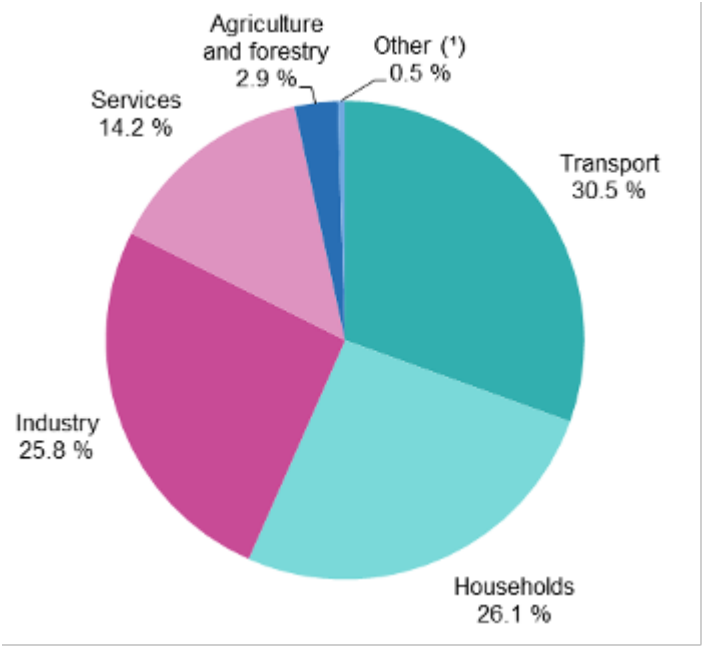

Figure 1.7 – Final energy consumption by sector, EU-27, 2018 [37]

Electricity represents clean energy and is the ideal form of supply for densely populated urban areas. The building sector is crucial for achieving the EU's energy and environmental goals. The EU "directive on the energy performance of buildings" provides the guidelines for the reduction of total energy consumption in the residential sector in the EU [39]. The aim of the directive is a "low-energy building" with a very high energy performance which improves the higher life quality of residents with additional economic advantages [40].

The microgrid concept for urban and residential households is a suitable solution for an increasing urban population, especially for operation in cogeneration mode [35]. A combined heat and power (CHP) generation mode of microgrids is an efficient solution for recovering the residual heat in the power generation unit to be exploited in proper form by the end-user. In centralized power generation mode, a part of the electrical power that is delivered to the residential sector is transformed and expended for heating or cooling purposes. Cogeneration units in DEG networks avoid inefficient heat to power and again power to heat conversion deficiencies.

1.3.3. Micro Turbine's Place in Future Smart Microgrid

Micro gas turbines provide a reliable and cost-effective power source with a quick load-following ability which can respond to demand peaks and compensate for intermittent renewable sources when they are not available. mGT units can work as a system together with renewables, or function as a stand-alone unit in off-grid operations. mGTs are fuel flexible which can offer cost-effective electricity and heat production, especially with fluctuating fuel prices. As a small power plant utilized in private households or public buildings, mGTs offer low noise, easy operation, and highly reliable power generation units, which are the most important requirements for decentralized energy systems.

Combined heat and power (CHP) systems based on mGTs have a higher share than micro power generators in the market due to the decentralized foundation of heat production. Moreover, cogeneration of heat and power increases thermal energy conversion efficiency and reduces costs.

All these features are privileged in the horizon of energy transition that is the carbon-free modern energy grid. The technology underlying micro gas turbines offer hybridization with renewable energy sources, flexibility in operations and fuel, and promising low-emission solutions that align with environmental concerns. However, there is a continuous need for improving energy efficiency as coupled with a pressing urge for reduced emissions.

To maintain desired performance and safe operation, effective control of system operating parameters during engine lifetime is essential. The operational performance of the engine can be deteriorated gradually or abruptly due to several causes. In this situation, the control methodology originally designed for the healthy engine may not be suitable anymore, depending on the level of

deterioration. An adequate monitoring and diagnostic program developed to constantly analyze the condition and performance of the engine will result in reducing operating and maintenance costs and longer component and engine life. Prediction of faults can change the maintenance strategy from a fixed prescheduled model to a condition-based approach and decrease the maintenance cost.

Realizing the actual health condition of components of the engine, an adaptive control scheme can be employed to compensate for the effect of deteriorations. Components degradation level is assessed by the variations in the available measurements; then the information about engine health condition is employed to adopt modified control strategies that guarantee a safe operation and limit the reduction in performance efficiency.

Three main platforms are required to accomplish the goal of improving the performance of micro gas turbines by monitoring their condition: to develop a predictive model of the mGT engine which will be used as a reference engine simulator, a condition monitoring tool to identify any deviations of engine performance from the reference engine, and an optimizer to modify the operational strategy for better performance. In this report first, the motive and scope of this work are described in chapter 1, and in the second chapter, an overview of related studies from the literature is presented.

Micro gas turbines provide a reliable and cost-effective power source with a quick load-following ability which can respond to demand peaks and compensate for intermittent renewable sources when they are not available. mGT units can work as a system together with renewables, or function as a stand-alone unit in off-grid operations. mGTs are fuel flexible which can offer cost-effective electricity and heat production, especially with fluctuating fuel prices. As a small power plant that is utilized in private households or public buildings, mGTs offer low noise, easy operation, and highly reliable power generation units, which are the most important requirements for decentralized energy systems.

Combined heat and power systems based on mGTs have a higher share than micropower generators in the market due to the decentralized foundation of heat production. Moreover, the cogeneration of heat and power increases thermal energy conversion efficiency and reduces costs.

The continuous development and implementation of diagnostics can significantly reduce both the financial losses that are caused by system breakdown and the costs that are attributed to unnecessary repair and replacement of components. Moreover, the condition monitoring assessments could be provided to an optimizer that changes the operational strategy of the mGT controller, seeking higher efficiencies, a longer lifetime, or both. The integration of mGT cycle data with smart tools based on AI techniques can potentially increase the useful operational hours and thus higher investment returns. Digitalization based on intelligent tools is, therefore, needed to conduct real-time analysis, considering the key parameters such as components' conditions, power demand patterns, and market prices to identify a smart combination and deliver high efficiency from existing installations [41].

The mGT industry currently faces new challenges of increasing operational flexibility, reducing operating costs, and improving reliability and availability while mitigating environmental impact. The main concern when it comes to distributed generation is the ability to maintain performance and high availability while minimizing the operation and maintenance costs.

One of the main challenges that is raised in the mGT is the overall efficiency of the cycle in the operation range, including design point and part-load conditions. Even though cogeneration applications of mGT lead to higher thermodynamic efficiencies, there are episodes of poor matching between heat and power demand, which indicates that further investigations are required to attain more efficient performance schemes. With an increasing number of passive houses, demand for heating will decrease which raises more challenges in the techno-economic aspects of mGT technology. However, the decrease of heat demand due to a paradigm shift in the structure of residential units and global warming effects will increase cooling demand, in which case the cooling application of mGTs will become more prevalent. For such applications, developing technologies for a more sophisticated operation of a micro gas turbine in cogeneration mode is essential.

Although performance improvements of gas turbine engines have been a subject of interest for decades, some features of micro gas turbines make them dissimilar to larger engines in several operating and system characteristics:

- The simple cycle form of micro gas turbines is less efficient than larger industrial gas turbines since the cycle pressure ratio in mGTs is considerably lower. The small size constraint in micro gas turbines imposes manufacturing complications to potential improvements of cycle parameters, such as pressure ratio and turbine inlet temperature. A recuperator helps with

compensating for these deficiencies in mGT cycles which makes them an essential element of micro gas turbines, unlike large-scale engines.

- Micro gas turbines operate at significantly higher shaft speeds. With a smaller size, typical problems such as tip supersonic speeds or mechanical limits are delayed to even higher rotational speeds. Therefore, micro gas turbines can operate at speeds above 100,000 rpm whereas a larger gas turbine will typically operate in the range of 3000 to 20,000 rpm [42]. Moreover, with compensating generators connected to mGTs, the rotational speed can vary according to power demand, unlike most large-scale turbines that remain at a constant speed. This alteration of rotational speed leads to different optimization practices for performance improvements.
- mGT cycles operate with lower pressure ratios (2~5) and turbine inlet temperatures (typically less than 1000 °C) which make the part-load operation span of these systems different from large-scale gas turbines (with pressure ratios up to 25 and turbine inlet temperatures up to 1700 °C). The span of cycle parameter variations, especially with altering rotational speed, is smaller compared to large-scale gas turbines.
- Considering the low-pressure ratio as well as the small volumetric flow and small power rating, a single-stage radial compressor and turbine are usually used. Both components have different operational behavior from axial versions, which is the common configuration that is implemented in large-scale engines.
- If the micro gas turbine operates as a CHP or CCHP unit, the system includes a second heat exchanger that uses the remaining exhaust thermal energy after the recuperator. The available exhaust gas, typically around 300˚C, provides energy for water and space heating, cooling systems such as absorption chillers, and process heat applications. The implementation of an economizer adds more application flexibility as well as constraints to the cycle.
- The fuel flexibility of mGTs, although having environmental and financial advantages, poses certain challenges to mGT design and operation. For conventional cycles, the low calorific value of the fuels requires the implementation of a larger volumetric flow of fuel to achieve the design turbine inlet temperature. This will affect the original matching point with the compressor. Considering the common turbine choking condition, the larger fuel flow rate results in lower demand for air from the compressor and, in general, an increase in compressor back-pressure and, therefore, lowering the surge margin [20]. On the other hand, a high air–fuel ratio within the primary combustion zone is required for achieving low emission levels at full-load conditions. Lean premix operation requires a large amount of air to be thoroughly mixed with fuel before combustion. This premixing of air and fuel enables clean combustion to occur at a relatively low temperature that is tolerated in uncooled turbines. Therefore, some operational limitations are imposed on the fuel–air flow ratio considering the type of fuel that is injected into the engine.

All the above-mentioned aspects of mGTs lead to a different practice to improve theirs in comparison with large-scale gas turbines. mGTs and the mGT cycles need further development towards [20]:

- higher electrical efficiency;
- increased flexibility for integration with other systems;
- increased flexibility towards the utilization of various sources of energy.

Improving the efficiency, flexibility, and reliability of micro gas turbines could be pursued by two approaches:

- component level
- system level

The main components of the engine, namely the compressor, recuperator, combustor, and turbine, show great potential for improvement in mGTs. The recuperator is responsible for a significant fraction of the electrical efficiency; therefore, its performance and limitations are additional parameters to be considered for improvements. On the other hand, the materials that are used in recuperators impose limitations on flow temperature at the turbine outlet (and the turbine inlet and hence the power output). Focusing on new designs and materials for recuperators could contribute to the efficiency of mGTs.

mGTs as a backup for the renewable-dominant power system of the future will operate in part-

load conditions as frequently as in full-load conditions. Therefore, it is essential to improve the efficiency of the compressor and turbine in off-design conditions along with the design point.

Combustion in mGTs occurs with lower equivalence ratios; the typical fuel–air ratio in mGTs is about an order of magnitude smaller than large-scale gas turbines. This means that the variation of flow properties in the flue gas in the case of replacing natural gas with hydrogen is small and, therefore, fewer complications are to be expected. The reason behind this is that flue gas properties of pure methane and pure hydrogen combustion diverge from each other as the equivalence ratio increases, yet in very lean combustions the difference is small. Focusing on hydrogen-driven mGTs will lead to building dispatchable units with zero carbon dioxide emissions. While fuel flexibility is an established advantage of mGTs, burning hydrogen and hydrogen-blended fuel is a goal to be accomplished by focusing on new technologies for combustion chambers.

Besides the component improvements, the system level improvements which are associated with the engine cycle and control of its operation could have a significant effect. Although mGTs are designed to run in cogeneration mode, the operation strategy is not mature and works the same as large-scale engines with addendums for cogeneration. The common design philosophy of operation control is based on sole electricity generation with an additional option of heat production. The controller runs the engine by focusing on power output and placing heat demand as the second priority. To improve the performance and operation efficiency of mGTs, it is essential to increase the flexibility of their operation by modifying the control and by setting the same priority for both heat and power generation.

As elaborated in the previous sections, the mGTs' main role in the future power generation industry is to provide support for intermittent renewable energy sources. Therefore, continuously monitoring mGTs' condition is important to maintain a reliable operation and avoid unpredicted shutdowns. Engine online monitoring is essential for tracking key parameters that are linked to the engine's health condition. Deterioration in engine performance has to be detected in the early stages, as well as signs of potential engine faults. Proper measures should be recommended based on the detections to prevent penalties on engine performance or even its life cycle in more severe cases.

A fault refers to a condition of an engine with a change of the form of its component(s) and hence its performance, from its original design or its initial operation. An engine fault can manifest itself by a change of the geometrical characteristics and/or integrity of the material of its parts, such as fouling, corrosion, erosion, etc., in a compressor or turbine. Monitoring the condition of the engine and its performance during operation and analyzing the observations and sensor measurements can help with detecting those possible faults. Engine faults can have other reasons such as bearings' wear, insufficient cooling of bearings, combustor malfunction, etc. Usually, non-performance-based monitoring methods such as vibration and oil samples can help with the detection of these faults.

To properly monitor the health condition of an mGT, an accurate model which represents healthy operation, and a condition monitoring platform that compares the engine and the model outputs are required. A precise computer model of the engine imitating the whole cycle performance in full-load and part-loads must be employed. The healthy engine model could be physics-based or data-driven, either way, the accuracy and speed of their prediction are the essential characteristics.

To develop a predictive model of the mGT cycle when a physics-based approach is chosen, a reduced order (0D and in some cases 1D) model is sufficient, as long as the maps and correlations that are implemented inside the components match the behavior of the actual healthy engine. To this end, a generic model of an mGT must be ready which could be tuned and become "adapted" to the actual engine during the first maneuvers of the operation. Once this model is tuned, then it works as a representative of a healthy engine and could be utilized as the core of condition monitoring platform. Figure 1.8 shows the adaptation process which is titled "learning period". The model should run by the same power setpoint as the actual engine and then the outputs of mGT and the model are compared and used for modifying the model's tuning parameters, which are basically the calibration factors of the maps and correlations. This process will continue until the difference between the engine outputs and model results are closer than acceptable tolerance. If the data-driven approach is chosen for building the model, the process will be replaced by simple data-based model training, by the means of machine learning methods.

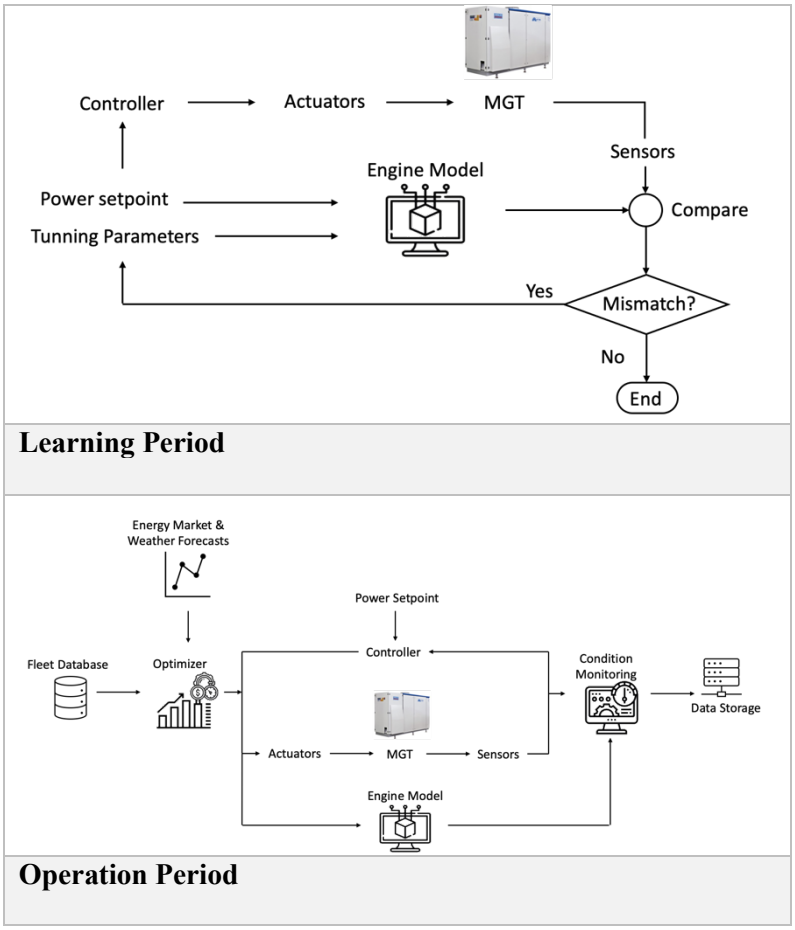

Figure 1.8 – Micro gas turbine fleet control based on online condition monitoring.

After the learning period is completed, the model must be utilized to provide inputs for the condition monitoring platform. In Figure 1.8, in the section "operation period", a structure for intelligent monitoring and control of mGT is proposed. The structure has three main poles: engine model, condition monitoring, and optimizer. The model is adapted to the healthy engine during the learning period, based on the initial operating hours of the mGT when it was assumed healthy. Then, a condition monitoring platform plays its role, which receives data from the engine as well as the model predictions.

The data-based condition monitoring can help with improving the reliability of the engine and reducing maintenance and operational expenditure by preventing harmful damages to the engine and avoiding unscheduled shutdowns. The advent of Industry 4.0 and the digitalization era provides the infrastructure for online collection and fast analysis of sensors' data to infer the condition of parts of the engine without dismantling the engine or getting direct access to its parts.

Artificial intelligence (AI) has demonstrated a powerful capacity in detecting and diagnosing faults of gas turbine engines. Monitoring through AI is proven to be an effective method for shifting from classical ''fail and fix'' practices to a ''predict and prevent'' methodology. Enhanced analytics and AI-enabled algorithms can help identify out-of-band behavior to improve efficiency and help with keeping the balance between energy supply and energy demand. AI techniques are quite useful when the problem is highly non-linear and a functional relationship between inputs and outputs is not easy to set up, or a quick response is required for real-time applications. Since physical problems of gas turbines have nonlinear and multidimensional characteristics, efforts to apply AI to performance prediction and fault detection and diagnosis of gas turbines have increased during the past decade.

The collected data in the condition monitoring platform of Figure 1.8 will be recorded and analyzed to estimate the health status of the mGT, which could improve the machinery maintenance strategy by employing statistical machine performance data and operational experience and hence prevent unexpected failure in the system. Online condition monitoring helps with predictive model improvements and, therefore, finding more optimized solutions for engine performance, which is the main role of the third pole of the system, the optimizer. Realizing the actual health condition of

components of the engine, an adaptive control scheme can be employed to compensate for the effect of deterioration. The component degradation level is assessed by the variations in the available measurements; then the information about engine health conditions is employed to adopt modified control strategies that guarantee a safe operation and limit the reduction in performance efficiency.

The function of the optimizer is tied to the controller of the micro gas turbine. The controller's function is to command the engine to operate with a specific fuel flow rate and specific rotational speed, that generates the demanded power while keeping the engines' components safe. The controller parameters, however, are constant and usually designed based on the engine operating at its absolute healthy status. If the condition monitoring platform could provide information that indicates the engine's deviation from its initial health, these control parameters could be modified by the optimizer and lead to higher efficiency and lifetime of the mGT. This flexibility of operation and increasing efficiency could be enhanced furthermore by adding flexibility to the cogeneration mode, as discussed previously. Inputs from weather and energy market forecast will be also beneficial to find the optimum operational strategy. The weather condition not only affects the fuel prices but also affects the amount and type of demand (i.e., electricity or heat).

It Is useful to put the data from one engine into a database of the fleet of micro gas turbines, where the diagnosis information of each engine could be available for others. The changes in controller parameters and their effect on performance will be useful and provide guidelines. Other than diagnostics of the micro gas turbine, sharing information among the engines could be beneficial for prognostic purposes. In Figure 1.8, the data from condition monitoring are collected and stored in the fleet database which is called by the optimizer. With a sophisticated infrastructure to organize the data, the prospect of employing more intelligent operation strategies will be increased.

1.4. Market Research

Due to the higher energy demand worldwide and the higher share of renewable energy, the market for micro-gas turbines in a decentralized energy context is getting higher inertia due to the intermittent generation characteristics of wind and solar energies. The integration of the mGT along with wind turbines, PV systems, biomass plants, fuel cells and energy storage would provide a secure, stable, efficient, economical, and environmentally friendly on-site energy production systems, connected close to the consumers load and providing the end consumer with heat and power without major transportation and conversation losses.

It is due to these characteristics of the foreseen energy market that the micro turbines market is expected to grow at a CAGR of 10.6% over the forecast period 2022 to 2030. The global micro turbines market size was reached at US$ 61.85 million in 2021 and is projected to rake US$ 139.6 million by 2030 [43]. North America dominated the global micro turbines market in 2021 and will led in the near future. The combined heat and power (CHP) segment dominated the micro turbines market in 2021. However, it is expected that the standby power segment will remarkably grow during the next decade.

In regard to energy end use, the industrial segment dominated in 2021. The main types of industries in which micro turbines proliferate are those heat driven applications where a robust source of energy is needed along with a high-grade source of heat. Thus, industries such as mining, oil & gas, wastewater treatment, and pharmaceutical are leading the use of micro turbines. In addition, small residential and office buildings are adopting this technology more and more as they may use a range of fuels and again, be used as a source of heat and power.

Despite the characteristics of the micro turbines that make them appropriate for some applications, they have found a difficult time to enter the market and increase the share of mGT in the power sector. The main competitor along the last years has been the internal combustion engine (ICE) which usually owns a higher electric efficiency and lower capital cost. Along with these features, the ICEs are granted with high market acceptance since it is widely adopted in the mobility industry with robust distribution channels. On the contrary, the mGT market penetration is low since it has failed to conquer a substantial part of the market, and only managed to be adopted in small market niches. Moreover, with the rapidly development of the hydrogen supply chain, the fuel cell market is expected to witness remarkable growth during the next decade as hydrogen is more widely available. This latter technology also owns a higher electric efficiency than the mGT but same or higher capital cost.

Table 1.2 – Specification of mGT manufacturers and their commercial products.

Manufacturer	Model	Rated Power kWe	Rated Electric Efficiency %
Capstone Green Energy [45]	C65	65	28
	C200S	200	33
	C600S (3 x C200S)	600	33
	C800S (4 x C200S)	800	33
	C1000S (5 x C200S)	1000	33
Flex Energy [46]	GT333S	333	33
	GT1300S (3 x GT333S)	1300	33
Aurelia [44]	A400	400	40.2
Ansaldo [47]	AE-T100NG	100	30
B+K [48]	ClinX 50	40	17.4 to 14.2
	ClinX 150	130	21.2 to 17.3
Euro-K [49]	MGT35	35	28
Bladon [50]	Bladon MGT	12	N/A
MTT [51]	EnerTwin	3.2	17
Mitis [52]	Micro10	12	23

However, due to the recent developments along with more companies entering the micro-gas turbine energy market, the electric efficiency gap is being reduced on the higher range power. Aurelia turbines owns a commercial mGT that offers 400 kWe with an electric efficiency of 40% [44].

However, the electric efficiency gap between mGTs and ICEs/FCs is much higher at micro-scale since the electric efficiencies of micro scale gas turbines (<10 kWe) merely reach 20%. However, the energy is not lost and is found in the exhaust gases being a great candidate for CHP applications. Furthermore, the many advantages offered by the mGTs remain certain. These main advantages can be summarized in the fuel flexibility capability of the mGT, being able to burn fuel with low and variable Low Heating Value (LHV). In addition, it is also a great candidate for remote sites as maintenance intervals are much greater than for the other two technologies.

Table 1.2 displays the different manufacturers of micro-gas turbines worldwide along with some characteristics of the commercial products they offer.

References – Chapter 1

[1] Caresana, F., Pelagalli, L., Comodi, G., and Renzi, M., "Microturbogas cogeneration systems for distributed generation: Effects of ambient temperature on global performance and components' behavior," Applied Energy, vol. 124, pp. 17–27, July 2014.

[2] De Paepe, W., Montero Carrero, Bram, M., S., Contino, F., and Parente, A., "Waste heat recovery optimization in micro gas turbine applications using advanced humidified gas turbine cycle concepts," Applied Energy, vol. 207, pp. 218–229, Dec. 2017.

[3] Comodi, G., Renzi, M., Caresana F., and Pelagalli, L., "Enhancing micro gas turbine performance in hot climates through inlet air cooling vapour compression technique," Applied Energy, vol. 147, pp. 40–48, June 2015.

[4] Duan, J., Sun L., Wang G., and Wu, F., "Nonlinear modeling of regenerative cycle micro gas turbine," Energy, vol. 91, pp. 168–175, Nov. 2015.

[5] Pilavachi, P., "Mini- and micro-gas turbines for combined heat and power," Applied Thermal Engineering, vol. 22, pp. 2003–2014, Dec. 2002.

[6] Kim, M. J., Kim, J. H., and Kim, T. S., "Program development and simulation of dynamic operation of micro gas turbines," Applied Thermal Engineering, vol. 108, pp. 122–130, Sept. 2016.

[7] Xiao, G., Yang, T., Liu H., Ni, D., Ferrari, M. L., Li, M., Luo, Z., Cen, K., and Ni, M., "Recuperators for micro gas turbines: A review," Applied Energy, vol. 197, pp. 83–99, July 2017.

[8] Jaatinen-Värri, A, Nerg, J, Uusitalo, A, Ghalamchi, B, Uzhegov, N, Smirnov, A, Sikanen, E, Grönman, A, Backman, J, & Malkamäki, M. "Design of a 400 kW Gas Turbine Prototype." Proceedings of the ASME Turbo Expo 2016: Turbomachinery Technical Conference and Exposition. Volume 8: Microturbines, Turbochargers and Small Turbomachines; Steam Turbines. Seoul, South Korea. June 13–17, 2016. V008T23A007. ASME. https://doi.org/10.1115/GT2016-56444

[9] Zornek, T., Monz, T., and Aigner M., "Performance analysis of the micro gas turbine Turbec T100 with a new FLOX-combustion system for low calorific fuels," Applied Energy, vol. 159, pp. 276–284, Dec. 2015.

[10] Cristina Cameretti, M. and Tuccillo, R., "Combustion features of a bio-fuelled micro-gas turbine," Applied Thermal Engineering, vol. 89, pp. 280–290, Oct. 2015.

[11] Kim, M. J., Kim, J. H., and Kim, T. S., "Program development and simulation of dynamic operation of micro gas turbines," Applied Thermal Engineering, vol. 108, pp. 122–130, Sept. 2016.

[12] Henke, M., Klempp, N., Hohloch M., Monz T., and Aigner M., "Validation of a T100 Micro Gas Turbine Steady-State Simulation Tool," in Volume 3: Coal, Biomass and Alternative Fuels; Cycle Innovations; Electric Power; Industrial and Cogeneration, (Montreal, Quebec, Canada), p. V003T06A003, American Society of Mechanical Engineers, June 2015.

[13] Montero Carrero, M., Decoupling heat and electricity production from micro gas turbines: numerical, experimental and economic analysis of the micro humid air turbine cycle. PhD thesis, Vrije Universiteit Brussel, Université Libre de Bruxelles, March 2018.

[14] Turbec Spa, "T100 microturbine system, Technical description (T100 Natural Gas) [D14127-03 Technical description Ver 3]," tech. rep., December 2009.

[15] De Paepe, W., Renzi, M., Montero Carrerro, M., Caligiuri, C., and Contino, F., "Micro Gas Turbine Cycle Humidification for Increased Flexibility: Numerical and Experimental Validation of Different Steam Injection Models," American Society of Mechanical Engineers Digital Collection, Aug. 2018.

[16] Zornek, T., Monz, T., and Aigner, M., "Performance analysis of the micro gas turbine Turbec T100 with a new FLOX-combustion system for low calorific fuels," Applied Energy, vol. 159, pp. 276–284, Dec. 2015.

[17] Traverso, A., Massardo, A. F., and Scarpellini, R., "Externally Fired micro-Gas Turbine:

Modelling and experimental performance," Applied Thermal Engineering, vol. 26, pp. 1935–1941, Nov. 2006.

[18] Traverso, A., Calzolari, F., and Massardo, A., "Transient Analysis of and Control System for Advanced Cycles Based on Micro Gas Turbine Technology," Journal of Engineering for Gas Turbines and Power, vol. 127, pp. 340–347, Apr. 2005.

[19] Calabria, R., Chiariello, F., Massoli, P. , and Reale, F., "CFD Analysis of Turbec T100 Combustor at Part Load by Varying Fuels," in Volume 8: Microturbines, Turbochargers and Small Turbomachines; Steam Turbines, (Montreal, Quebec, Canada), p. V008T23A020, American Society of Mechanical Engineers, June 2015.

[20] Jaatinen-Värri, A, Nerg, J, Uusitalo, A, Ghalamchi, B, Uzhegov, N, Smirnov, A, Sikanen, E, Grönman, A, Backman, J, & Malkamäki, M. "Design of a 400 kW Gas Turbine Prototype." Proceedings of the ASME Turbo Expo 2016: Turbomachinery Technical Conference and Exposition. Volume 8: Microturbines, Turbochargers and Small Turbomachines; Steam Turbines. Seoul, South Korea. June 13–17, 2016. V008T23A007. ASME. https://doi.org/10.1115/GT2016-56444

[21] Head, A. J., and Visser, W. P. J., 2012, "Scaling 3-36 kW Microturbines, "Proceedings of ASME Turbo Expo 2012, Copenhagen, Denmark, June 11-15, ASME Paper No. GT2012-68685.

[22] Henke, M., Monz, T., and Aigner, M. (August 19, 2013). "Inverted Brayton Cycle with Exhaust Gas Recirculation—A Numerical Investigation." ASME. J. Eng. Gas Turbines Power. September 2013; 135(9): 091203. https://doi.org/10.1115/1.4024954

[23] Agelidou, E., Monz, T., Huber, A., and Aigner, M., "Experimental investigation of an inverted brayton cycle micro gas turbine for chp application," 06 2017.

[24] De Paepe, W., Montero Carrero, M., Bram, S., Parente, A., and Contino, F., "Experimental Characterization of a T100 Micro Gas Turbine Converted to Full Humid Air Operation," Energy Procedia, vol. 61, pp. 2083–2088, 2014.

[25] I. Renewable Energy Agency, "IRENA, Global Renewables Outlook: Energy Transformation 2050," 2020. Accessed: Jan. 25, 2021. [Online]. Available: www.irena.org

[26] O. US EPA, "Catalog of CHP Technologies." Accessed: Jan. 24, 2021. [Online]. Available: https://www.epa.gov/chp/catalog-chp-technologies

[27] The European Commission's Knowledge Centre for Bioeconomy, "Brief on biomass for energy in the European Union," 2018.

[28] G. Brauner *et al.*, "Electrical Power Vision 2040," 2013.

[29] International Energy Agency, "Energy Technology Perspectives 2014 Harnessing Electricity's Potential." Accessed: Jan. 26, 2021. [Online]. Available: http://www.iea.org/termsandconditionsuseandcopyright/

[30] R. H. Lasseter, "MicroGrids," in *2002 IEEE Power Engineering Society Winter Meeting. Conference Proceedings (Cat. No.02CH37309)*, vol. 1, pp. 305–308. doi: 10.1109/PESW.2002.985003.

[31] I. Aslanidou, M. Rahman, V. Zaccaria, and K. G. Kyprianidis, "Micro Gas Turbines in the Future Smart Energy System: Fleet Monitoring, Diagnostics, and System Level Requirements," *Front Mech Eng*, vol. 7, p. 51, Jun. 2021, doi: 10.3389/FMECH.2021.676853/BIBTEX.

[32] A. Ali, W. Li, R. Hussain, X. He, B. Williams, and A. Memon, "Overview of Current Microgrid Policies, Incentives and Barriers in the European Union, United States and China," *Sustainability*, vol. 9, no. 7, p. 1146, Jun. 2017, doi: 10.3390/su9071146.

[33] M. Soshinskaya, W. H. J. Crijns-Graus, J. M. Guerrero, and J. C. Vasquez, "Microgrids: Experiences, barriers and success factors," *Renewable and Sustainable Energy Reviews*, vol. 40, pp. 659–672, Dec. 2014, doi: 10.1016/j.rser.2014.07.198.

[34] D. Bohn, "Micro gas turbine and fuel cell: a hybrid energy conversion system with high potential." NATO Research & Technology Organisation, 2005. doi: alm70022774x.

[35] S. Gros, D. Jakus, J. Vasilj, and M. Zanon, “Day-ahead scheduling and real-time economic MPC of CHP unit in microgrid with smart buildings,” *IEEE Trans Smart Grid*, vol. 10, no. 2, pp. 1992–2001, Mar. 2019, doi: 10.1109/TSG.2017.2785500.

[36] S. N. Bhaskara and B. H. Chowdhury, “Microgrids - A review of modeling, control, protection, simulation and future potential,” in *IEEE Power and Energy Society General Meeting*, 2012. doi: 10.1109/PESGM.2012.6345694.

[37] “Energy statistics - an overview ,” 2018. Accessed: Jan. 25, 2021. [Online]. Available: https://ec.europa.eu/eurostat/statistics-explained/index.php?title=Energy_statistics_-_an_overview

[38] G. Brauner *et al.*, “Electrical Power Vision 2040 for Europe,” EUREL, 2012.

[39] M. A. Cañete, “Commission Recommendation (EU) 2016/1318,” 2016. Accessed: Feb. 12, 2021. [Online]. Available: http://www.sciencedirect.com/science/article/pii/S0306261911007811/

[40] European Commission, “Energy performance of buildings directive.” https://ec.europa.eu/energy/topics/energy-efficiency/energy-efficient-buildings/energy-performance-buildings-directive_en (accessed Feb. 12, 2021).

[41] “Next Generation of Micro Gas Turbines for High Efficiency, Low Emissions and Fuel Flexibility.” 2020.

[42] European Turbine Network (ETN), “Micro Gas Turbine Technology Research and Development for European Collaboration,” ETN Micro Gas Turbine Technology Summary.

[43] “Micro Turbines Market - Global Industry Analysis, Size, Share, Growth, Trends, Regional Outlook, and Forecast 2022-2030,” Precedence Research, 2021.

[44] “Aurelia A400,” Aurelia Turbines, [Online]. Available: https://aureliaturbines.com/files/sites/775/190115-datasheet-a400-iso-eu-6015b194-826a-48cd-bceb-08368c5fc968.pdf. [Accessed 09 11 2022].

[45] “C1000S, C800S, C600S, C200S and C65,” Capstone Green Energy, [Online]. Available: https://www.capstonegreenenergy.com/products/energy-generation-technologies/capstone-microturbines/c1000s. [Accessed 09 11 2022].

[46] “Gas Turbines Solutions,” FlexEnergy, [Online]. Available: https://www.flexenergy.com/power-solutions/turbine-innovations/. [Accessed 09 11 2022].

[47] “AE-T100 - The modular value,” Ansaldo Energia, [Online]. Available: https://www.ansaldoenergia.com/offering/equipment/turbomachinery/microturbines/ae-t-100. [Accessed 09 11 2022].

[48] “BK ClinX Products,” B+K Energy Systems, [Online]. Available: https://bergundkiessling.com/wp-content/uploads/2021/09/BK-ClinX-Produktbroschuere_V2.3-l-eng-web.pdf. [Accessed 09 11 2022].

[49] “Developments of the Euro-K,” Euro-K, [Online]. Available: https://euro-k.de/en/developments/. [Accessed 09 11 2022].

[50] “Micro Turbine Genset,” Bladon, [Online]. Available: https://www.bladonmt.com/bladon-micro-turbine-genset. [Accessed 09 11 2022].

[51] “EnerTwin,” MTT, [Online]. Available: https://enertwin.com/enertwin/. [Accessed 09 11 2022].

[52] “Our microturbine,” mitis, [Online]. Available: https://www.mitis.be/microturbine. [Accessed 10 11 2022].

2. Component oriented optimisation

2.1. ESR4

With the rapid advancement of technology, compact, efficient, light, low-noise, low-cost devices are becoming increasingly popular, especially in the transportation and power generation industries. A Micro Gas Turbine (mGT) is an alternative power source for the decentralized market at the micro-scale that is lightweight and may provide a viable alternative to internal combustion engines. The lower efficiency and cost-effectiveness of the device prevent it from capturing a significant proportion of the global market. Generally, these types of bladed turbomachinery are composed of a bladed compressor, turbine, and combustion chamber etc., as major components. At the microscale, conventional bladed devices have many disadvantages, such as tight clearances, high viscous frictional losses in the rotor, the viscous effect, and the cost of manufacturing micro bladed impellers [1-3]. By deflecting and constraining the flow within the rotor, Rice [4] hypothesized that momentum exchange is affected by blades or channels shaped to deflect and constrict the fluid flow. The efficiency of conventional turbomachinery decreases with size scale down, in contrast to bladeless turbomachinery, which has almost constant efficiency over decreasing the sizes [1,4]. The bladeless turbomachinery invented by Nikola Tesla in 1913 is based on the boundary-layer phenomenon. As a result of the name of the inventor, such a type of turbomachinery has become widely known as a Tesla turbomachinery. A rotor with a bladeless or Tesla design consists of multiple thin, flat disks mounted on a shaft with the specified gap. The rotor is mounted within the stator or volute casing, which forms the Tesla turbomachinery. There are several advantages of bladeless turbomachinery including ease of manufacturing, low production costs, low noise levels, and reversibility of operation in order to meet the needs of the current market that make it more attractive than conventional technologies. In spite of this, the experimental performance indicates a low level of efficiency. Despite the fact that the majority of research is focused on Tesla turbines, there are countable data available on the experimental and numerical performance of Tesla compressors. It is important to note that both modes of operation are based on the same principle. It is therefore the bladeless compressor that is the subject of this research.

2.1.1 Introduction

For microscale applications, such as power generation, medical, chemical processes, etc., there is an increasing demand for efficient, lightweight, low-cost, low-noise compressors. Contrary to conventional compressors, bladeless compressors are fulfilling the current market demand and exhibit almost constant performance as the scaling down size, which attracts researchers to further investigate the subject [1,2,4,5]. In the bladeless compressor rotor, mechanical power is provided to the fluid, which enters axially through the center of the disk, passes through its narrow channels in an outward spiral motion, and exits tangentially as shown in Fig. 2.1. A rotating disk imparts a shear force on the fluid that increases its dynamic pressure at the outlet of the disk. The Tesla and bladeless compressors work on boundary layer and viscous forces, so they are also called boundary layer or viscous pump/compressors. Their disks distinguish bladeless compressor assemblies from conventional bladed compressor assemblies. In this assembly, the pressure does not affect the rotation of the compressor, which is characterized by pulse-free laminar flow patterns.

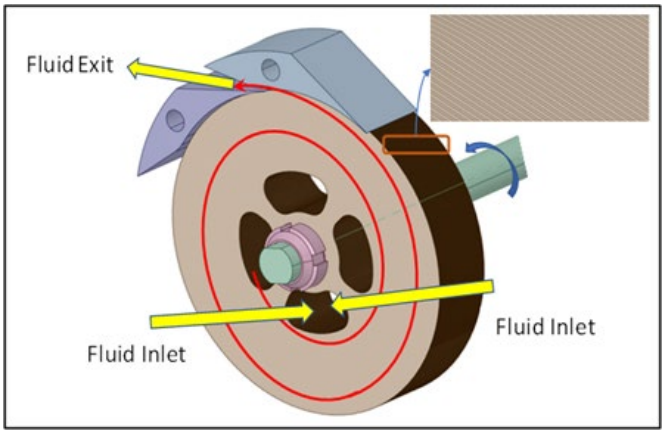

Fig. 2.1 Tesla compressor: principle of operation

Using numerical and experimental analysis, the present study examines the performance, major issues, and losses of a bladeless compressor. In accordance with the numerical and experimental analysis, further improvements are made to the geometry in order to maximize performance and minimize losses.

2.1.2. Performance Investigation of bladeless compressor

The bladeless expander prototype model was developed in TPG laboratory (University of Genoa). It has achieved maximum efficiency of 36.5% at 10 krpm with 2 nozzle configurations (experimental tests in [6]). The same prototype model (without any modification) is studied in reversible or compressor mode to characterize its performance by Tiwari [1]. Tiwari first numerically studied the bladeless compressor and its results performing a comparison with the experimental results. The numerical analysis was carried out based on steady-state simulations, the bladeless compressor performance is determined for three different rotational speeds: 10 krpm, 20 krpm, and 30 krpm. At 30 krpm, he obtained a maximum pressure ratio of 1.21 and a maximum efficiency of 43%, while at low mass flow rates, the rotor only efficiency is 78%. The Comparison of numerical and experimental results can be performed closing a valve at the compressor outlet. When the valve is closed, all flow is directed through the end disks, thereby causing a leakage in the compressor. Static pressure is created in the discharge chamber prior to the valve. In closed valve conditions, there is a small difference between experimental and numerical static pressure ratios, i.e., 0.95%, 0.35%, and 0.43%, respectively, at 30 krpm, 20 krpm, and 10 krpm, which indicates very good agreement between the two analyses. Based on the experimental and numerical results he noticed several issues that impact overall Tesla compressor performance. In general, bladeless compressor performance is influenced by the disk gap, radius ratio, interaction between rotors and stators, stator shape, number of stators, inlet and exhaust sections, and sealing system, but there is no optimal design parameter that can be used to evaluate the best performance point of such devices. In the following points the main aspects of the prototype are summarized.

- According to the prototype model, the disk gap was 0.1 mm and the Reynolds number was 2.3. Rice [4] recommends that the disk gap should be equal to twice the thickness of the boundary layer, where Reynolds number is 5 or 6.
- Initially, the stator was intended for use as a nozzle in the expander, which has a large expansion ratio of 10.2 in reversible operation. There was a recirculation of fluid inside the diffuser that resulted in a degradation of performance.
- There is a large gap between the end wall and end-disk, causing significant leakage and adversely affecting the performance of the system. It is certain that providing a sealing mechanism (which was absent in the prototype model) would improve the net mass flow, pressure ratio, and the device efficiency.

Tiwari [2] is continuing his research to further improve the performance of the bladeless compressor. As the Tesla Rotor is the heart of the Tesla compressor, the focus of his research regards improving rotor performance and then on improving stator performance.

1. Rotor:

- A numerical analysis of the independent rotor has been conducted by optimizing the gap between the disks using dimensionless Ekman and Reynolds numbers.
- Both the Ekman and Reynolds numbers have been finalized for the purposes of improving efficiency.
- The radius ratio of the disks is optimized with an optimal disk gap.

2. Stator:

- Based on the model study of the prototype, the stator shapes (diffusers) are numerically analyzed according to quasi-static nozzle/diffuser theory to eliminate recirculation and pressure loss issues.
- In order to improve efficiency and pressure performance, a statorless design case will be examined (volute casing).

2.1.3. Numerical analysis of bladeless compressor

It has been demonstrated that pressure-based solvers can handle highly compressible flows in turbomachinery applications with greater computational stability than density-based solvers. Consequently, a pressure-based steady solver is selected for solving steady and compressible flow, using ideal gas as the working fluid in the current study. The three-dimensional Navier–Stokes equations are solved utilizing ANSYS FLUENT and discretized using the "finite volume method." The viscous model utilized is k-w SST, a Reynolds-averaged Navier–Stokes model which has become the industry standard for turbulence modelling [1,7]. The k-w SST combines the advantages of the k-w model (better prediction near-wall region) with those of the k-e model (better prediction of the far-field region) [8]. A second-order upwind linear interpolation is used to discretize the governing equations and a COUPLED scheme for fluid coupling of pressure and velocity is used for solving them. This study considers the flow domain between two rotating disks as stationary. For the entire "rotor-diffuser" and "rotor-volute" configuration, half of the disk thickness and half of the gap between rotating disks are considered as a single fluid domain. As a result of this computational approach, the problem is simplified and execution time is reduced.

2.1.3.1. Performance analysis of bladeless rotor

A numerical studied is carried out on the different disk gap based on the Ekman number as discussed by Tiwari 2 at 40000 rpm. A graph of total to total and static to static pressure ratios for four different Ekman numbers is shown in Figure 2.2 (a). There is a higher characteristic line for the Ekman number equal to 1.6 in all mass flow rates, compared to the other cases. Additionally, the total-to-total adiabatic efficiency is best at Ekman number 1.6 as shown in Fig. 2.2(b). In the tested cases, the Reynolds number is approximately 10, almost twice as high as the optimal values of 5 and 6 [4]. A discussed by Tiwari [2] rotor model (prototype) with an Ekman number of 0.8 shows the lowest efficiency of approximately 78%. As the Ekman number is increased from 0.8 to 2, the rotor efficiency increases until 1.6 Ekman number then it's decreases. It's showing Ekman number 0.8 to 1.6 worst to best and 1.6 to 2 best to worst. Consequently, the performance map indicates that Ekman numbers around 1.6 represent the optimal case, particularly for low mass flow rates with "rotor only" total to total efficiency of more than 82.6%. Approximately a 5% efficiency increase is shown between model (Ek-0.8) and rotor model (Ek-1.6). The static-static pressure vs mass flow is shown in Fig.2.2 (a) where Ekman 1.6 indicates a higher static pressure ratio of 1.29 compared to other Ekman numbers at 0.045 g/s, which is bit improved in total to statice efficiency. The analysis is carried out for the single gap and the higher efficiency is obtained at 0.045 g/s.

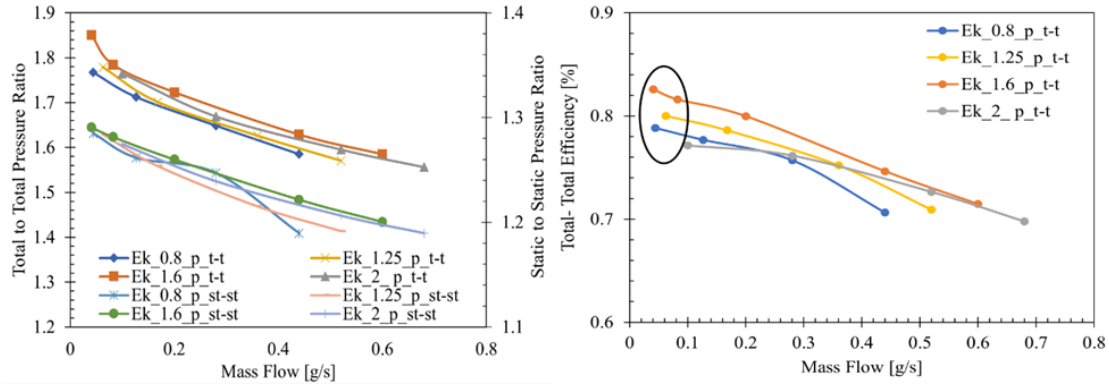

(a) **(b)**

Fig. 2.2 Rotor only (a): Total - total and static-static pressure ratio vs mass flow rate for different Ekman numbers. (b): Total to total adiabatic efficiency vs mass flow rate for different Ekman numbers.

The rotor-only Tesla compressor behaves differently from a conventional one when the disk gap is increased. Our pressure ratio line appears to be asymptotic to the y-axis, whereas that of the bladed compressor appears to be asymptotic to the x-axis. There is a great deal of interest in this result, which actually demonstrates the advantages associated with bladeless turbomachinery. With no blades, the flow can adjust to the optimal flow angle at different mass flow rates, giving maximum performance every time. This obviously cannot happen in a constant blade compressor where losses decrease the performance as we diverge from the operating point.

The disk gap has been optimized using what published by Tiwari [2] which shows a greater rotor efficiency at Ekman of 1.6 and Reynolds number equal to 10. To further improve the performance, the optimized disk gap is evaluated at different rotor diameter ratios (DR), which are numerically tested at 40000 rpm. In this study, two types of rotor diameter ratio are considered, namely DR-2, and DR-2.5. In the diameter ratio DR-2, 120 mm and 60 mm are considered as the outer and inner diameter, respectively. A diameter ratio of DR-2.5 is maintained by two methods: the first is by fixing the inner diameter at 60 mm and changing the outer diameter from 120 mm to 150 mm, followed by fixing the outer diameter at 120 mm and minimizing the inner diameter (from 60 mm to 48 mm). It is expected that the pressure ratio will increase with increasing diameter, which is highly dependent on the area. According to Figure 2.3(a), pressure ratios increase with higher diameter at low mass flow rates, while pressure ratios are lower in the other two cases with smaller diameters (fixed outer diameters). There is a slight increase in the pressure ratio for diameter 2.5 (120 mm / 48 mm) at each mass flow rate, compared to diameter ratio equal to 2. This is most likely the result of the larger surface area. This Figure 3.1.3(b) shows that maximum efficiencies tend to cluster at mass flow rates between 0.5 g/s and 0.1 g/s for various diameter ratios. According to the diameter ratio 2.5, the rotor efficiency is greater

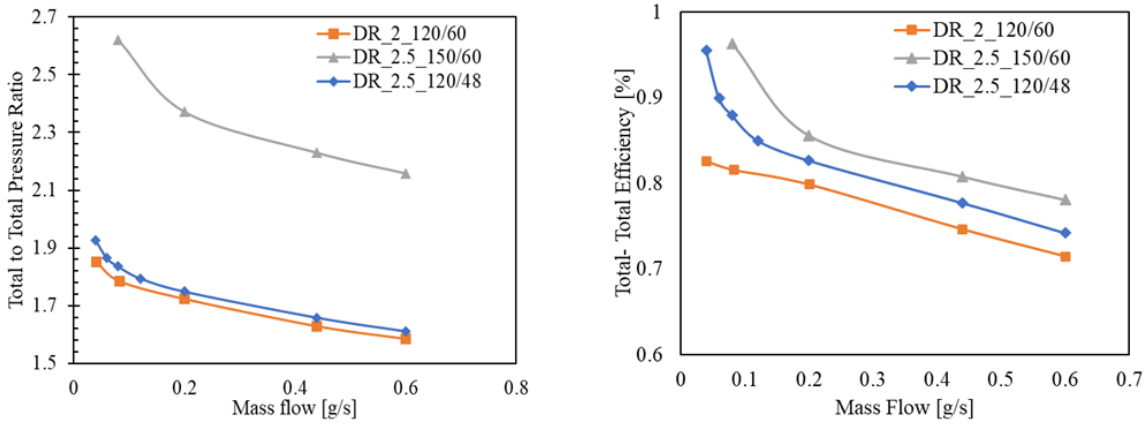

(a) **(b)**

Fig. 2.3 Rotor only (a): Total to total pressure ratio vs mass flow rate at different diameter ratio. (b): Total to total adiabatic efficiency vs mass flow rate at different diameter ratio.

than 95% in both cases at slightly different mass flow rates. It is possible to achieve a higher efficiency at different mass flows as a result of the larger inlet area. However, such geometrics can be chosen based on the application and requirement.

2.1.3.2. Performance analysis of bladeless compressor

An improved bladeless compressor rotor and stator geometry has been developed based on the existing prototype model. An optimized and efficient rotor has been initially simulated with a diffuser case (diff.1) that has been proposed by Tiwari [2]. During the numerical analysis, only one gap has been considered. Numerical analysis has been carried out using the commercial software ANSYS fluent. The k-omega SST model has been selected with the 2nd order upwind and coupled option (pressure and velocity). The model is based on atmospheric pressure at 300 K for the inlet condition as well as mass flow at the out-boundary condition [1][2]. According to Figure 2.4(a), diff.1 has been simulated with all diameter ratios (DR) discussed in the previous section. As compared to rotors with diameter ratios (DR) of DR-2 and DR-2.5, the efficient rotor with diameter ratio DR-2.5 has shown a higher-pressure ratio. An increase in pressure has been calculated with increasing tip speed, which is high at DR 2.5. At the same tip speed, the results have shown that it is possible to define two rotors with DR 2 and DR 2.5 with higher and lower inner diameters, respectively. The DR 2.5 pressure (120 mm / 48 mm) is a bit high in these cases due to the higher surface area. The statorless (VTM1) case has been numerically analysed for the first time, which shows a higher-pressure ratio of 1.47 with a higher mass flow rate. Figure 3.1.4(b) shows bladeless compressors with diffusers and statorless configurations: total-to-static efficiency in relation to mass flow rate. Tiwari's proposed diffuser has been numerically tested with different rotor configurations. There is a significant increase in rotor efficiency at diameter ratio 2.5, which is also evident when considering diffuser cases. DR-2.5 has a total static efficiency of 1.5%, which is considered higher than the DR-2 one. When this efficient rotor is tested with statorless configuration (i.e. volute casing), further efficiency is increased by 1.5%. The total static efficiency is lower for the diffuser case (diff.1) than for the statorless configuration. It is shown that the statorless configuration has an efficiency of around 55%, whereas the diffuser configuration (diff.1) has a lower efficiency.

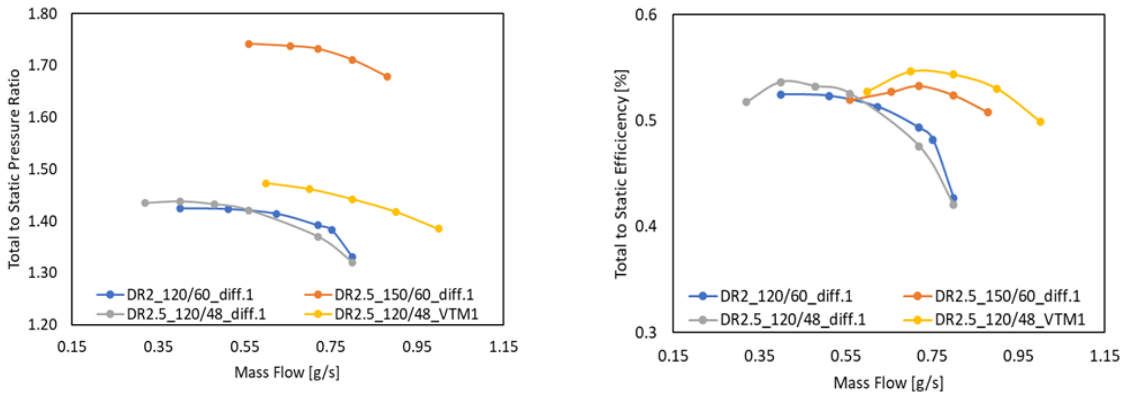

(a) **(b)**

Fig. 2.4: Bladeless compressor with stator and statorless (a): Total to static pressure ratio vs mass flow rate at different diameter ratios. (b): Total to static efficiency vs mass flow rate at different diameter ratios.

2.1.4. Noise characterization of bladeless blower

In modern turbomachinery compactness, efficiency and cost-effectiveness are highly addressed with the related noise emissions having been always a significant concern. In conventional machinery, it has been challenging to deal with noise, but in bladeless turbomachinery, such noise emissions is potentially lower [4]. The authors [1][4][5][6] have worked on such types of bladeless devices and observed low noise emission, but there was no clear evidence available on it. In turbomachinery, there are two main sources of acoustic noise: the first is due to mechanical rotation while the second to aeroacoustics [9][10]. Due to rotor unbalance and solid parts contacts (such as bearing and motor), shaft mechanical noise is emitted while aeroacoustics noise is created by the fluid flow oscillations and interaction with solid parts [10]. In bladed machinery, if rotational speed and machine size increase, then the contribution ascribable to aeroacoustics grows, along with fluid-structure interactions. Cumpsty [11] noticed in his study, based on the challenges which arise when facing turbomachinery aeroacoustics in turbo engines, that most of the noise is generated by the interaction of the fan wake with the downstream outlet guide vane (OGV). The objective of this research is to develop an innovative noise characterization method for an air Tesla-type bladeless blower that works on the same principles as a Tesla pump/compressor. According to the literature review, there has not been any study on the noise characterization of bladeless turbomachinery. Therefore, in this study an experimental investigation of the acoustic behavior of such devices has been performed comparing the results to conventional machines.

2.1.4.1. Noise measurement and discussion

The measurements are obtained using a number of the most recent techniques and the accuracy of the measurements is evaluated using the most recent post-processing methodologies. Noise characterization is conducted using the commercial software LMS Test Lab. In order to determine the accuracy of noise characterization, the acoustic power is calculated based on sound intensity measurement that is employed at a distance of 500 mm from the source. For the purpose of measuring intensity, there are ten positions that are selected in accordance with ISO standards. Also, microphones are placed at different distances from the source, namely 250 mm, 350 mm, and 500 mm, at the front, top, and back of the source, respectively, to measure the level of sound pressure. It is discussed in detail how the acoustic performance of the air Tesla blower at different distances is compared with that of a conventional blower.

Figure 2.5 shows the average RMS spectrum of the measured sound intensities at different angular speeds, such as 10 krpm, 20 krpm, and 30 krpm. For each speed, the sound intensities are measured at ten positions surrounding the source. The cursor has been inserted in this representation at significant frequencies including revolution frequency (1 X) and orders of 4 X, 8 X, and 12 X. There is a significant amount of energy present in their respective spectral contents at such frequencies. In order to calculate an average amplitude level, the RMS value is calculated for each of the ten positions. Fig. 2.5 illustrates the same sound intensity level (SIL-dB) averaged spectrum in dB scale: the upper average intensity levels (dB) are 90 dB, 80 dB, and 62 dB for angular speeds of 30 km/h, 20 km/h, and 10 km/h, respectively. As shown in Figure 2.5, the sound intensity level (SIL-dB) increases with increasing angular speed, and this may be due to acoustic radiation generated by both mechanical and aeroacoustics effects.

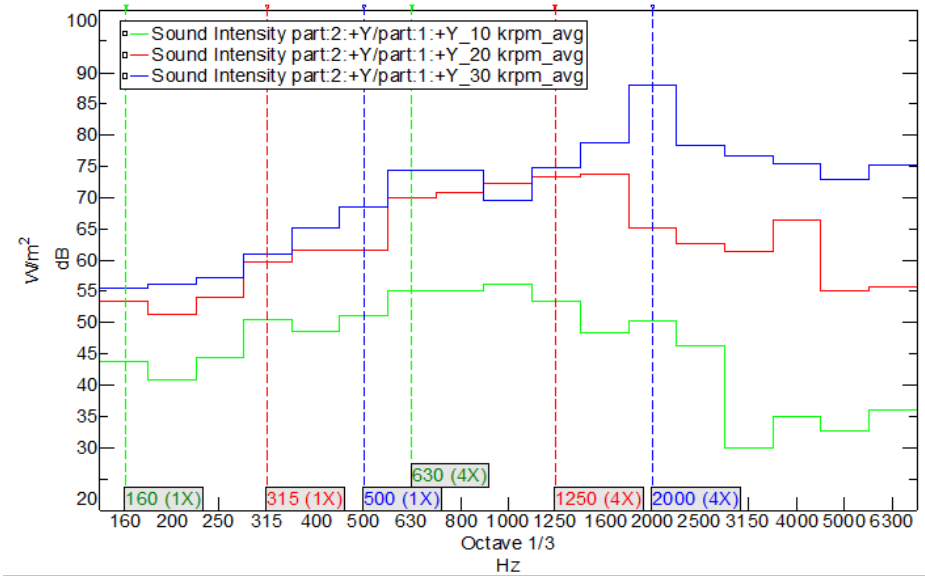

Fig. 2.5 – Average sound intensity at different rotational speed with averaged spectrum (SIL-dB)

2.1.4.2. Comparison of air Tesla and conventional blower

A comparison is made between the acoustic emissions of an air Tesla and those of a conventional blower. Lucifredi [12] investigated the acoustic emission of a bladed conventional blower at various distances and at 12700 rpm. In order to determine the acoustic power and pressure levels accurately, the acoustic intensity is measured at different distances using an acoustic intensity sensor. A bladed blower is smaller than an air Tesla blower, and a bladed rotor is three times smaller than an air Tesla blower. Bladed blowers have volute-type duct outlets, while Tesla blowers have cylindrical chambers between the rotor and casing. There are eight cylindrical outlets connected to this chamber through a cylindrical outlet hole. Comparisons of noise are conducted at the same tip speed of 27 m/s for both devices. It is considered to be a fair comparison since (i) the speed of the tip of a rotor is proportional to the maximum head that a machine can achieve, both bladeless and bladed, and (ii) the frequency of tip passing creates a considerable amount of noise in bladed machines. Alternatively, the two blowers will be compared for equivalent operating conditions. Acoustic intensity sensors were installed at fixed distances of 0.5 m, 1 m, 1.5 m, and 2 m in order to compare the performance of the bladed blower with the performance of the air Tesla. As expected, the bladed blower spins at 12700 rpm, whereas the air Tesla blower spins at 4300 rpm at the same tip speed of 27 revolutions per minute. The discussion of theoretical methods for quadrupoles and dipoles has generally been limited to models for describing the sound generated by pressure fluctuations at the blade surfaces.

According to Lucifredi [12], the sound pressure levels (SPL-dB) of bladed blowers were measured at distances of 1 m, 2 m, 3 m, and 4 m, yielding 83.77, 79.57, 77.93, and 74.91 respectively. Similarly, acoustic intensity is measured at distances of 0.5 m, 1 m, 1.5 m, and 2 m to determine acoustic power and pressure levels. Fig. 2.6 illustrates a comparison of sound pressure levels produced by a Tesla blower and a bladed blower at different distances. Compared to the air Tesla blower, the conventional blower is extremely noisy. When the bladed curve is extrapolated towards the y-axis, it shows a higher sound pressure of 86 dB at 0.5 m as opposed to 57 dB for the air Tesla. In the same manner, the air Tesla rotates at a higher speed of 30000 rpm, and the noise at 0.5 m decreases significantly as distance increases. Noise emission increases quadratically when distance decreases. Since the conventional blower has multiple zones of solid interaction, particularly the number of blades, it is noisier than the Tesla (bladeless) blower. In accordance with sound intensity theory, the acoustic emission curve of a bladeless blower decreases quadratically as distance increases. It has been demonstrated that the acoustic emission of the Tesla blower is inversely proportional to the square of the distance, which is an analytical trend that is not perfectly obtained with a bladed blower. This result has been explained by the measurement section as being obtained in a similar nearly anechoic environment to that in which the air Tesla blower test is conducted.

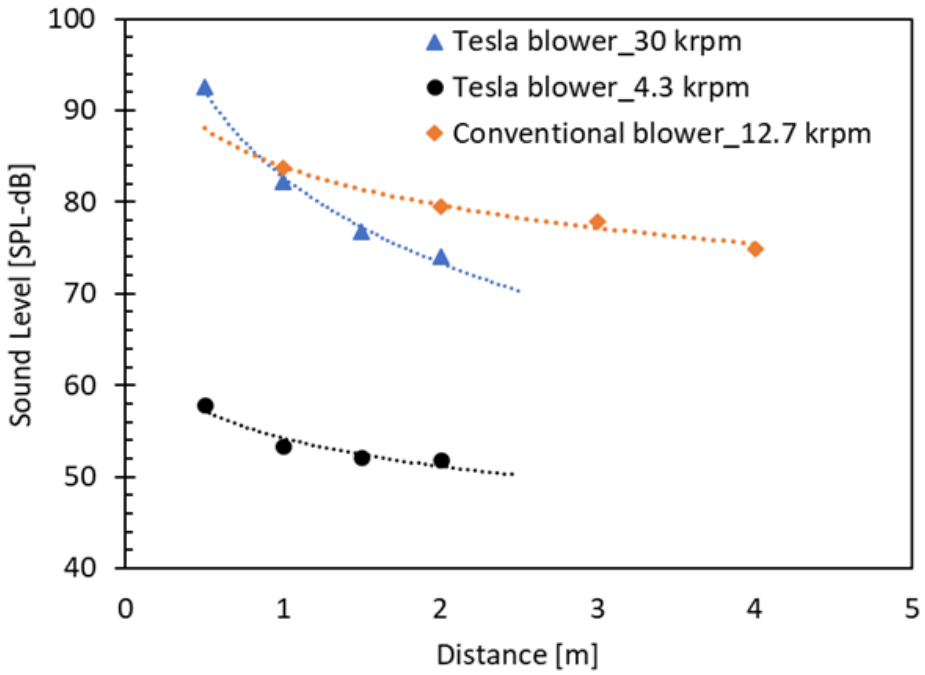

Fig. 2.6 – Acoustic level (SPL-dB) comparison of an air Tesla and bladed blower and different distances.

2.2. ESR5

2.2.1. Introduction

Counter-rotating propellers appeared at the beginning of the 20th century and were used in several well-known aircrafts such as the Spitfire (UK) and the Antonov An-22 (USSR). The main advantage of the contra-rotating turbomachinery is the increased power density of the system, which means the engine size is reduced and the overall weight is decreased. Furthermore, these systems improve the through-flow behaviour, increasing the aerodynamic efficiency and, in the case of the propellers, providing more thrust. Recently, there is an increasing interest in mGTs for mobile applications such as UAV propulsion, car range extenders and even exoskeleton power supplies, which require high energy density sources. However, the current mGT technology suffers from low overall performance. This is due to the significant heat transfer between cold and hot components, the manufacturing restrictions of such small devices and the high aerodynamic losses of these scaled-down components.

Mixed flow and radial compressors are widely used in mGT applications. Although they provide a higher-pressure ratio per single stage than an axial compressor, high swirl at the exit of the impeller results in higher losses and lower adiabatic efficiencies. A potential solution to improve the flow behaviour in a radial compressor is the contra-rotating impeller configuration. This consists of two rotors, turning in opposite directions. There are several investigations, both experimental and numerical, that are limited to axial compressors and demonstrate the advantages of contra-rotating turbomachinery [13].

Wilcox [14] was the first trying to evaluate the potential of a counter-rotating axial flow compressor. Utilizing a one-dimensional analysis, he calculated a higher-pressure ratio, lower relative Mach number and flow turning angle for the counter-rotating compressor. Pundhir and Sharma [15] conducted an experiment of a contra-rotating axial compressor stage, investigating the effect of speed ratio and axial spacing between the contra-rotors. They found that the stall behaviour was better when the second rotor was running at a higher speed.

Furukawa et al. [16] analysed the characteristics of a contra-rotating pump (CRP) using experimental data. The results shown that the CRP, running at a lower rotational speed, had a more stable head characteristic curve and an extended operational range, especially when the rotational speeds of the front and rear rotor were individually controlled. At the same time, both the efficiency and the compactness of the CRP were improved. Gao et al. [17] investigated the tip clearance effect on the pressure ratio and the efficiency of a contra-rotating axial compressor. They found that the higher the tip gap, the lower the performance parameters.

Wang et al. [18] conducted an experimental investigation of the stall inception, which according to the data, is located at the tip of the second rotor. Simultaneously, the stall cell speed was measured at 35% of the compressor rotational speed. Nouri et al. [19] presented experimentally that two counter-rotating fans can produce a higher-pressure ratio, higher efficiency, and wider operational range; compared to the conventional configuration.

Alexiou et al. [20] designed a model for a contra-rotating turbomachinery component. This was used for one-dimensional simulations to predict engine performance. The model was run for a turbofan case and the results showed a 10% weight reduction of the engine and a 1.1% fuel decrease when the contra-rotating compressor was implemented. Gao et al. [21] conducted unsteady time accurate simulations to study the stall inception of a dual-raw counter-rotating axial compressor. The results indicated that the secondary leakage flow of the second rotor has a significant impact on the compressor unsteadiness. Moreover, the onset of the rotational stall was due to the breakdown vortex (created by first rotor), and this caused a blockage increase in the downstream rotor.

Liu et al. [22] investigated how the inlet distortion effect impacts on the stall behaviour of a transonic contra-rotating axial compressor performance. The results showed that the shockwave structures of the downstream rotor are more complicated than the one upstream. Finally, Knapke et al. [23] tried to implement boundary layer control to improve the counter-rotating axial compressor efficiency and the stall margin. The numerical simulations showed a 2.2% efficiency increase in the aspirated compressor case.

Based on literature review, only Dejour et al. [24] attempted an assessment of a non-axial counter-rotating compressor through computational fluid dynamic (CFD) simulations. The results

showed that the mixed flow contra-rotating compressor doubled the pressure rise while the efficiency slightly increased. Furthermore, the stall margin was improved, and the total axial length of the compressor was reduced.

2.2.2. Methodology

2.2.2.1. Baseline Compressor Design

A one-dimensional analysis is used to define the baseline rotor geometry and predict the performance characteristics of the radial compressor [24]. The full set of the equations used can be found in Fig. 2.7 and these can be split in two main parts. Firstly, the inlet conditions are chosen by the designer and all the flow parameters are computed at the leading edge (LE) of the impeller (hub & shroud). Secondly, the flow and geometry parameters are identified at the exit of the impeller, based on the chosen pressure ratio. Table 2.1 shows all the operational and geometry parameters of the baseline compressor design. The three-dimensional blade is designed in Ansys DesignModeler [25] (Fig. 2.8). The blade angle distribution is calculated using an optimization procedure focusing on the minimization of the blade surface losses. A 30deg rake angle is implemented at the exit of the impeller and splitter blades are also used at the 25% of the meridional flow path [26].

Table 2.1 – Geometry Parameter

Baseline Rotor	
Parameter	**Value**
N	40krpm
$\dot{m}$	0.24kg/s
PR	1.55
Z	8+8
D_{1h}	10.00mm
D_{1s}	50.00mm
D_4	124.90mm
β_{1h}	8.40deg
β_{1s}	36.30deg
β_{4h}	35.10deg
β_{4s}	45.00deg

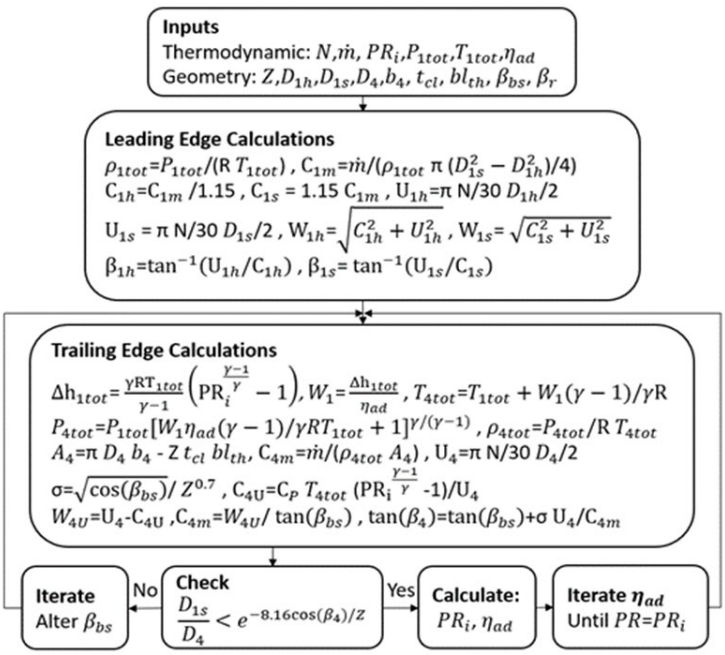

Figure 2.7 – One Dimensional Analysis

Figure 2.8 – Baseline 3D Blade

2.2.2.2. Contra-Rotating Compressor Design

The main step in designing the CRRC is to separate the compressor impeller into two individual rotors. The flow-path in the meridional plane is exactly the same as the one of the baseline geometry. Inlet and outlet geometry parameters are identical to make an objective comparison. This means that the LE and TE blade angles, both at the hub and shroud of the first and second rotor respectively, are kept the same as the corresponding angles of the baseline configuration. The location of the first rotor trailing edge is calculated as a percentage of the total blade length in the meridional plane (Fig. 2.9). In this study the 25% case is tested. This means that the first rotor accounts for the 25% of the baseline rotor blade, and the second one for the remaining 75%. This split point is chosen because the splitter blades in the baseline configuration start from the same location.

To design the three-dimensional blade, there are some geometrical parameters that need to be calculated. Starting from the first rotor, the outlet blade angle (hub / shroud) must be defined. After choosing the splitting point (25% in this case), the diameter at the hub and shroud are known and the procedure described in Fig. 2.7 can be applied. The only missing parameter is the pressure ratio of the first rotor. Having numerically analysed the baseline geometry, the inlet-to-outlet total pressure distribution is obtained (Fig. 2.10) and can be used to find the corresponding pressure ratio at the potential splitting point.

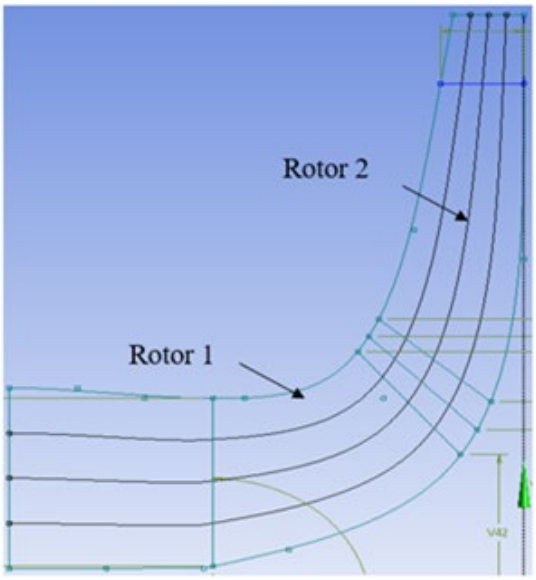

Figure 2.9 – Splitting line of Rotor 1&2

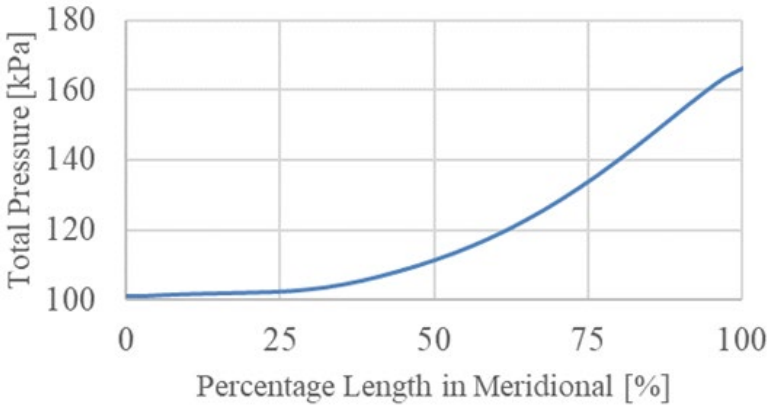

Figure 2.10 – Total Pressure Distribution from Inlet to Outlet

Based on the contra-rotating blade theory, the outlet flow conditions of the first rotor remain the same at the inlet of the second one. This is a key assumption to calculate the design parameters of the second rotor. Fig. 2.11 shows the theoretical velocity triangles which can be used to determine the blade angle (hub / shroud) at the LE of the second rotor. More specifically these angles can be computed by equations (1) and (2).

$$W_{3U} = U_3 + C_{2U} \quad (2.1)$$

$$\tan(\beta_3) = \frac{W_{3U}}{C_{2m}} \quad (2.2)$$

Fig. 2.12 presents the proposed contra-rotating configuration, in which the inner impeller rotates counter-clockwise and the outer rotor clockwise. It is important to highlight that the absolute value of the rotational speed is the same for both rotors (Table 2.2). In contra-rotating blade designs, it is common that the rotor-stator compressor is replaced by a rotor-rotor configuration and as a result the speed of the first rotor decreases. In this study, the approach of splitting the impeller into two parts is applied and therefore no speed changes are implemented. All the geometric and the operational design parameters are presented in Table 2.2. The number of blades being used in the first rotor is 8, the same as the number of full blades in the baseline geometry; and 15 blades are being used at the second rotor. Note that for the latter 15 blades are used as opposed to 16 to avoid any resonance phenomena.

Furthermore, the two rotors are placed at an average axial distance of 6mm. This study does not investigate the effect of gap between the two rotors. Finally, the blade angle distribution is calculated using the same optimization process as in the baseline configuration.

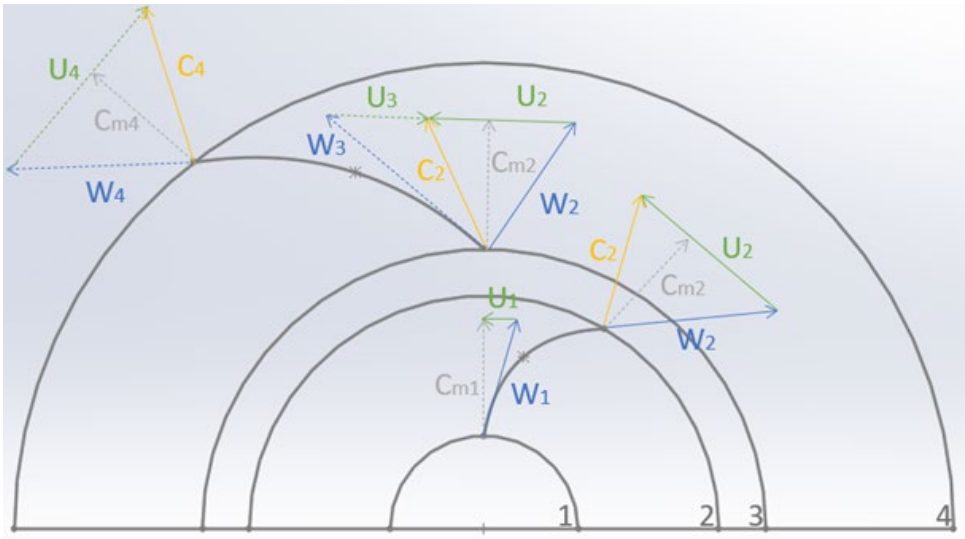

Figure 2.11 – Contra-Rotating Velocity Triangles

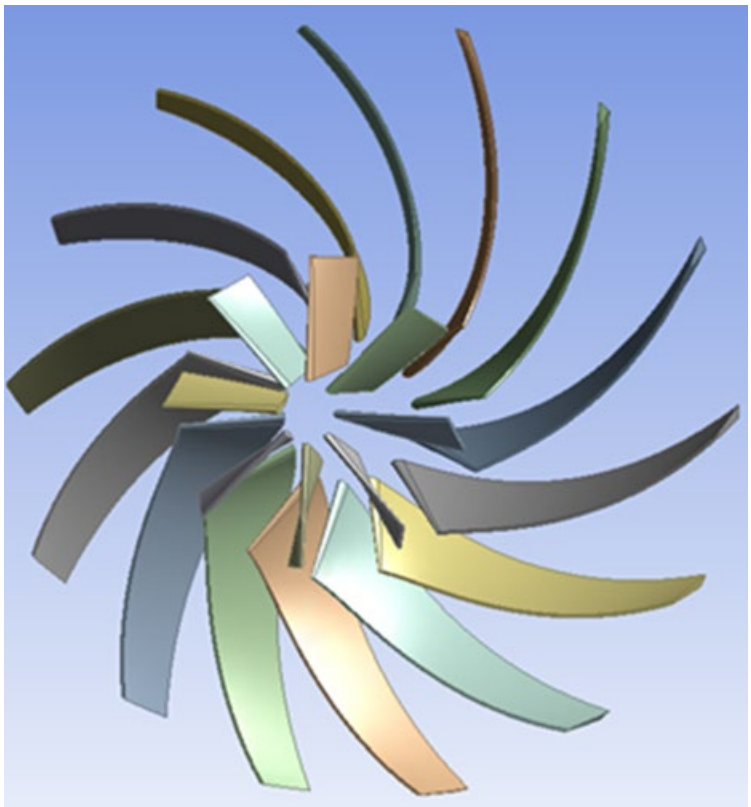

Figure 2.12 – Proposed CRRC

Table 2.2 – CRRC Geometry and Design Point Parameters

Rotor 1		Rotor 2	
Parameter	**Value**	**Parameter**	**Value**
N_{r1}	40krpm	N_{r2}	-40krpm
$\dot{m}_{r1}$	0.24kg/s	$\dot{m}_{r2}$	0.24kg/s
Z_{r1}	8	Z_{r2}	15
D_{1h}	10.00mm	D_{3h}	22.42mm
D_{1s}	50.00mm	D_{3s}	53.63mm
D_{2h}	16.19mm	D_{4h}	124.90mm
D_{2s}	51.14mm	D_{4s}	124.90mm
β_{1h}	8.40deg	β_{3h}	8.90deg
β_{1s}	36.30deg	β_{3s}	36.80deg
β_{2h}	11.70deg	β_{4h}	35.10deg
β_{2s}	36.60deg	β_{4s}	45.00deg

2.2.3. Computational setup

Numerical simulations are performed using ANSYS CFX (version 18.1) which is a high-performance commercial CFD software, ideal for turbomachinery numerical studies [28]. ANSYS TurboGrid is used to create the mesh around the rotor blades. The computational domain of the baseline configuration consists of two parts (Inlet and Rotor subdomains) while the CRRC is decomposed into four (Inlet1, Rotor1, Inlet2 and Rotor2) (Fig. 2.13). In both cases, the computational domain of the compressor includes the inlet duct and the impeller domain (baseline and CRRC). The volute is not being considered in this study as this would have an effect on the performance results. A steady-state, compressible simulation of a single channel is carried out, with a Mixing Plane interface for the CRRC case between rotors one and two [29].

Inlet total pressure and total temperature are set to 101.325kPa and 288.15K respectively, based on International Standard Atmosphere (ISA). The flow direction is chosen to be normal to the inlet boundary condition and the turbulent intensity is set to medium (5%) [30]. Mass flow outlet is the boundary condition at the exit of the computational domain. Based on Table 2.1 and 2.2, only the mass flow rate at the design point is simulated (0.24kg/s). The blade surfaces, including the hub and shroud regions, are set as walls where the no-slip condition is applied. No tip clearance is considered which means that the shroud is rotating with the blades. The working fluid is Air Ideal Gas, and the k-omega SST turbulence model is selected for this study. A grid independence analysis is conducted to find the ideal number of cells. Moreover, the mesh size must be chosen to satisfy the condition of y+=1 close to the wall. Fig. 2.14 shows the mesh convergence for both cases for six different mesh sizes. The higher the number of cells, the lower the inlet mass flow error, which is stable after approximately 150.000 cells. Therefore, the case with the mesh size of 200.000 cells is used to conduct the simulations. The generated mesh for the baseline and contra-rotating compressor is presented in Fig. 2.15.

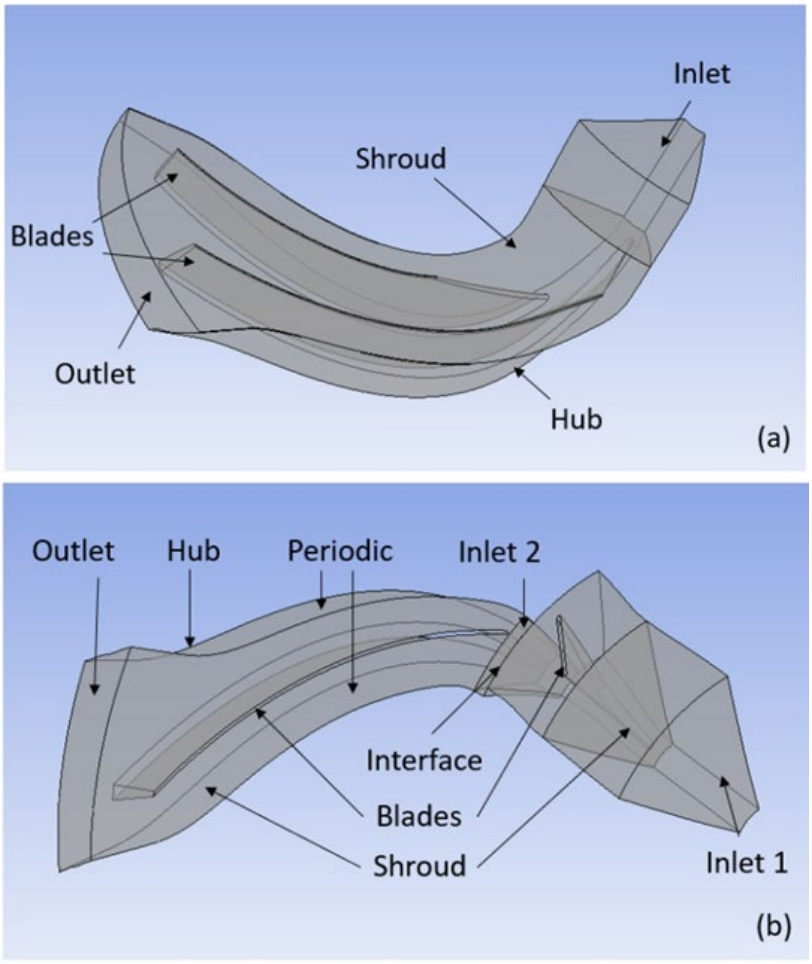

Figure 2.13 – Computational Domain for (a) the Baseline and (b) CRRC

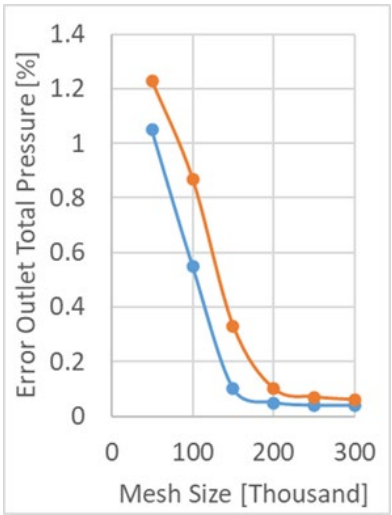

Figure 2.14 – Grid Analysis

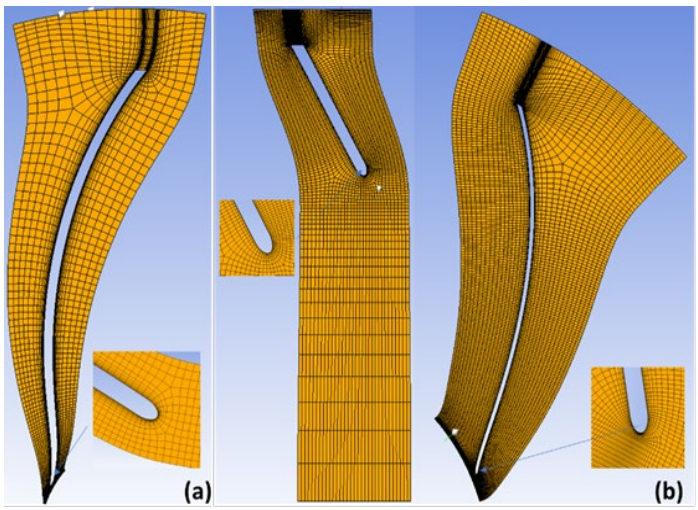

Figure 2.15 – Generated Mesh for (a) the Baseline and (b) CRRC

2.2.4. Results

The overall performance of the baseline and contra-rotating compressors is assessed in this section. This is done by studying the pressure, Mach number and entropy contours in different locations. Furthermore, the total-to-total pressure ratio and the total-to-total polytropic efficiency are calculated using equations (3.2.3) and (3.2.5).

$$PR_{t-t} = \frac{P_{out}}{P_{in}} \quad (2.3)$$

$$TR_{t-t} = \frac{T_{out}}{T_{in}} \quad (2.4)$$

$$\eta_{poly\,t-t} = \frac{\ln(PR_{t-t})}{\ln(TR_{t-t})} \frac{\gamma - 1}{\gamma} \quad (2.5)$$

Fig. 2.16 illustrates the blade-to-blade static pressure contour in the mid-span plane for the two tested cases. Based on the numerical data, there is a gradual increase of the static pressure in both cases which is something expected, as compressor configurations are being studied. However, it is apparent that the CRRC gives higher exit static pressure than the baseline one. Specifically, the flow exits the baseline and CRRC impeller at 140.1kPa and 144.6kPa (mass flow averaged) respectively, which is approximately a 3% increase. This means that the kinetic energy produced by the first rotor of the CRRC is converted to a higher static pressure by the second one.

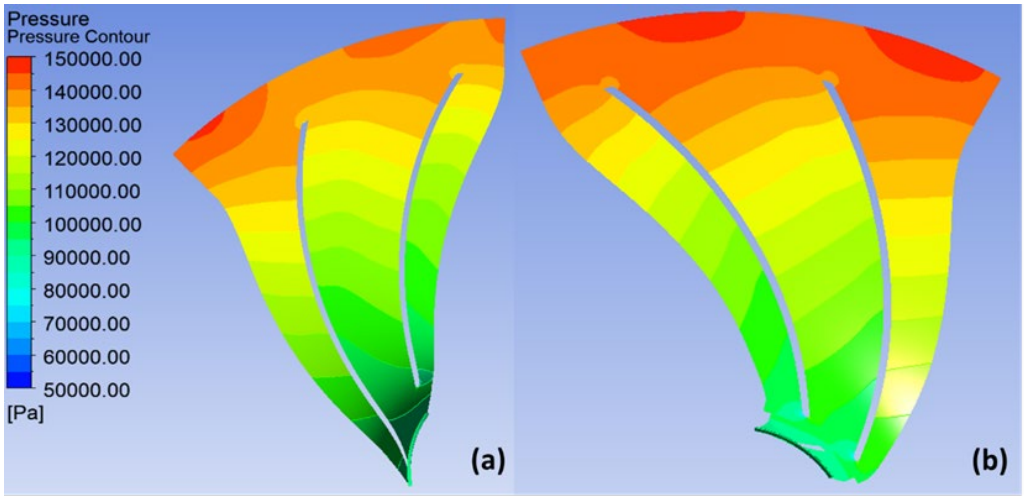

Figure 2.16 – Pressure Distribution in Mid-span for (a) the Baseline and (b) CRRC

Fig. 2.17 shows the blade-to-blade Mach number distribution in the mid-span plane for the baseline and the CRRC configurations. As mentioned in the methodology section, both the baseline compressor and CRRC first rotor run counterclockwise, while the CRRC second rotor runs clockwise. This is key to understand the flow field computational results and identify the pressure and suction side of each blade. Firstly, low speed structures can be observed at the trailing edge of the baseline impeller and the CRRC second rotor, both of them in the suction side of the blade. This means that the simulation in both cases follows the natural flow behaviour of a radial impeller. These low-speed structures are different between the simulated cases. In the baseline configuration, these instabilities are strong and occupy an important part of the channel. This makes the flow accelerate at the impeller exit which predicts a non-uniform velocity profile. On the other hand, the strength of these structures is reduced in the CRRC, decreasing the jet-wake flow effect. Therefore, a lower and more uniform velocity profile and a higher adiabatic efficiency is expected.

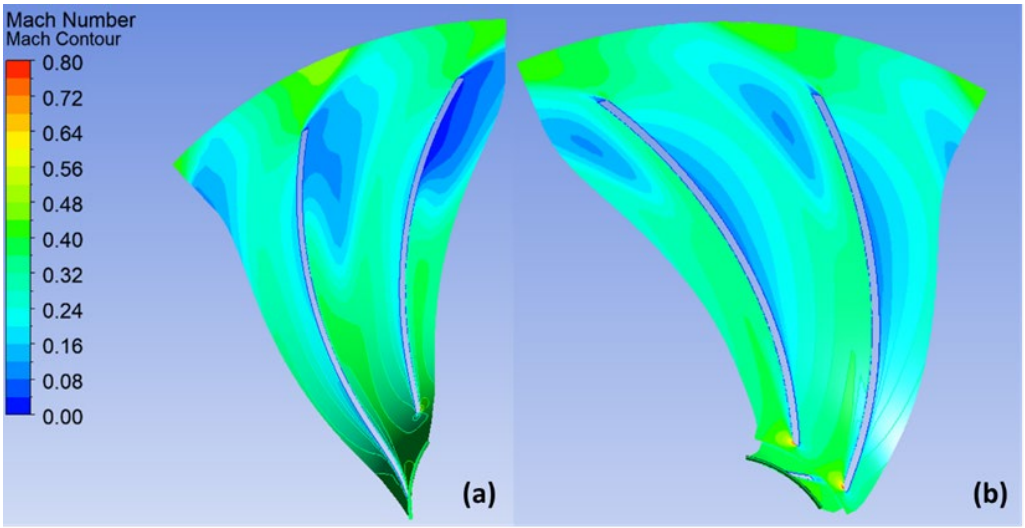

Figure 2.17 – Mach Number Distribution in Mid-span for (a) the Baseline and (b) CRRC

Figure 2.18 presents the normalized hub-to-shroud mass flow average velocity profile at the outlet of both compressor configurations. The profiles are split into three spanwise areas (0-0.5, 0.5-0.75 and 0.75-1) to understand their shape. From spanwise area ranges of 0 to 0.5, the CRRC profile shows lower velocity values and is more vertical when compared to the baseline one. The CRRC profile therefore presents a more uniform shape. It can be concluded that, at this spanwise area range, the influence of the CRRC is visible. At spanwise area ranges of 0.5-0.75, the rotating shroud starts having an effect on the shape of the profile. This is a transition area of the velocity profile. Finally, at spanwise area ranges of 0.75-1, both profiles start showing a very similar behaviour, which is due to the shroud. The overshooting behaviour shown by the CRRC profile, in Figure 2.18, at these are ranges, is due to the conservation of momentum in the hub-to-shroud direction.

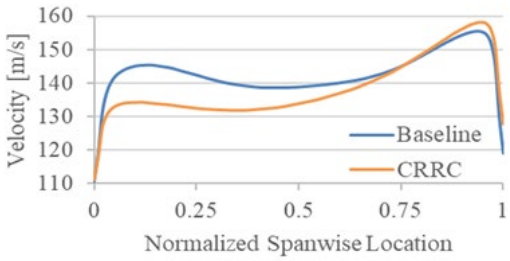

Figure 2.18 – Velocity Exit Profiles

Table 2.3 – Compressor Performance Parameters

Parameter	Baseline	CRRC
N	40krpm	40krpm/-40krpm
$\dot{m}$	0.24kg/s	0.24kg/s
Z	8+8	8 /15
PR_{t-t}	1.647	1.695 (+2.91%)
$\eta_{poly\ t-t}$	0.931	0.949 (+1.93%)

Figure 2.19 illustrates the hub-to-shroud static entropy contour at the outlet of the two compressor configurations. The advantage of the CRRC design, especially in terms of the efficiency, can be observed in this figure. Entropy losses associated with jet-wake flow structures are approximately 40% higher in the baseline configuration according to the graph. Furthermore, the CRRC outlet flow field is more uniform, once again proving the advantageous effects on the compressor performance. These findings can be validated by the mass flow average calculations of the performance parameters for the two compressor configurations, as shown in Table 2.3. The CRRC has a 2.91% higher total-to-total pressure ratio and an 1.93% increase in the adiabatic efficiency.

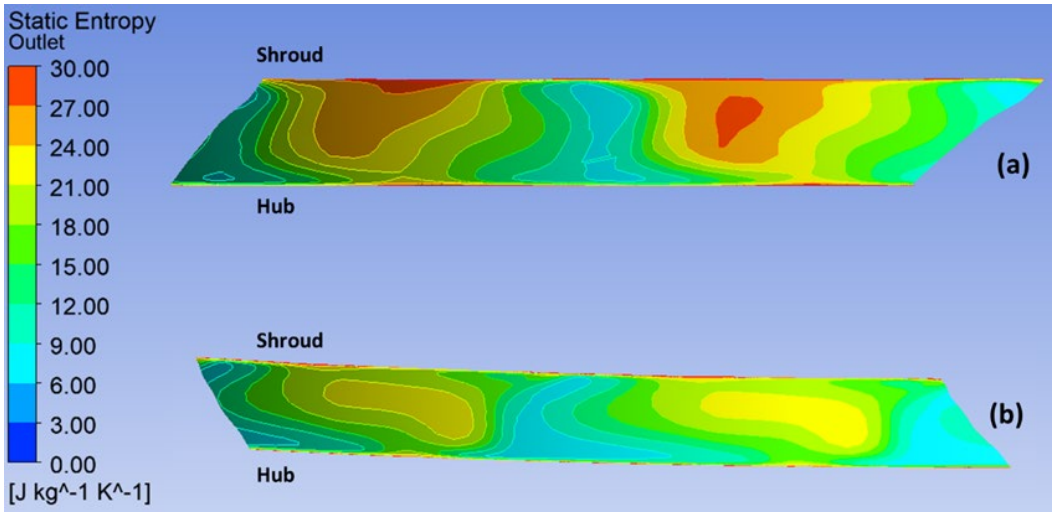

Figure 2.19 Static Entropy Distribution at the Outlet for (a) the Baseline and (b) CRRC

2.3. ESR8

2.3.1. Contribution on MILD combustion

MILD combustion was identified as one of the suitable techniques to be employed in micro gas turbines combustion chambers. Further developments of this new technology need to be supported by affordable CFD tools. However, modelling this regime is more difficult than traditional flames because of the strong coupling between turbulent mixing and chemical kinetics. The use of finite-rate approaches has therefore become an essential requisite for CFD. As a consequence, a large number of stiff ordinary differential equations (ODEs) needs to be solved in each computational cell, making finite-rate models expensive, especially for realistic-sized combustion systems.

However, many well-known fundamental studies demonstrated that the truly active chemical dynamics involves a limited number of chemical pathways. This consideration created many opportunities to tackle the computational cost burden of detailed kinetics. Among the proposed techniques, Sample-Partitioning Adaptive Reduced Chemistry (SPARC), was recently proposed to couple adaptive chemistry and machine learning. This methodology brings the advantages of the dynamic reduction techniques, i.e., the mechanism size is tailored to the local conditions, and simultaneously saves the cost associated to the on-the-fly adaptive reduction, which can be prohibitive when large kinetic mechanisms are used. SPARC methodology has been developed and tested for simulating MILD combustion in JHC burners, with results showing speed-up factors for the chemical step of ≈ 2 using a detailed mechanism accounting of 36 species.

References – Chapter 2

[1] Tiwari, R., N., Reggio, F., Renuke, A., Pascenti, M., Traverso, A., Ferrari, M.L., 2022, "Performance Investigation of a Bladeless Air Compressor" J. Eng. Gas Turbines Power, Vol-144(9) Doi.org/10.1115/1.4054945.

[2] Tiwari, R., Eleftheriou, K., Ferrari, M.L., Efstathiadis, T., Traverso, A., and Kalfas, A., 2022, "Numerical Investigation of Bladeless Compressor on Different Disk Spaces and Diffuser Configurations" J. Eng. Gas Turbines Power, Vol-145(01). Doi.org/10.1115/1.4055705.

[3] Epstein, A. H., 2004, "Millimeter-Scale, Micro-Electro-Mechanical Systems Gas Turbine Engines," ASME J. Eng. Gas Turbines Power, 126(2), pp. 205–226

[4] Rice, W., 1963, "An Analytical and Experimental Investigation of Multiple Disk Pumps and Compressors", J. Eng. for Power 1963. Pp. 191-198.

[5] Renuke, A., Vannoni, A., Pascenti, M., and Traverso, A., 2019, "Experimental and Numerical Investigation of Small-Scale Tesla Turbines," ASME J. Eng. Gas Turbines Power, 141(12), p. 121011.

[6] Renuke, A., Reggio, F., Traverso, A., and Pascenti, M., 2022, "Experimental Characterization of Losses in Bladeless Turbine Prototype," ASME J. Eng. Gas Turbines Power, 144(4), p. 041009.

[7] Dewar, B., Tiainen, J., Jaatinen-V€arri, A., Creamer, M., Dotcheva, M., Radulovic, J., and Buick, J. M., 2019, "CFD Modelling of a Centrifugal Compressor With Experimental Validation Through Radial Diffuser Static Pressure Measurement," Int. J. Rotating Mach., 2019, pp. 1–12.

[8] Menter, F. R., 1992, "Influence of Freestream Values on k-Omega Turbulence Model Predictions," AIAA J., 30(6), pp. 1657–1659

[9] Wasala, S. H., 2016, "Numerical Analysis and aeroacoustics Simulation of Noise from Wind Turbines," Ph.D. Thesis, the University of Auckland, 2016.

[10] Wasala, S. H., Xui, Y.,Stevens, L.,Persoons, T., 2021, "Aeroacoustics Noise Prediction from Contra-Rotating Cooling Fan Used in Data Center Cooling System", Conference, AIAA Aviation 2021 Forum, Doi:10.2514/6.2021-2313.

[11] Cumpsty, N. A. 1977 "A critical review of turbomachinery noise", Journal of Fluids Engineering, Vol-99(2) 278-293.Doi.org/10.1115/1.3448745

[12] Lucifredi, A., Noceti, D., Ferraro, A., Silvestri, P., and Ortenzio, G., 2011 "Acoustic and Vibrational Characterization for Noise Reduction of a Piaggio P180 Cockpit Blower" 8th International Conference on Condition Monitoring and Machinery Failure Prevention Technologies, Cardiff, UK.

[13] Sharma, P., and Adekoya, A., (1996). A Review of Recent Research on Contra-rotating Axial Flow Compressor Stage, proceedings of ASME 1996 International Gas Turbine and Aeroengine Congress and Exhibition, Birmingham, UK.

[14] Wilcox, W., (1952). An analysis of the potentialities of a two-stage counter-rotating supersonic compressor.

[15] Pundhir, S., and Sharma, P., (1992). A Study of Aerodynamic Performance of a Contra-rotating Axial Compressor Stage, Defense Science Journal.

[16] Furukawa, A., Shigemitsu, T., and Watanabe, S., (2007). Performance test and flow measurement of contra-rotating axial flow pump, Journal of Thermal Science.

[17] Gao, L., Li, X., Feng, X., and Liu, B., (2012). The Effect of Tip Clearance on the Performance of Contra-rotating Compressor, proceedings of ASME Turbo Expo 2012, Copenhagen, Denmark.

[18] Wang, Z., Yuan, W., Li, and Q., Lu, Y., (2012). Experimental Investigation on the Stall Inception of a Counter-rotating Compressor, proceedings of ASME Turbo Expo 2012, Copenhagen, Denmark.

[19] Nouri, H., Danlos, A., Ravelet, F., Bakir, F., Sarraf, C., (2013). Experimental Study of the Instationary Flow Between Two Ducted Counter-Rotating Rotors, Journal of Engineering for Gas Turbines and Power.

[20] Alexiou, A., Roumeliotis, I., Aretakis, N., Tsalavoutas, A., and Mathioudakis, K., (2012). Modelling Contra-Rotating Turbomachinery Components for Engine Performance Simulations: The Geared Turbofan With Contra-Rotating Core Case. Journal of Engineering for Gas Turbines and Power.

[21] Gao, L., Li, R., Miao, F., and Cai, Y., (2015). Unsteady Investigation on Tip Flow Field and Rotating Stall in Counter-rotating Axial Compressor, ASME Journal of Engineering for Gas Turbines and Power.

[22] Liu, H., Wang, Y., Xian, S., and Hu, W., (2016). Effect of Inlet Distortion on the Performance of Axial Transonic Contra-rotating Compressor, proceedings of IMech Part G: J Aerospace Engineering.

[23] Knapke, D., Turner, G., List, G., Galbraith, S., Beach, T., and Merchant, A., (2008). Time Accurate Simulations of a Counter-rotating Aspirated Compressor, proceedings of ASME Turbo Expo 2008, Berlin, Germany

[24] Dejour, Q, & Vo, HD., (2018). Assessment of a Novel Non-Axial Counter-Rotating Compressor Concept for Aero-Engines, Proceedings of the ASME Turbo Expo 2018, Oslo, Norway.

[25] Japikse, D., (1996). Centrifugal Compressor Design and Performance.

[26] ANSYS, ANSYS Workbench, (2018). ANSYS Academic Research, Release 18.1

[27] Mojaddam, M., Pullen, K., (2019). Optimization of a Centrifugal Compressor Using the Design of Experiment Technique, Applied Sciences 2019.

[28] ANSYS, CFX Theory Guide, (2018). Basic Solver, ANSYS Academic Research, Release 18.1

[29] De, G., Grazia, M., Ficarella, T., Fontanarosa, A., (2017). Numerical investigation of the performance of Contra-Rotating Propellers for a Remotely Piloted Aerial Vehicle. Energy Procedia.

[30] Ashrafi, F., Michaud, M., and Vo, H. D., (2016). Delay of Rotating Stall in Compressors Using Plasma Actuators. ASME Journal of Turbomachinery.

3. System oriented optimisation

3.1. ESR2

3.1.1. Introduction and motivation

Energy Storage Systems (ESSs) are a crucial technology that is needed to increase the share of Variable Renewable Energy (VAR), mainly wind and solar. So far, the available technologies cannot cope with the high demand for energy storage. Energy storage technologies can be classified according to the form in which energy is stored: *electrical, electrochemical, mechanical, and thermal.* Only a few ESSs are suitable for storing a high amount of energy, such as Pumped Hydroelectric Storage (PHS). Nevertheless, PHS is highly constrained on local geographic constrained features as it requires the presence of both water streams and natural/artificial basins with large differences in altitude. In the same way, Compressed Air Energy Storage (CAES) shares similar limitations since its installation requires to have large caverns available.

Many other ESSs are available but they are presently applicable on the small scale only, such as electrochemical batteries, flow batteries, superconducting magnetic energy, flywheels, capacitors, and supercapacitors. With such limitations, the previous ESSs seem to be more feasible for grid balance than for large-scale energy storage.

In recent times, with the introduction of a higher share of VAR, chemical energy storage is seen as the pathway to store large amounts of energy in the form of hydrogen and derivatives. Power-to-Hydrogen (P2H2) is a chemical energy storage that uses renewable energy to drive an electrolyser to produce hydrogen through water electrolysis. The potential of hydrogen is seen from the fact that it can be produced wherever there are water and renewable energy sources available. In the past, hydrogen has been widely produced by methane-steam reforming and it has been mainly used by the fertilizer and refinery industries. In addition, other ways of producing hydrogen exist, and depending on their origin, they are classified in different colours. Table 3.1 shows the origin and associated colour for the different hydrogen production pathways.

Table3.1. – Classification of hydrogen production by colours.

Terminology	Technology	Feedstock/ Electricity Source	GHG Footprint
Green	Electrolysis	Wind / Solar / Hydro / Geothermal / Tidal	Minimal
Purple/Pink		Nuclear	Medium
Blue	(Natural gas reforming or gasification) + (CCSU)	Natural gas / coal	Low
Turquoise	Pyrolysis	Natural gas	Solid carbon
Grey	Natural gas reforming		Medium
Brown	Gasification	Brown coal (lignite)	High
Black		Black coal	

Hydrogen is the lightest chemical element, and it is only found when bounded with other chemical elements forming a compound. Hydrogen needs to be produced (table 3.1), enables energy to be carried and can be converted back into any other form of energy. Hence, hydrogen is categorised as an *energy vector*. Figure x highlights the many uses of hydrogen. It serves for production of heat, power, or for transportation. This is what is called in literature as Power-to-H_2-to-X, where X means heat, power, or mobility. This subject has risen a lot of attention from different public and private cooperations with the aim to develop the hydrogen economy. The fully deployment of it would help to achieve the targets on energy independency and decarbonisation of different sectors and applications

where electrification cannot be achieved. In this regard, governments around the world have released their hydrogen roadmaps [1] [2] [3] [4].

This section is focused on the use of (micro) gas turbines as thermal energy systems that allow the conversion of hydrogen into power through the combustion of H_2 in a combustion chamber. This is named Power-to-Power (P2P). Therefore, from now on, this section will only focus on the production and use of hydrogen for power generation. Chapter 1 gives a detailed introduction on the thermodynamics of the Brayton cycle along with the different components that form the micro gas turbine (mGT).

Next sections will explore the feasibility of having P2P-ESS with mGTs, assessing the techno-economic challenges associated with this ESS technology along with the different results that have been conducted by ESR2.

3.1.2. Targets and Approach

The targets of ESR-2 come from the motivation of exploring the use of the mGT within a P2P-ESS as a way of storing large amounts of energy to cope with the higher share of renewable energy. As for now, the energy market systems still rely on fossil fuels whose CO_2 footprint is much higher that what it is considered on the limit of a sustainable power generation system from the EU taxonomy guidelines (< 270 gr CO_2/kWeq) [5]. Therefore, the production and use of hydrogen for power generation is vital for the future of the (micro) gas turbine to remain competitive and respectful with the environment. The main aim of ESR-2 is, therefore, to find the optimum layouts of the P2P-ESS that will bring the most advantageous operation of it. This target will be found by following the next steps:

- *State-of-Art* of electrolysers.
- Thermodynamic analysis of P2P-ESS with mGTs.
- Techno-economic analysis of different configurations of the P2P-ESS and its integration with other technologies, such as BESS.
- Performance analysis of the (micro) gas turbine for high performance, reliability, and low-emission thermal power system.

So far, the three first points have been already addressed by ESR-2 and they will be detailed in the next section. ESR-2 have been dealing with the modelling of each of the systems involved, put them together in a software environment (Python), and developed the system integration. This inhouse software allows to carry out techno-economic analysis of P2P ESS as it will be described in the next sections.

3.1.3. Power-to-H2-to-Power Energy Storage System with mGTs

A Power-to-H2-to-Power (P2P) energy storage system uses the surplus of VRE to produce H2 through water electrolysis in an electrolyser. Later, H2 is stored for its later use when power is demanded, and it cannot be supplied by VRE. This energy storage system is formed by the following systems:

- Variable Renewable Energy
- Electrolyser
- Storage media
- Power system

3.1.3.1 Variable Renewable Energy

Regarding the VRE, the main energy sources are both solar and wind. The main technologies associated and considered for the inhouse developed software are PV Solar and Wind Turbine. Therefore, only green hydrogen is considered for the production of hydrogen in the P2P. The system design of these technologies is carried out by the open-source software System Advisory Model (SAM) software developed by the National Renewable Energy Laboratory (NREL) [6] is used for the modelling and design of renewable energy sources. It is a performance and financial model software

tool able to estimate system performance and cost of energy for grid-connected power projects based on installation/operating costs and on system design parameters set by the user. SAM has a dedicated Python package, PySAM [7], which can be called from a Python code to carry out SAM simulations and access SAM's default values and input variables. PySAM is a wrapper around the SAM library that groups the C API functions into modules either by technology or financial models. There are two ways to feed input data into PySAM; either by setting up each input parameter in each section in the environment of Python, or by delivering a JSON file with all input data that can be obtained from SAM software. The latter option is used in the software developed in this work since another option would mean to replicate the already built SAM Software's interface, which is open-source and available to download.

3.1.3.2 Electrolyser

Water splitting is the chemical reaction in which water is broken down into its molecules, oxygen and hydrogen.

$$H_2O + \text{energy} \rightarrow 2H_2 + O_2$$

Water is one of the most abundant compounds on Earth and it can be used to produced H_2 through water splitting processes such as electrolysis, thermolysis and photolysis. This chemical reaction does not take place spontaneously and it is endothermic but, on the contrary, energy input is needed to drive the formation of hydrogen and oxygen from water: electrolysis when the energy input is electricity. ESR-2 has released 3 scientific articles where he deals with the water electrolysis fundamental and electrochemical modelling of the electrolysers.
Three main types of electrolysers are currently keeping most of application interests:

- Alkaline EC
- Proton Exchange Membrane (PEM) EC
- Solid Oxide (SO) EC

Alkaline electrolyser is the most mature electrolyser technology. The main advantage of this technology compared to the others is the availability of the construction materials at an inexpensive price. The electrochemical reactions that happen in an alkaline electrolyser, at anode and cathode, are shown in Table 4.1.2. The electrodes are immersed in the liquid electrolyte, a highly concentrated alkaline aqueous solution made of concentrated potassium hydroxide. The anode is usually made of nickel or nickel-based catalyst while the cathode is made of nickel or nickel-based catalyst. A porous solid material (diaphragm) allows transport of hydroxyl ions (OH^-) between the electrodes and exhibits a low permeability to oxygen and hydrogen. In practical operation, the cell voltage lies in the 1.3 – 2.0V range.

Proton exchange membrane (PEM) systems are based on the solid polymer electrolyte (SPE) concept for water electrolysis introduced in the 1960s. The PEM electrolysers that are commercially available today, are more flexible and tend to have smaller footprint than the alkaline electrolysers. In PEM cells, there is no liquid electrolyte as such. Only deionized (water circulates through the anodic compartment of the cell. The central component of the cell is a thin (≈ 0.2 mm thick) membrane of a proton-conduction polymer electrolyte. The membrane is used for the double purpose of carrying ionic charges and separating electrolysis products. The most popular membrane material is a perfluoro sulfonic acid (PFSA) ionomer. On both sides of the membrane, two porous catalytic layers are coated. These catalytic layers are connected to an external DC power source that provides electrical energy for the reaction. The electrochemical half-cell reactions that happen in a proton exchange membrane cell, at anode and cathode, are shown in Table 3.2.

Water molecules are oxidized at the catalytic anode (usually made of unsupported Ir-based oxide particles), leading to the production of dioxygen and protons. Oxygen evolves in the gaseous phase and is extracted from the cell. Electrons circulate in the external circuit and hydrated protons migrate across the polymer membrane, down to the cathode (usually made of unsupported Pt particles or of carbon-supported Pt nanoparticles) where they are reduced by the electrons injected by the external DC power supply. As a result, dihydrogen is produced.

Table 3.2 – Half-cell reactions for each type of electrolyser.

	Anode	Cathode
AEC	$4\,OH^- \rightarrow O_2 + 2H_2O + 4e^-$	$4H_2O + 4e^- \rightarrow 2H_2 + 4OH^-$
PEMEC	$H_2O(l) \rightarrow \frac{1}{2}O_2(g) + 2H^+ + 2e^-$	$2H^+ + 2e^- \rightarrow H_2(g)$
SOEC	$O^{2-} \rightarrow \frac{1}{2}O_2(g) + 2e^-$	$H_2O + 2e^- \rightarrow H_2 + O^{2-}$

Solid oxide electrolyser belongs to the group of the so-called High Temperature Steam Electrolysis (HTSE). Electrolysis of water can be performed either at low temperature or high temperature, using liquid water or steam. However, the main advantage of this technology is that the dissociation of steam requires less energy [8]. In addition, the amount of electrical energy required decreases as temperature increases. The operating temperature is within the range of 700-900ºC. The technology is immature and has only been tested at laboratory scale. However, the working principle is the reverse functioning of a Solid Oxide Fuel Cell (SOFC), from which knowledge on materials and operation is taken. The half-cell's reactions are shown in Table 3.2.

A summary of the main characteristics and performance of the 3 electrolyser technologies presented previously can be visualized in Table 3.3. Current – voltage curves measured on different electrolysis cells can show the performance variances of different electrolyser technologies. Figure 3.1 shows typical ranges of cell voltage and current density for electrolysers' sizes that can be found in industry nowadays.

Due to the high attention risen by the development of high efficiency, reliability, and low maintenance of the electrolyser in the recent years, the latest development trends are the reduction of CapEx (for example, increasing current density, find cheaper materials with wider availability, etc.) and OpEx (for example, increasing efficiency, pressurizing electrolyser systems, etc.). Due to the different electrolyser's working principle, compositions, and operating conditions, the research and development will be focused on different electrolyser's elements depending on the electrolyser type. More information about it can be found at [8] [9].

Table 3.3 – Characteristics of different electrolyser's technologies [10].

Technology	AEC	PEMEC	SOEC
Development Stage	Commercial lager scale plant	Prototypes and commercial units	Laboratory stage units
Conventional temperature range (ºC)	60 – 80	50 – 80	650 – 1000
Conventional pressure range (bar)	1 – 30	Up to 40	1 – 8
Electrolyte	25 – 35 % KOH	Nafion Membrane	$Y_2O_3 + ZrO_2$
Conventional current density (Acm^{-2})	0-5 – 1.0	2.0 – 3.0	1.0 – 2.0
Stack energy consumption ($kWh/kg\ H_2$)	51	70 – 55	41 – 40
Stack Efficiency (LHV-%)	77	57 – 72	98
Durability (h)	100,000	50,000 – 90,000	> 4500
Load cycling	Medium	Good	No data available
Stop/go cycling	Weak	Good	Weak
Cost (€/kW)	800 to 1300	1200 to 2000	Not commercialized

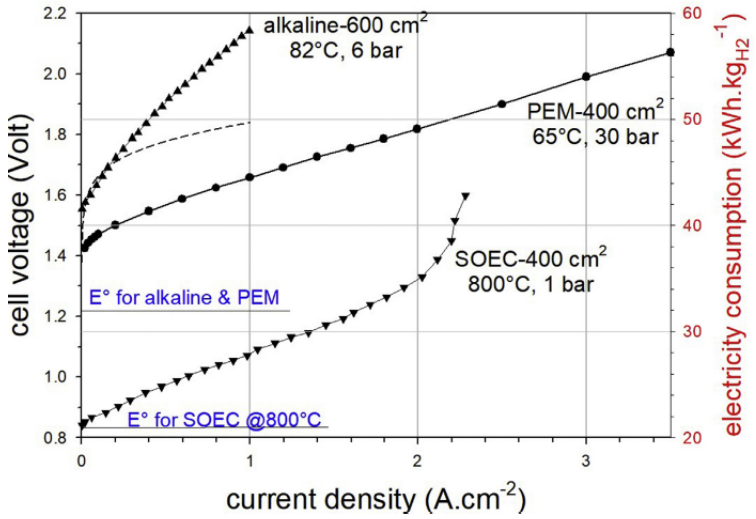

Figure 3.1. – Comparison of typical i-V curves measured in Alkaline, PEM and SO water electrolysis cells [9].

3.1.3.3 Storage media and transportation

Hydrogen, as energy carrier, can be stored in different ways and for as long as it requires. Nonetheless, the term-period for which hydrogen is most attractive as energy storage media is in the order of days to months.

Hydrogen is well-known for being the fuel with the highest gravimetric density but with the counterpart of having one of the lowest volumetric densities at ambient conditions among conventional fuels. Hence, different storage strategies are applied to overcome the low volume density of hydrogen, with solutions for its three states of matter: **gas**, **liquid** and **solid**. It is common to liquefy hydrogen or to increase the gas pressure to gain volume density. However, all these processes are highly energy intensive, reducing considerably the final round-trip efficiency of the energy system.

Figure 3.2 shows the different volume energy density for different states of hydrogen and other fuels with similar applicability. Volume energy density of hydrogen at ambient conditions compared to the others, such as methane, ethanol, or ammonia, clearly states the challenges presented for efficient storage of hydrogen. Hence, hydrogen storage remains as the most challenge process for the deployment of an energy market based on hydrogen.

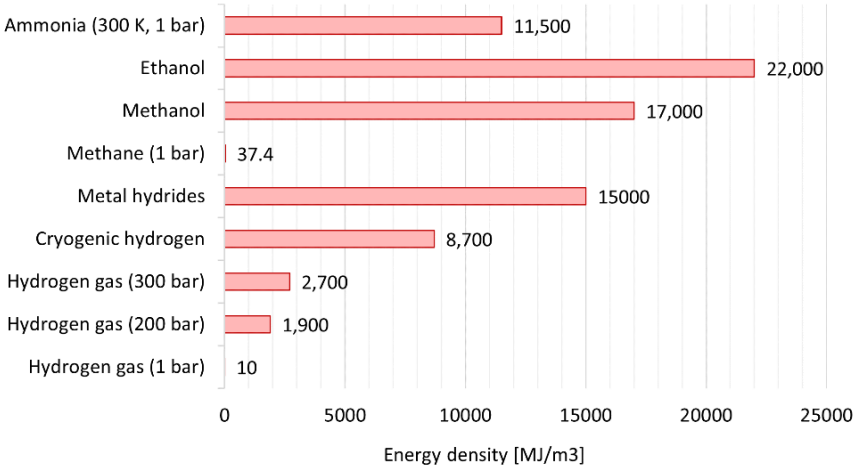

Figure 3.1. – Energy density of different fuels [10].

Compressed H_2 is the most usual method to store and distribute hydrogen at relatively small quantities, 5 to 10 kg/H_2 per vessel. The pressure to which hydrogen is compressed depends on both whether it is transported and the final application for what it will be used. Keeping in mind that the higher the target pressure, the higher the capital and operational expenditure, there is a trade-off between application storage space available and costs. Hence, mobility applications, such as cars or forklifts, the storage available is limited and the highest pressure is achieved to increase hydrogen volume density (≈ 700 bar). On the opposite, stationary applications, such as small auxiliary power system, the storage available is not often a problem and lower hydrogen volume densities are possible (150 bar to 500 bar).

Considering the H_2 pressure at the exit of the electrolyser (Table 3.3), compressors to deliver high-pressure H_2 are required to work with high level pressure ratios, often even higher than 30. Hence, not every type of compressors is adequate for this purpose. More details about the different compressors that can be used are found in Reference [9].

At ambient pressure, 1.013 bar, hydrogen is in the **state of liquid** when its temperature is equal or below 20.37 K [11]. Nonetheless, hydrogen is produced closely to ambient conditions as stated in Table 3, from 1 to 30 bar and from 303 to 343 K. Hence, cryogenic plant concept is needed in order to reduce hydrogen temperature to such extreme conditions, even further down from the coldest places in Earth. Even though the high energy intensive processes to liquefy hydrogen, and the more auxiliary equipment to keep it at those conditions, the direct benefit of dealing with cryogenic hydrogen is the increase in density, going from 0.083 kg/m^3 (at 1.013 bar and 295 K) to 76.2 kg/m^3 (at 1.013 bar and 15K) [11].

One of the most recent projects to shed light on to the purpose of reducing power consumption is the H2020 project *IDEALHY* [12], completed in 2013. Main results from this project were the proposal of a cryogenic hydrogen plant with a power consumption of around 6.7 kWh/kg H_2, which is almost half with regard already built and in operation liquefied-H_2 plants [10]. Furthermore, recent investigations have already showed that lower power requirement, 5.9 kWh/kg H_2, can be achieved with further optimisation [10].

The configuration of metals or alloys with hydrogen leads to the formation of a new compound, named ***Metal Hydride***. The new compound is characterized by its high volumetric density, as shown in Figure 3.3, reaching values over 115 kg/m^3. As a chemical reaction, the loading and unloading of hydrogen is mainly influenced by thermodynamics and kinetics processes.

Metal hydrides can reversibly store (absorbs) large amounts of hydrogen, simultaneously releasing heat during the absorption process. Conversely, hydrogen is released (desorbed) when heat is delivered to the compound.

3.1.3.4 Hydrogen consumption (mGT)

There are several applications where an energy carrier such as hydrogen can be used: mobility, feedstock, power generation, and others [3,13-16]. Nevertheless, in this work, only power generation is considered in order to provide more focused conclusions about the feasibility and interest of P2P applications.

Fuel Cells (FC) are usually recognised as the most interesting technology to produce power from hydrogen [17]. Nonetheless, with the recent interest triggered by hydrogen technologies to decarbonise many sectors, other power technologies are being upgraded to enable the direct utilisation of hydrogen as main fuel. GTs are one of the technologies that is catching up more quickly with FCs, thanks to the lessons learned from hydrogen co-firing in the last decades [18] [19] [20] [21]. However, challenges for a flexible and interrupted operation with 100% hydrogen combustion still remain; an overview of the state-of-art of hydrogen operation of GTs is available in a recent report by the European Turbine Network [22]. In addition, several projects are underway to deal with the design and operation of the first 100% H_2 GT and mGT in Europe, such as the HYFLEXPOWER [23] and ROBINSON [24].

This study is focused on mGTs rather than larger GTs < 500 kWe. These smaller engines exhibit two main differences with respect to the larger units, brought about by the need to use radial machinery as a consequence of the low volumetric flow rate of air through the engine (compressor and expander). Indeed, the utilisation of single stage radial compressors limits the pressure ratio of the engine to values lower than 4 (approximately) and the lack of internal cooling systems built into radial expanders limits turbine inlet temperature to values not higher than 950 ºC. These key design parameters are in contrast

with pressure ratios (≈ 20-25) and combustor outlet temperatures (1500-1600 ºC) commonly found in heavy-duty gas turbines. As a consequence of this, mGTs typically rely on recuperative cycle layouts to attain higher thermal efficiency and they also need specific combustor designs to enable operation on 100% H_2, even though this can largely leverage on the experience gained with larger engines. As far as this work is concerned, only mGTs burning 100% H_2 are considered, even if this capability is not offered by any commercial product in the market yet.

3.1.4. Results

ESR2 has already conducted studies on the feasibility of the P2P ESS. The first analysis focused on the thermodynamic analysis of the different options that exist for the different systems that can be implemented for each of the processes described above. This study has been delivered in the form of journal paper in the International Journal of Hydrogen Energy [10]. A market research study has been conducted to find out the different commercial systems that exists for each process involved in the P2P.

The figure of merit to assess the thermodynamic adequacy of each option is the named *round-trip efficiency* (RTE), which is defined as the ratio from the energy delivered back to the user (or the grid) to that taken from the primary source of electricity, and expressed as follows:

$$RTE = \frac{E_{in}}{E_{out}} \cdot 100 \quad (3.1)$$

Out of the market research, the following options were selected to form the P2P system to investigate the RTE.

- Production: AEC, PEMEC and SOEC.
- Storage and distribution: gas compressed at 500 bar, liquefied-H2, and metal hydride + 200 km of transportation by a Fuel-Cell Electric Truck (FCET).
- Power generation: micro-gas turbine (30 kW).

The combination of the different options yields 9 combinations, and for each of them the RTE efficiency was calculated. Figure 3.3 and Figure 3.4 show the energy balance conducted of each combination as well as the RTE. From the energy consumption's side, the electrolyser is the system that clearly produces the highest difference amongst the different combinations. SOEC states out as its efficiency is around 20 to 30 percentage points higher than the other two types. Thus, the energy consumption is lower than the other types. After, the storage becomes the second most important energy consumption in a P2P ESS. Liquefaction of hydrogen comes with the penalty of higher energy consumption and lower RTE. From the energy production's side, the mGT chosen for each combination is the same. However, it is of utmost importance to remark that only around 12 kWh out of 33.33 kWh is obtained from this engine. Rest of the power is in the form of heat in the exhaust gases, but heat is left out from the RTE calculation.

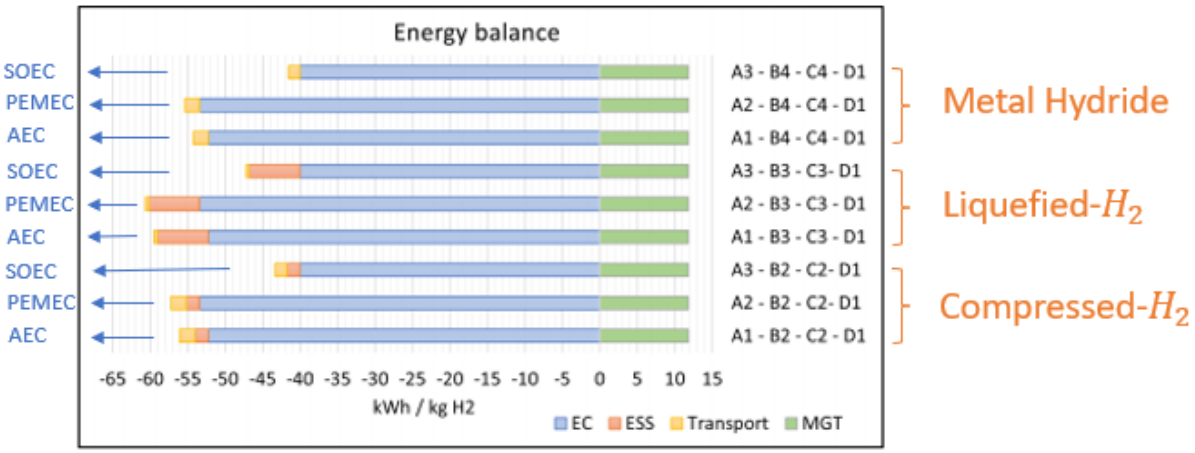

Figure 3.2 - Energy balance for the P2P solutions considered in the study carried out by ESR 2 [10].

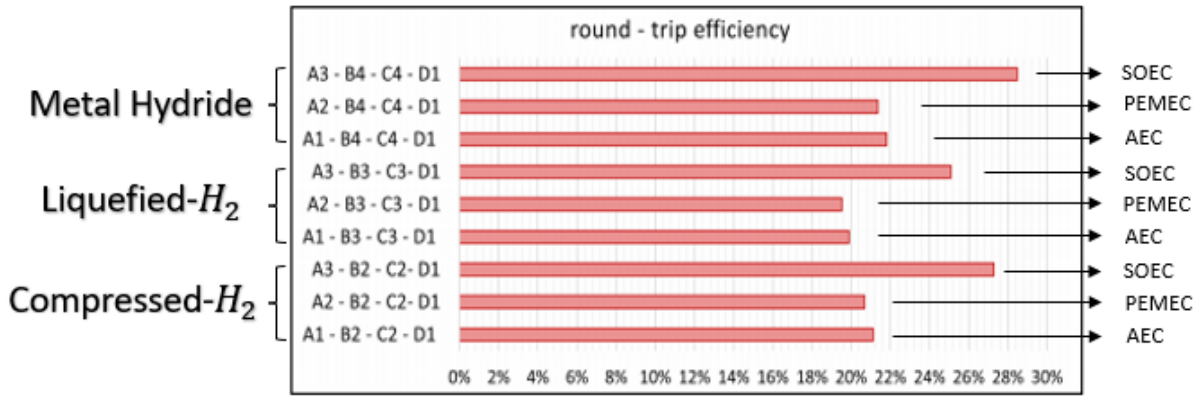

Figure 3.3 - Round-trip efficiency for the P2P solutions.

The RTE of the different combinations studied never surpasses 30%. Furthermore, the options that are closer to 30% are those with a SOEC, which is far to be a mature technology yet. If either AEC or PEMEC are considered, the RTE goes down to 22%. It is to be mentioned that these numbers were obtained considering that each of the systems would be working at full load, which means that the potential RTE would be reduced when being installed and following the application's power demand.

The conclusions that were drafted from this study are that the highest RTE possible that can be achieved with a P2P with a mGT is of 28%, but only 22% when considering mature technologies. When this is compared with other ESS, these values are highly lower since BESS and pumped-hydro can achieve 85% RTE. Nevertheless, analysing the improvements that can be achieved in the following years for the P2P ESS, the major potentials come from improving the energy efficiency of the electrolyser and electric efficiency of the mGT along with higher integration between the application's energy demand and the power and heat delivered by the mGT. Thus, it is concluded that RTEs in the order of 40 to 42% could be achieved for the combination of P2P and mGT in the following years as an energy storage system at large scale.

A second study was conducted with the aim to assess the performance of the electrolyser and H_2 compressor. The main goal of this analysis is to look into the thermodynamic principles of each process: electrolysis of water and compression of hydrogen, with the aim to characterise the energy and exergy balance of the system, looking at their behaviour individually and when functioning together [25]. The results of this study were presented in the Conference Turbo Expo: Power for Land, Sea, and Air in June 2022.

The main conclusion that was obtained from this study is that the highest potential to increase the exergy efficiency of the electrolysis-compression system stems from using electrochemical compression until 30 bar followed by mechanical compression until the final storage pressure. In this way, exergy efficiency is improved by 1.3 percentages compared to when hydrogen is produced 1 bar from electrolysis. Accounting for exergy destruction in the electrolyser and the compression system, the electrolyser is responsible for more than 95% of the total exergy destroyed in the range from 1 to 100 bar compressor inlet pressure.

3.2. ESR3

3.2.1. Introduction

This work involves the cycle developments of mGT which were performed by ESR3 until now within the project. The research firstly focuses on the effective and fast modelling of the Turbec T100 unit in steady state and transient conditions. We aim to utilize this model and to assist the role of mGTs in the future energy production and use it as a baseline to include more complex cycle configurations. Parameters that affect the transition between loads are optimised in order to minimise the error from experimental results of this engine. The second part of studies the thermodynamic limit 2-spool mGT with Intercooling by adding water injection into the cycle. The goal of this study was to investigate the potential of water injection in the 2-spool mGT by applying an adiabatic black box method in Python language using object-oriented programming. Past simulations and experiments with steam injection on the T100 showed the potential in the microturbine cycle [37,48,50,59]. Thus, the advantages of applying water/steam injection in a 2-spool mGT are highlighted.

3.2.2. Transient and Steady-state assessment using computational effective tools

This Chapter is based on the journal articles:
Published
Gaitanis A, Laterre A, Contino F, De Paepe W. Towards real time transient mGT performance assessment: effective prediction using accurate component modelling techniques. Journal of the Global Power and Propulsion Society. 2022; 6:96-105. Doi: https://doi.org/10.33737/jgpps/150359
Published
Gaitanis, A., Contino, F., and De Paepe, W. (December 5, 2022). "Real Time MGT Performance Assessment Tool: Comprehensive Transient Behaviour Prediction with Computationally Effective Techniques." ASME. J. Eng. Gas Turbines Power. Doi https://doi.org/10.1115/1.4055785

3.2.2.1. Introduction

The energy demand for heat and power is firmly increasing through the years and single power plants are substituted by decentralized grids [26]. During the renewable energy transition mGT should perform flexibly to the fluctuating demand. Such a power production engine has to change operating points quickly and work at part load efficiently. Thus, it is important to use a reliable dynamic model that can accurately predict the behaviour of the key performance parameters of the engine in dynamic operation. The inclusion of novel components in mGT units, like saturators, fuel cells, heat exchangers, alter the dynamic characteristics of the cycle. As a result, there is an indisputable necessity of a modular and flexible software that simulates steady-state and dynamic operation for the development of cycles with novel components.

Numerous papers, that study the dynamic phenomena in mGT cycles, have been published. Traverso validated a model of the Turbec T100 mGT using the lumped volume method [27]. Di Gaeta et al. Developed a dynamic model of the same machine focusing on the behaviour of important cycle parameters with different fuel blends [28]. An approach similar to the one of Traverso was pursued by Henke et al. regarding the flow formulation with a thorough description of a recuperator component by analytically calculating the heat transfer values [29].

The above-mentioned models present different proven approaches on the transient simulation of mGTs but the link between accuracy, calculation time, and overall complexity remains to be studied in the field of small-scale power generation. Thus, we aim to collected an effective group of modelling methods in a real-time performance application of such an engine. So, in this chapter, we extensively present the development of an accurate real-time mGT simulation tool by discussing the modelling strategies and governing equations at each individual component. Measurements on the T100 test rig at VUB, Belgium allow us to calibrate and validate the model in steady-state conditions. Then the model's accuracy in transient conditions is also tested by comparing key performance values with experimental data in positive and negative power load step.

3.2.2.2 Component modelling approach

In order to decrease the complexity and increase the accuracy of the model, a grey box modelling approach is adopted. This method combines physical and data-driven models and it is typical for the effective inclusion of performance maps [30,31]. At first the modelling method of the Compressor and Turbine component is presented which involve the adaptation of their performance maps.

Compressor and Turbine components

In order to incorporate the compressor and turbine performance maps, the map data which are given from the manufacturer are fitted with a specific mathematical equation. The fitting equation for each iso-speed line of the map should have a single form that is controlled by the coefficients of the equation. Therefore, the precision of our fitting techniques relies only the deviation from the data which is created by the form of the mathematical equation. Thus, 3 fitting cases are analysed for both compressor and turbine maps and the technique that minimizes the error from the data is integrated in the dynamic model.

For the representation of pressure ratio π_c as a function of the reduced mass flow rate $\dot{m}_c$ and reduced shaft speed *N*, three fitting mathematical equations are compared to each other. The equations of the three curves are shown below.

$$\textbf{Ellipse:}\ \left|\frac{\dot{m}_c \cos\vartheta_{\pi_c} - \pi_c \sin\vartheta_{\pi_c}}{a_{\pi_c}}\right|^2 + \left|\frac{\dot{m}_c \sin\vartheta_{\pi_c} + \pi_c \cos\vartheta_{\pi_c}}{b_{\pi_c}}\right|^2 = 1 \quad (3.2)$$

$$\textbf{Superellipse:}\ \left|\frac{\dot{m}_c \cos\vartheta_{\pi_c} - \pi_c\, sin\,\vartheta_{\pi_c}}{a_{\pi_c}}\right|^n + \left|\frac{\dot{m}_c \sin\vartheta_{\pi_c} + \pi_c \cos\vartheta_{\pi_c}}{b_{\pi_c}}\right|^n = 1 \quad (3.3)$$

$$\textbf{Supershape:}\ \left|\frac{\dot{m}_c - x_{0\pi_c}}{a_{\pi_c}}\right|^{n_1} + \left|\frac{\pi_c}{b_{\pi_c}}\right|^{n_2} = 1 \quad (3.4)$$

Equation 3.2 is an ellipse curve with a center at (0,0) and axes rotation. The Superellipse is a curve with the same parameters as the Ellipse and a coefficient *n* which alters the shape and adds an extra degree of freedom. For the equation 3, a Supershape curve is used with a center at $(x_0, 0)$, 5 degrees of freedom and no axes rotation. The fitting of the compressor's maps speed lines for the three equations is demonstrated in Figure 3.5. It is observed that Ellipse and Superellipse functions are not able to simulate the steep decrease in pressure ratio (choking conditions). Thus, the Supershape is employed to test if we can fit the data points in that region with a single equation. It seems that this equation can fit all the data points but with a questionable accuracy. Therefore, we calculated the relative Root-Mean Squared

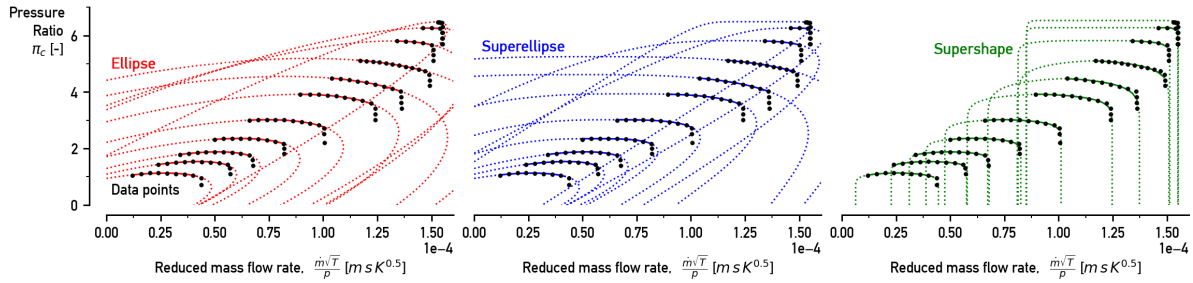

Figure 3.5 – Compressor map equations are fitted into the data points: Ellipse, Superellipse and Supershape [32]

Error (RMSE) for each case in every speed line of the data points that do not belong to the choking region and compared the different methods. Figure 3.6 shows that Ellipse has the most effective fitting behaviour in low as well as high rotational speeds with a relative error below 0.9%. Moreover, Supershape presented increased error (above 1.5%) despite the fitting of all data points. Therefore, Case 1 is chosen to model the speed lines due to its satisfactory results among the proposed fitting methods. This technique is also coupled with a linear interpolation between the points of maximum mass flow and minimum pressure ratio at the chocking region to account for the accurate representation of the steep decrease in the π_c value. Then, the parameters of the adopted equation (α, b, ϑ) are expressed as a function of rotational speed with the use of 1-D interpolation.

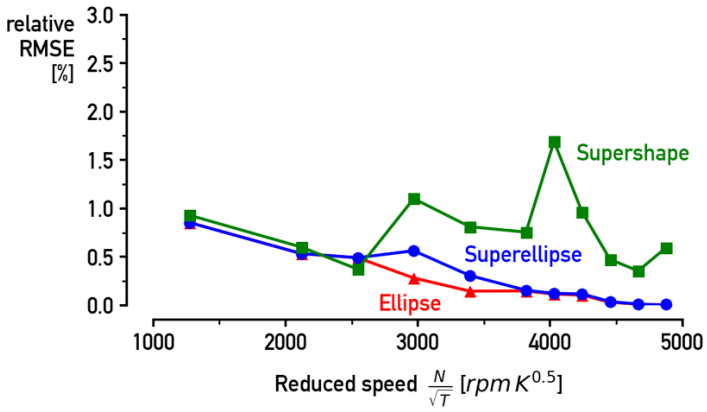

Figure 3.6 – The relative RMSE of the 3 equations as a function of the reduced speed for the compressor map. The relative RMSE of the fitting curves highlight the superiority of the first method (red lines) [32].

For the adaptation of the Turbine maps exponential and polynomial equations are used with the 5th degree polynomial to present the most accurate results. Moreover, a similar method and fitting equations were used for the calculation of the efficiency curves for both the Compressor and Turbine [32].

The outlet values are determined with the same modelling approach for both the compressor and the turbine. Therefore, the black box model for the Compressor and Turbine with the input and output variables is presented in Figure 3.7 as part of the global mGT model because outlet values are determined with the same modelling approach for both components

The mass flow rates of these blocks are calculated by the utilization of the map equations as shown in Figure 3.7 for a given shaft speed (N) and pressure ratio (π). The isentropic law is used for the determination of the outlet temperature and the outlet specific enthalpy is derived from the definition of isentropic efficiency (η_{is}) where $h_{is,out}$ is obtained from the Coolprop library [33] using the pressure and temperature of the stage as inputs. Also, in Figure 3.7 m_{casing} is the mass and specific heat capacity of the virtual casing. Which is obtained by calibrating this module with experimental results from the T100 test rig.

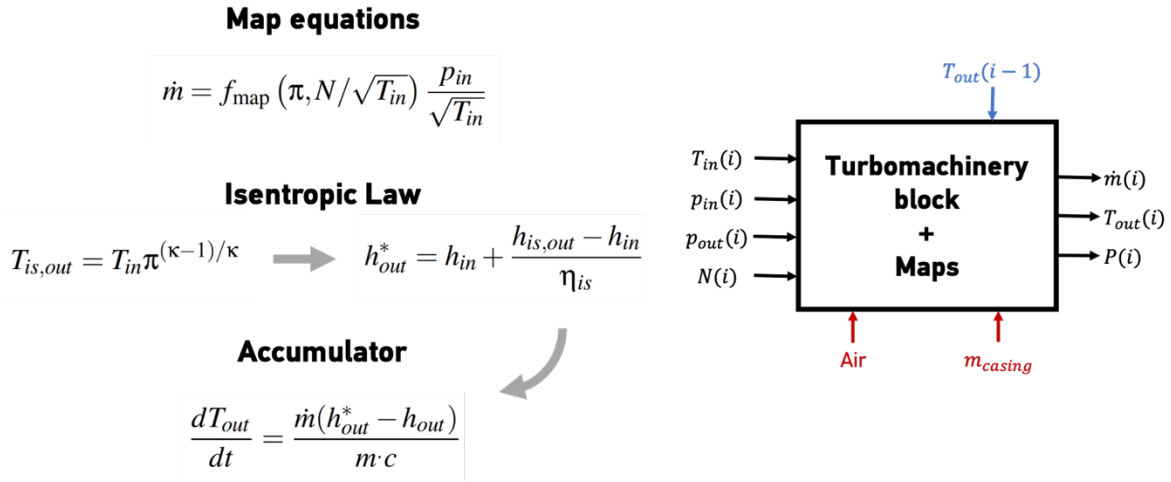

Figure 3.7 – The equations that govern the calculation of the outlet conditions of the turbomachinery block are shown in the left-hand side. The layout of the turbomachinery block with the input and output parameters is presented in the right-hand side. The constant values are presented at the bottom of the box and the values of the previous time step at the top.

Recuperator component

The heat exchanger is discretised into a N cells to ensure a satisfactory accuracy according to Figure 3.8 . where the energy equation is applied using the following formulation:

$$\frac{mc_m}{N}\frac{dT_{w,i}}{dt} = \dot{m}_c c_{p,c}(T^c_{i+1} - T^c_i) - \dot{m}_h c_{p,h}(T^h_{i+1} - T^h_i) \quad (3.5)$$

The heat capacity and the mass of the casing are expressed with c_m and m respectively. The remaining values of the equation are the temperature, mass flow rate and heat capacity of the hot, cold side and wall as shown in Figure 3.8. For the heat balance of the air and gas stream, we applied a steady-state approximation. This is justified as the temperature rate of change in each "stream" cell is greater than the temperature rate of change in each "wall" cell. So, the heats that are absorbed and released from the streams in each cell are presented below:

$$\dot{Q}_{c,i+1} = \dot{m}_c c_{p,c}(T^c_{i+1} - T^c_i) = \frac{UA_c}{N}\left[T_{w,i} - {}^1\!/_2\,(T^c_{i+1} + T^c_i)\right] \quad (3.6)$$

$$\dot{Q}_{h,i+1} = \dot{m}_h c_{p,h}(T^h_{i+1} - T^h_i) = \frac{UA_h}{N}\left[{}^1\!/_2\,(T^h_{i+1} + T^h_i) - T_{w,i}\right] \quad (3.7)$$

We also assumed that the thermal resistance of the recuperator plates is fairly small and could be ignored.

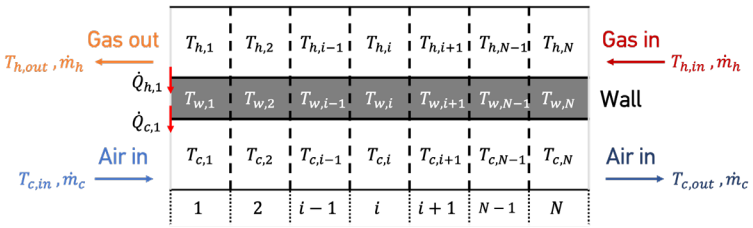

Figure 3.8 – Modelling scheme of the heat exchanger [32]

Moreover, two different cases for the heat transfer coefficient will be considered. In the first one, the UA is kept constant and is taken by the work of Lagerström at nominal conditions. In the second case, the UA is expressed as a function of $\dot{m}_c$. This function is constructed by tuning the UA in order for the component to match the effectiveness (ε) of experimental data of the T100 in 4 different operating points (100, 90, 80, 70kW). Then a linear interpolation is applied between the tuned UA points

Combustion Chamber component

The boundary conditions of the Combustion Chamber (CC) block are presented in Figure 3.9. with red colour. This module calculates the mass conservation inside the CC, which is described in Figure 3.9 along with the energy conservation. The LHV is the Lower Heat Value of the fuel, and η_{cc} represents the combustion efficiency. Also, h is the specific enthalpy of the 3 different flows and u_3 equals the specific internal energy of the flue gasses (subscript f) at the combustor outlet. The pressure

Single step combustion model

$$nC_cH_h + n_{O_2}O_2 + n_{N_2}N_2 + n_{Ar}Ar \Longrightarrow$$
$$ncCO_2 + \left(\frac{nh}{2}\right)H_2O + \left(n_{O_2} - nc - \frac{nh}{4}\right)O_2 + n_{N_2}N_2 + n_{Ar}Ar$$

Mass conversation

$$\frac{d\rho_3}{dt} = \frac{1}{V_{comb}}(\dot{m}_c + \dot{m}_f - \dot{m}_t)$$

Energy conversation

$$\frac{du_3}{dt} = \frac{1}{\rho_3 V_{comb}}\Big(\overbrace{\dot{m}_c h_{2'}}^{\dot{Q}_{air}} + \underbrace{\dot{m}_f(h_f + \eta_{comb}LHV)}_{\dot{Q}_{fuel} + \dot{Q}_{comb} - \dot{Q}_{loss}} - \overbrace{\dot{m}_t h_3}^{\dot{Q}_{gas}} - u_3(\dot{m}_c + \dot{m}_f - \dot{m}_t)\Big)$$

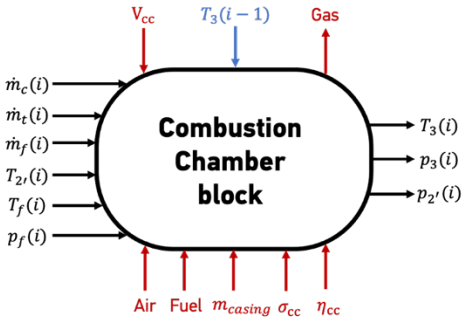

Figure 3.9 – The equations that govern the calculation of the outlet conditions of the Combustion. Chamber block are shown in the left-hand side. The layout of this block with the input and output parameters is presented in the right-hand side.

(p4) and temperature (T4) at the outlet are calculated from the Coolprop library [33] after we determine the u3 and ρ3.

Shaft component

The rotational speed of the shaft is calculated by the differential equation in Figure 3.10 which is called Global energy balance of the cycle. The shaft angular speed is ω, I is the moment inertia of the shaft, P_t is the power produced by the turbine, P_c the power required by the compressor, P_{lb} the power

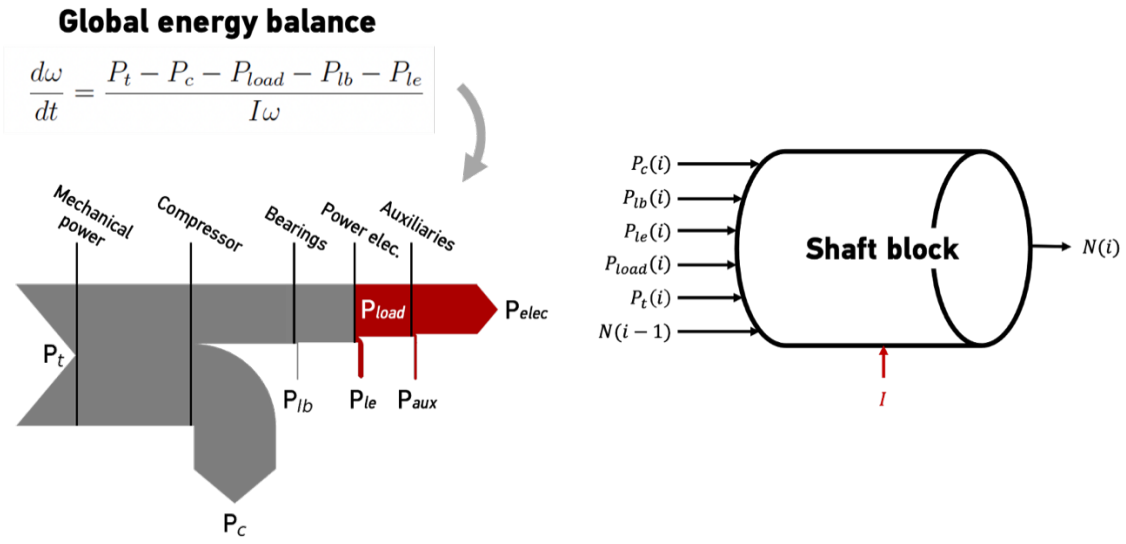

Figure 3.10 – The equation that governs the calculation of the Shaft rotational speed is shown in the left-hand side along with a visual representation of the power losses of the cycle. The layout of this block with the input and output parameters is presented in the right-hand side.

losses from the bearings, P_{le} the consumption of the power electronics and auxiliaries and P_{load} is the power produced in the generator. This value is regulated by the control system. For the bearing losses, the model presented by Henke et al. is adopted [29]. For the electrical losses and auxiliaries, a correlation is made using experimental data from the Turbec T100 test rig for the electrical losses and auxiliaries. This correlation is a function of P_{load} with a 3rd degree polynomial. The generator is modelled with an electrical efficiency of 99% and the power electronics with a conversion efficiency of 95%.

Control system

The control system the T100 engine is comprised by the fuel control and the power control presented in Figure 3.11. The fuel control consists of a Turbine Outlet Temperature (TOT) control loop which keeps the TOT constant during the transients. Based on the shaft speed, a primary value of the fuel requirement is calculated by a table from the manufacturer. Then the TOT fuel requirement is added in the primary value and added to an integrator of the TOT fuel requirement to get finally the total fuel requirement.

The input of power control is P_{dem}. The controller corelates P_{dem} with a reference shaft speed by look-up tables from the manufacturer. Then this speed is controlled by a fault signal between P_{dem} and P_{load} of the previous time step. Finally, the corrected reference speed is compared with the calculated shaft speed (N).

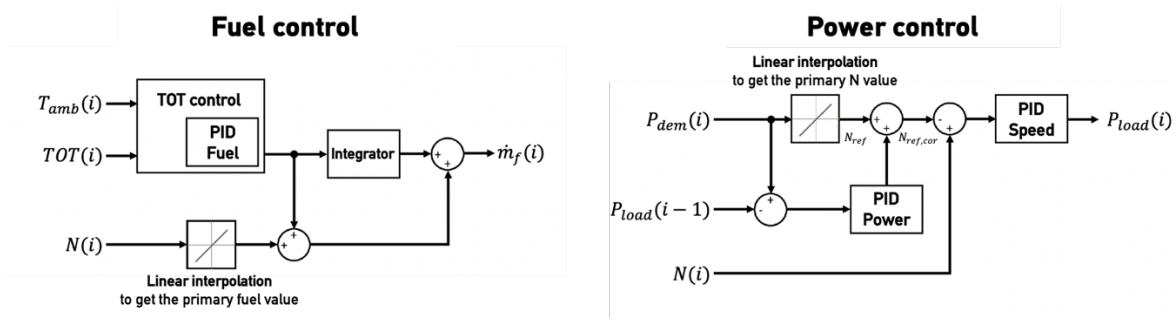

Figure 3.11 – The layout of the Fuel and Power controls which are part of the main control system of the Turbec T100.

3.2.2.3. Complete mGT dynamic model

The inclusion of each component that was demonstrated above into a complete real-time simulation software requires to solve 11 different ODEs fast. The complete model is shown in Figure 3.12. The link between different components is also evident with arrows that connect the inputs, outputs and boundary conditions. Also, the step-by-step solution at each stage of the model is depicted in the right-hand side of Figure 3.12. At first, the Combustor outlet conditions are calculated and in the next step the mass flow, temperature and pressure at the outlet of the turbomachinery components. The Recuperator outlet conditions at point 2' is the last stage that is calculated in a specific time step.

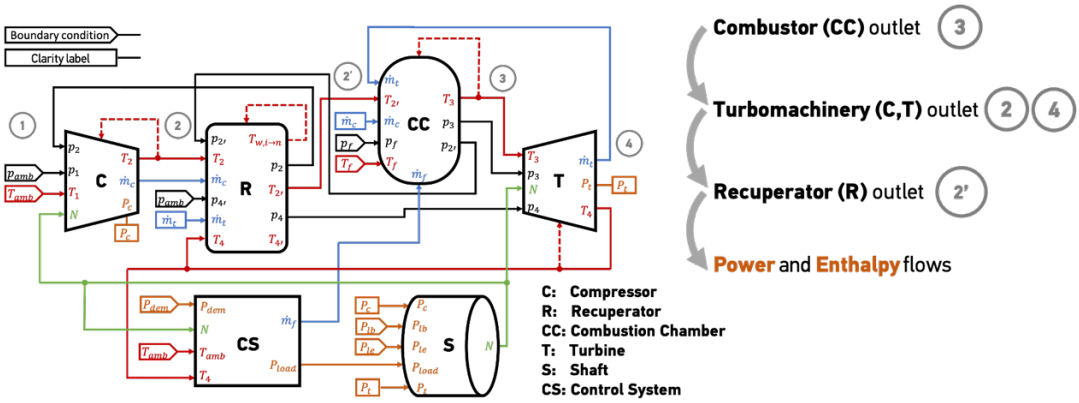

Figure 3.12 – The layout of the mGT model is presented with arrows presenting the calculated parameters and its connections with the components.

3.2.2.4. Results and Discussion

Steady state validation

In this chapter, we discuss the fidelity of the developed model regarding the measurement results that are obtained from the Turbec T100 VUB, Belgium test rig at steady state and transient conditions. Four steady-state tests are carried out with a power load (P_{load}) of 100, 90, 80 and 70 kWe. The tests were executed at an average ambient temperature (T_{amb}) of 21.2 °C. The values that are used for this validation are the Shaft speed (N), the Fuel flow rate ($\dot{m}_f$), the electrical efficiency ($\eta_{el} = (P_{load} - P_{aux})/(\dot{m}_f LHV)$), the Compressor outlet temperature (T_2), the Compressor outlet pressure (p_2), the CC inlet temperature (T_3). Figure 3.13 shows the relative error of the values that are tested during the validation in four different generated power loads. The relative error is $e = (|x_m - x|/x_m)100\%$ with the simulated values as x and the measured as x_m. The majority of the values in Figure 3.13 show errors below 1.5%. Furthermore, it is shown that fuel flow rate, efficiency and shaft speed have the largest error at 80 kWe. However, this error does not exceed the 1.5% limit which is considered to be in the range of accuracy of the measurement probes. As a result, this error is considered to be acceptable for mGT operations and the model is optimized for the Turbec T100 mGT.

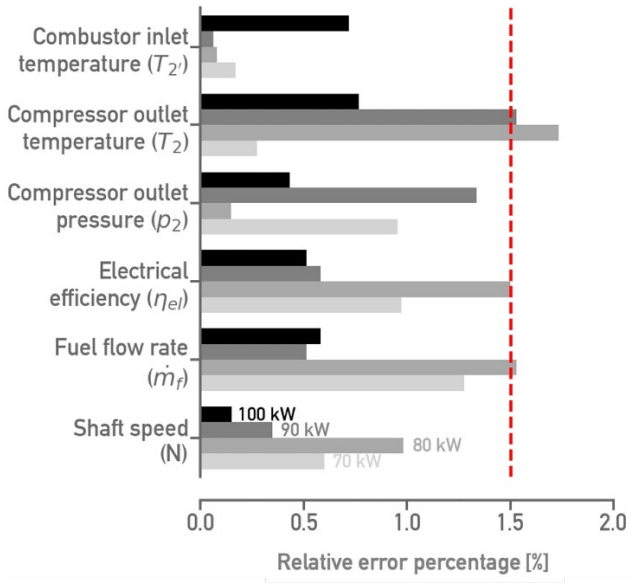

Figure 3.13 – Error percentage of the values that are used for steady state validation. The majority of the values have an error below the range of accuracy of the measuring probes [34].

Transient validation

Two-step changes are presented in the demanded power during the transient validation. The first step is 100-80 kWe (-20 kWe) and the second 90-100 kWe (+10 kWe). Firstly, the simulated slopes of the Electric power (P_{load}) correspond with the measurements nicely. This confirms that the power control of the model effectively predicts the behaviour of the actual controller of the engine [34]. The other important parameter that can verify the effective behaviour of the control system is the fuel flow rate as it regulates the energy and mass conversation of the combustion chamber and adjusts the TOT and p4. Figure 3.14 presents the fuel flow rate through time at the two demanded power steps. In both steps, the slope during the transient follows well the experimental measurements. At 90 to 100kW there is a relatively higher fuel flow rate at 45-50 sec. The fuel flow rate peak occurs at this moment during the simulation, while in the measurements the peak is after 10 sec. This mismatch in mass flows, after the transition, very quickly dissipates before the 100 sec mark. On the other hand, at 100 to 80kW the model simulates almost accurately the fuel flow transition. Thus, we can also see that the fuel control module accurately predicts the mass flow rate for a negative step change but miscalculates the peak position at the positive step. This does not prevent the control system to provide the correct amount of fuel in the cycle before and after the peak.

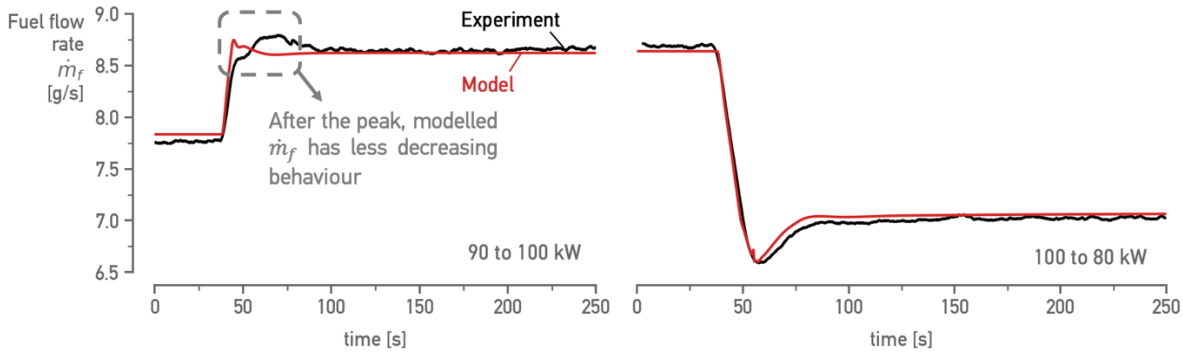

Figure 3.14 – Fuel flow rate transition from 90 to 100kW (left hand side) and 100 to 80kW (right-hand side) [34].

The rotational speed results are shown in Figure 3.15 at the same demanded power steps. The slope of the transition matches well the simulated rotational speed in both steps. At 90 to 100kW there is a decreased peak in N compared to the experiment. Furthermore, the downward peak in the negative

power step is smaller and the model overestimates the Shaft speed at 80kW. This behaviour is a result of the simplicity of the control system by the control system and a possible deviation of the compressor map from the actual turbomachinery performance characteristics of the test rig. Also, because the current test rig was converted to an mHAT, there are extra pressure and heat losses due to the additional tubing. These losses could affect the pressure ratio of the turbomachinery components and as a result slightly miscalculate the shaft speed.

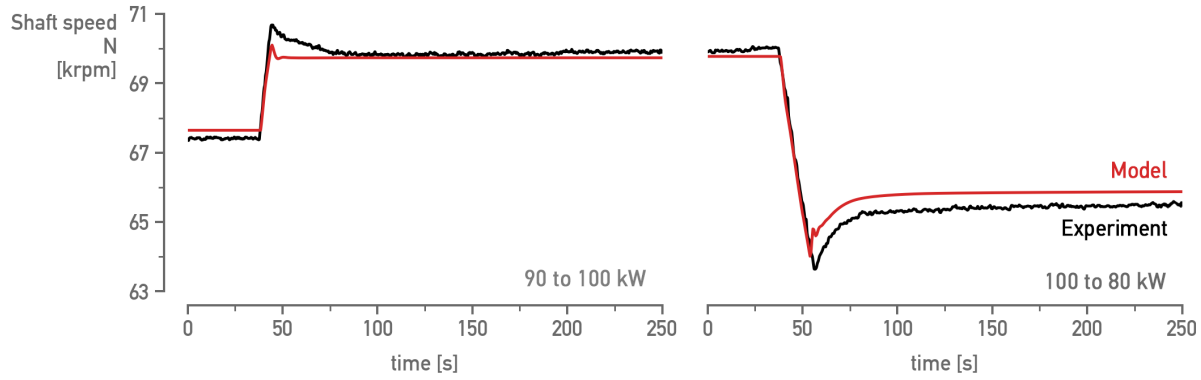

Figure 3.15 –Shaft speed (N) at positive (left-hand side) and negative (right-hand side) power step [34].

Figure 3.16 presents compressor outlet T_2 and recuperator outlet $T_{2'}$ temperatures at a -20 kW_e (100-80kW_e) demanded power step change. The error of T_2 is rather small and does not exceed 3°C due to the effective calibration of the virtual mass of the compressor casing. The recuperator cold side temperature is closely dependent on the T_2, the TOT from the energy balance in the heat exchanger and the heat transfer coefficient (UA). The TOT is controlled by the fuel flow and affects the behaviour of the $T_{2'}$ slope. Also, the UA plays a significant role as it regulates the the amount of heat that is added to the flow. Therefore, Figure 3.17 confirms that the approach to use a variable UA asis a function of airflow calculated T_3 accurately. The simulated T_3 matches well the measurements during the transition. Although, we observe a higher peak of this value compared to experiments this result is in the range of the measurement probe uncertainties.

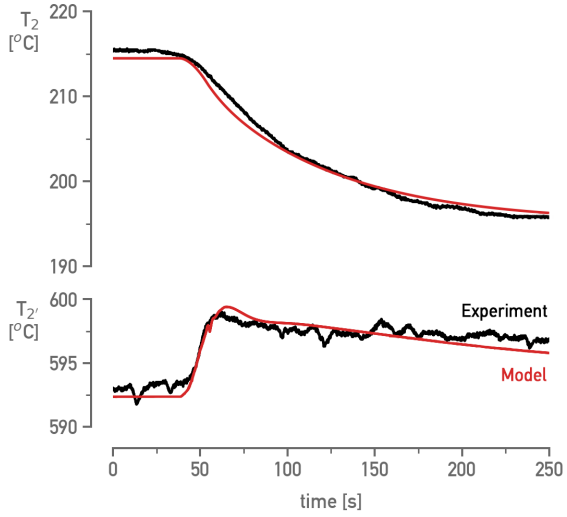

Figure 3.17 – Compressor outlet temperature (T_2) and Recuperator outlet temperature of the cold side ($T_{2'}$) at a negative power step from 100 to 80kW_e [34].

From the transient and steady state results of the developed model, it is safe to conclude that the simulation software presents a good agreement with the data with only minor deviations. The increased peak in fuel flow rate is a result of the fuel control system which needs further calibration. Also, the small error in the shaft speed is a product of pressure losses modelling in part load conditions. As a

future step, these losses could be recalculated and a correlation can be extracted based on the test rigs data.

3.2.3. Water injection in a 2-spool mGT – a black box method

3.2.3.1. Introduction

In order to enhance the profitability of mGT in a CHP operation and make it more competitive against ICE engines, the electrical efficiency of the unit should increase. Any increase in the Turbine Inlet Temperature (TIT) and recuperator effectiveness assist in the improvement of the overall performance of the engine [35]. However, the cooling techniques that increase the TIT are difficult to be applied in a radial turbine configuration. Therefore, many studies focus on the use of ceramic materials in heat exchanger that could improve dramatically the energy savings [36,37]. Although, at the current state of GT technology advancements the recuperator efficiency is benefitted by increasing the recuperator size, weight and cost [35]. This could increase the pressure drop of the component and will result in a decrease of the turbine efficiency [38]. Galanti and Massardo proposed that a 2% efficiency increase of the turbomachinery components would significantly increase the overall mGT electrical efficiency without affecting the cost [39].

In this context, water injection is proved to be an effective way to increase the performance of GTs [40]. When the heat demand is limited in a CHP unit, the thermal energy in stored in the exhaust gases could be recovered by injecting heated water inside the cycle. In that way the investment into mGT units could be profitable [41]. The beneficial effect of steam injection on the efficiency of a recuperated mGT cycle was simulated [42]. Parente et al. studied the thermo-economic performance of the micro Humid Air Turbine (mHAT) [43]. The effect of rich steam mass flow is studied in a hybrid system test rig by Ferrari et al. Test results indicated that the mGT accepted the injected steam mass flow rate without surge problems [44]. De Paepe et al. research the potential of injecting liquid water from a thermodynamic point of view. Direct injection of heated water is proved to the most optimal cycle layout for waste heat recovery through water injection in a mGT [45].

None of the previous mentioned studies however identified the most optimal route for liquid water injection in a 2-spool mGT cycle to exploit the waste heat. In this chapter, the results of water injection in a mGT, using black box are presented. The black box considered as adiabatic and no constant stack temperature is imposed. Therefore, we allowed condensation of the exhaust gasses without controlling the condensed amount of water. The main goal of this study is to determine the thermodynamic limit for water injection in a twin-spool mGT under this deliberate boundary condition.

3.2.3.2. Methodology

For this approach we modelled the 2-spool mGT which has similar performance characteristics as the Aurelia A400 mGT [46]. The simulation toll is developed in Python programming language. The layout of the engine is demonstrated in Figure 2.2. Such a mGT presents high electrical efficiency (40% in nominal conditions) and could compete against the ICEs in the small-scale CHP market. This type of engine has radial compressors and turbines with permanent magnet electric generators. The two shafts can operate at variable speeds and they are directly linked to the spool without a gearbox. Aurelia Turbines also claim that the combustor is modular and can be replaced to accommodate alternative fuel blends. The electrical efficiency is increased as both spools have active magnetic bearings to reduce friction and maintenance demands. As a result, the requirement for oil pumps is eliminated [46]. The

Table 3.4 - Design parameters of the two-shaft gas turbine [47].

Parameter	Value	
Pressure ratio, π	5	
Turbine inlet temperature, TIT	1 350	K
LP compressor isentropic efficiency	80	%
HP compressor isentropic efficiency	82	%
LP turbine isentropic efficiency	84	%
HP turbine isentropic efficiency	84	%
Recuperation degree, ε	0.90	

main design parameters of this engine (see Table 3.4) are used to develop a 0-D steady state model which is the baseline in order to introduce water injection.

The simulation approach for each component is similar with that of the previous Chapter 3.2.2. Although in the current model the use of Accumulator is avoided as the cycle is modelled only in steady state conditions. The compressor maps are extracted from literature [47] and digitized to calculate the pressure ratio and isentropic efficiency of Low Pressure and High Pressure Compressors. The outlet temperature of the turbomachinery components is calculated using the isentropic law. Also, the High Pressure Turbine is considered choked. Thus, the maximum amount of mass flow rate through the turbine is fixed by the choking constant is defined as [48]:

$$K_c = \frac{\dot{m}_{HPT}\sqrt{TIT}}{P_{in,HPT}} = A\sqrt{\frac{k_{HPT}}{R}\left(\frac{2}{k_{HPT}+1}\right)^{\frac{k_{HPT}+1}{k_{HPT}-1}}} = constant \quad (3.8)$$

where $p_{in,HPT}$ is the pressure at the inlet of the turbine, k_{HPT} corresponds to the heat capacity ratio of the turbine working fluid, R is the gas constant and A is the cross sectional area of the turbine. As we introduce water in the cycle the k_{HPT} decreases, eventually leading to a reduction of the choking constant.

Similarly, the influence of k on the isentropic efficiency of the turbine is addressed for the water injected mGT. This is done, as suggested by Parente et al. [49], with

$$\frac{\eta_{is}}{\eta_{is}^*} = \frac{k-1}{k^*-1}\sqrt{\frac{k^*+1}{k+1}\frac{1-1/PR^{(k^*-1)/k^*}}{1-1/PR^{(k-1)/k}}} \quad (3.9)$$

where the apex (*) refers to the properties of standard dry air and PR to the pressure ratio of the component.

The power ratio (P_eR) between the generated power of HP and LP is extracted form literature and has the value of 1.018 [47]. With that in mind, the complete steady state model of the cycle operating first with dry air is constructed. The flow chart of the calculations at each component is presented in Figure 3.18. The model uses an internal which starts at the inlet of the cold side of the recuperator. This iterative method assumes an inlet hot side temperature (T_8) at this step and solves the Recuperator, Combustor and Turbine blocks until the error of T_8 between iterations is minimized. The external loop has the role to converge the simulation to three user defined constant values using the Secant method Therefore, $\dot{m}_{air}$ controls K_c, N controls P_{load}, PR_{HPT} controls $P_eR = P_{HP}/P_{LP}$.

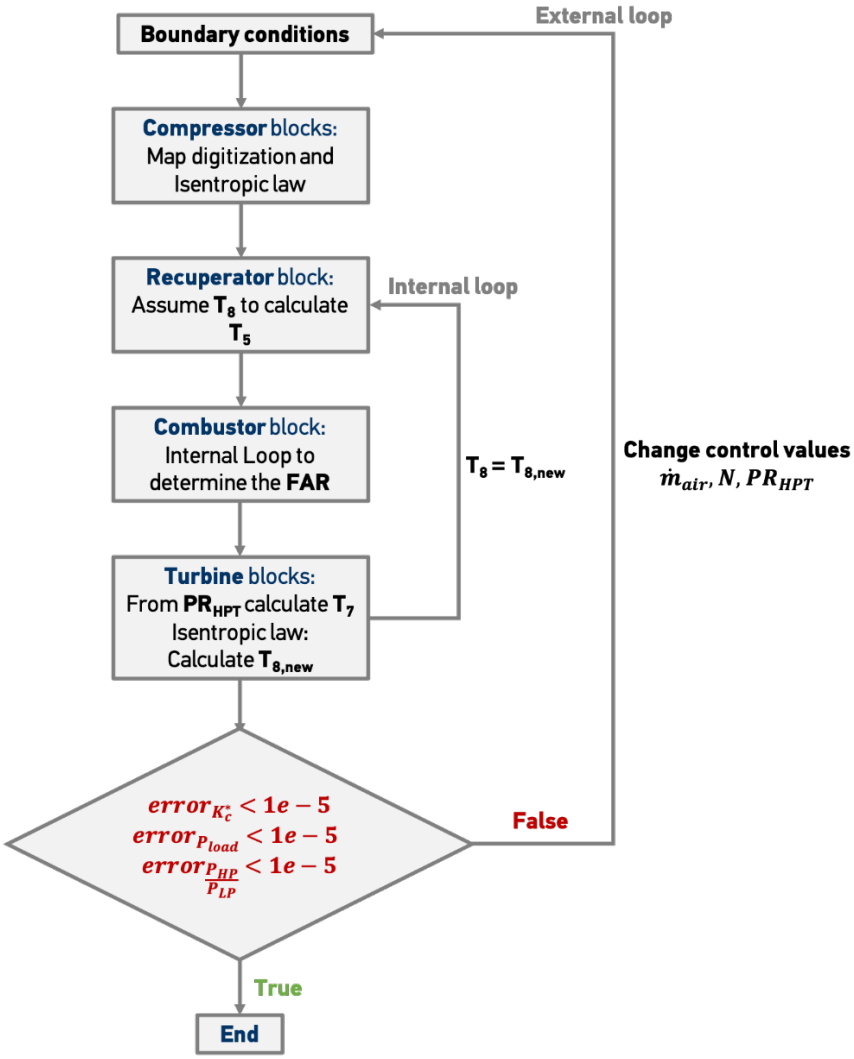

Figure 3.18 – Flow chart of the step-by-step solution in the simulation process.

When the simulation ends and the steady state point of the nominal conditions is reached (400kW), we compared the Temperature and Pressure values with the ones found in literature [50]. The error between the results and the values from the literature is calculated the same way as in Chapter 3.2.2.4. Figure 3.19 presents the different relative errors for the pressure and temperature at 6 points in the cycle. Figure 3.19 ensures that the methods used in this model are in line with the literature as the error of the key parameters is below 1%.

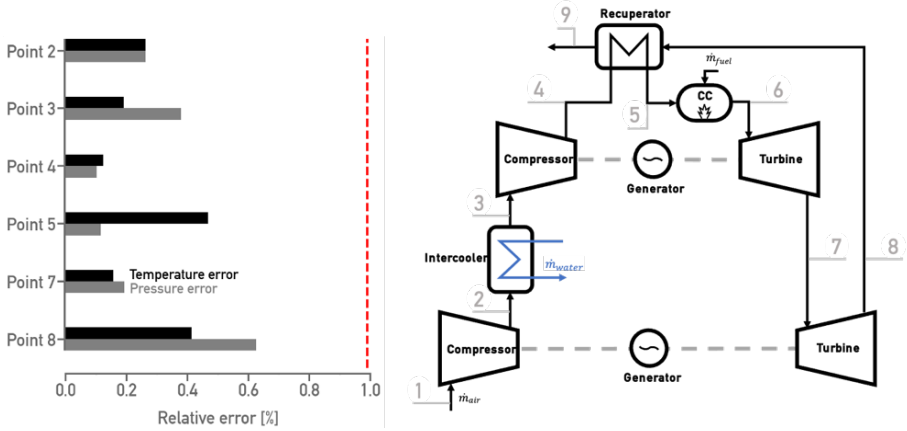

Figure 3.19 – Relative error percentage at 6 stages of the simulated cycle.

Water injection is introduced in the cycle before the inlet of recuperator cold side. The water and the other fluid properties are modelled with Coolprop Python library [33] and are considered pure fluids. An iterative method is created to calculate the possibility of two-phase water into the humid air. This iterative method is also utilised to model the condensation of the exhaust gases when they go through the recuperator. Figure 3.20 presents the 2-spool mGT cycle with water injection and the considered black box for this analysis. the water is injected in the compressed air. Before entering the combustion chamber, the air/water mixture is preheated in the Recuperator. The flue gasses coming from the turbine are then cooled in Recuperator hot side before they are ejected through the stack. Moreover, the temperature difference between the cold side outlet and hot side inlet (hot pinch ΔT_{hot}) of the black box is imposed in order to have the necessary variable to calculate the energy balance in the recuperator. This hot pinch is imposed taking into account that the recuperator has 0.9 effectiveness. As a result, the hot pinch value is set at 63.38 ºC.

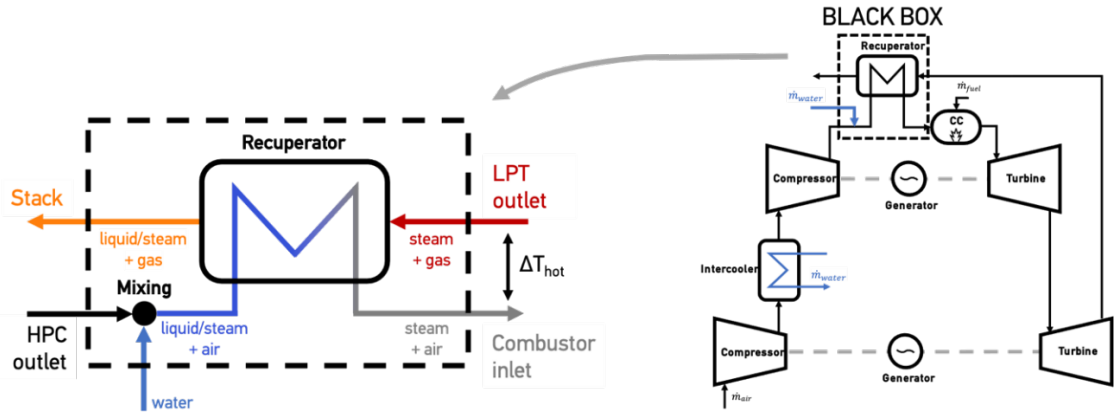

Figure 3.20 – Relative error percentage at 6 stages of the simulated cycle.

The stack temperature during simulations is variable. So, rather than applying a specific stack temperature to the black box system, it was decided to control the amount of injected water to determine the maximum amount of water. In order to calculate the thermodynamic limit of the black box the exergy destruction and exergy efficiency should be calculated. Therefore, the exergy destruction of the black box is defined as follows:

$$BB_{dest} = \frac{\sum_{in} \dot{E}_x - \sum_{out} \dot{E}_x}{\dot{E}_{x\,fuel}} \quad (3.10)$$

$\dot{E}_{x\,fuel}$ is the total exergy content of the fuel. Exergy efficiency is defined as the Exergy sum of streams that gain exergy divided by the sum of the streams that lose exergy:

$$BB_{eff} = \frac{\sum_{gain} \Delta\dot{E}_x}{\sum_{loss} \Delta\dot{E}_x} \quad (3.11)$$

With that in mind, the exergy efficiency is essentially the ratio between the exergy gain of the compressed air and the exergy loss of the flue gasses. As the condensation heat, which is exposed to the environment is considered lost and is not introduced in the exergy balance. So, for each amount of injected water we calculate the exergy destruction and efficiency. The limits for the exergy destruction and efficiency are considered a minimum of 5 % and a maximum of 93 % respectively for the heat transfer systems according to literature [51]. Crossing these limits will lead to unrealistic heat exchanger designs.

3.2.3.3. Results and discussion

For the analysis of the water injection behaviour into the cycle the electric power is kept constant at 400 kW_e and the power ratio is kept at 1.028. The injected water is varied from 0 to 320 g/s

as larger amounts of water generate solution instabilities in the iterative method of the condensation. Water and compressed air are mixed before entering the Recuperator as shown in Figure 3.20. Depending on the amount of water, the mixture of air and water is either humidified air, fully saturated air or saturated air that contains liquid water droplets.

As the injected water increases, the stack temperature (T_9) decreases linearly (Figure 3.21). More water requires more exchanged heat between the flue gasses and the wet compressed air to reach a combustor inlet temperature such that the hot pinch temperature remains constant. The stack temperature decreases until 40.95 °C. At this stage, the water in the flue gas mixture starts to condense and releases more heat.

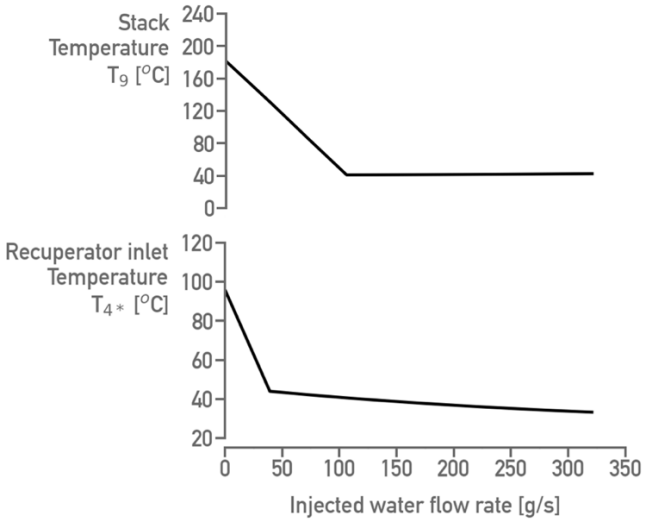

Figure 3.21 – Stack temperature (T_9) and recuperator inlet temperature (T_{4*}) behaviour with an increasing amount of water injection.

With an increasing amount of injected water, the recuperator inlet temperature (T_{4*}) follows the behaviour of stack temperature and decreases linearly until the water reaches 30 g/s. Before this point, the condensed amount of water in the air/water mixture is zero and the fluid is considered as humid air. As the injected water increases up to this point some water is condensed and the rest remains as saturated steam.

Figure 3.22 shows that for all injected water the black box exergy efficiency is below the limit that is set by the literature. Also, the Black Box Exergy destruction is higher the lower the indicated number [51]. For increasing injected water mass flow rates, the exergy destruction of the black box, increases first, while efficiency decreases. Afterwards, when flue gases condensation occurs the exergy

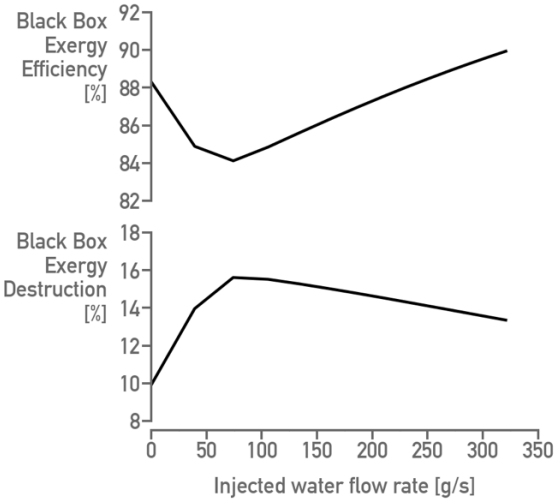

Figure 3.22 – Black box exergy efficiency and exergy destruction with an increasing amount of injected water.

efficiency starts to increase while exergy destruction decreases again. As we observe the exergy fluxes of Figure 3.23, we could thoroughly explain the behaviour of the black box exergy efficiency.

First of all, the exergy flux of the combustor inlet slightly increases after the condensation of the flue gases (Figure 3.23). As the amount of water increases the rotational speed and air mass flow rate decreases (Electric Power = constant) and compensates the increasing exergy flow due to the higher temperature and water content. The exergy flow through the LPT outlet increases, due to the higher water content of the flow. The LPT outlet temperature is also increases, as TIT is kept constant in a control loop. The HPC outlet exergy flow decreases due to the lower air flow rate and pressure ratio. The exergy flow of the injected water is not included in the figure because the water is introduced in the cycle at 15 ºC and 1 bar which is considered as the dead state of our analysis. Thus, the injected water has no exergy. Moreover, the stack exergy flow is decreasing as the stack temperature is dropping. After the condensation of the flue gases the stack exergy remains nearly constant.

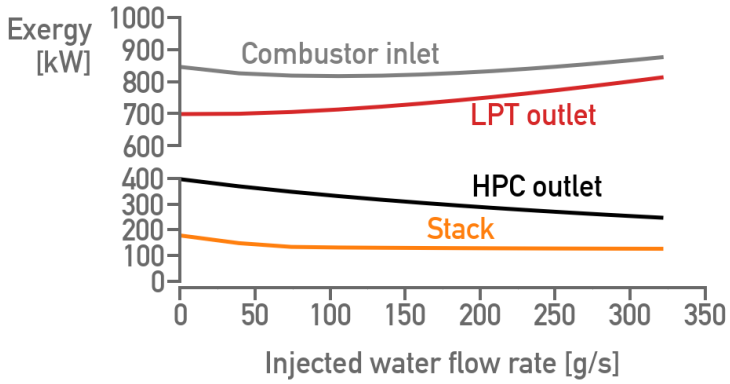

Figure 3.23 – The different exergy flows of the black box.

Therefore, the behaviour of exergy efficiency is clearer. Before the condensation of the flue gases the exergy difference between Combustor inlet and HPC outlet decreases faster than the difference between LPT outlet and stack. This phenomenon decreases the black box exergy efficiency. After the condensation of the flue gases the exergy of the HPC outlet continues to decrease and together with the slight increase of the combustor inlet exergy flow increase significantly the black box exergy efficiency.

Figure 3.22 indicates that the black box exergy efficiency could increase more if we introduce larger amount of water into the cycle. A tool to determine the limit of the injected water in order to have safe mGT operation is the surge margin which is presented in the equation 3.12:

$$SM = \left. \frac{\dot{m}_c - \dot{m}_{c,sl}}{\dot{m}_c} \right|_{N=cte} \cdot 100\% \quad (3.12)$$

$\dot{m}_c$ is the mass flow rate of the compressor and $\dot{m}_{c,sl}$ is the mass flow rate at the surge limit of the compressor at the same rotational speed.

With an increasing amount of injected water mass flow rate, the operating point of both compressors move towards the surge line (Figure 3.24). This occurs as the control system of the engine keeps a constant electric power. More heat is recuperated form the flue gases due to water injection which leads to les fuel consumption. The decrease in fuel flow rate affects the air flow rate to keep a constant TIT. As a result, the air flow rate decreases as well. The electrical efficiency, shown also in Figure 3.24, increases as the amount of injected water rises. The black box exergy efficiency behaviour (decreases and then increases) has no effect on the overall efficiency of the unit. The electrical efficiency rise depends on the amount of water mass flow rate that is introduced. At the end of the simulation with 320 g/s of injected water the electrical efficiency is 49.9 %. Therefore, the absolute efficiency rise is 10.7 %. However, this efficiency rise results in a LPC surge margin of 7.94 % and an HPC surge margin of 10.7 % which are not considered a safe operating area. In order to achieve this efficiency rise, both compressors should be redesigned in order for the surge margin to be increased up to 15-20 %. This range is considered by literature to be a sufficient margin for a safe compressor operation [52]. If the compressor designs remain the same and with the information of the lower surge

margin limit to be 15 %, it is shown it Figure 3.24 that the amount of water at 15 % of LPC surge margin is 263 g/s. With that specific amount of injected water, the electrical efficiency reaches 48.7 % which corresponds to 9.57 % absolute rise.

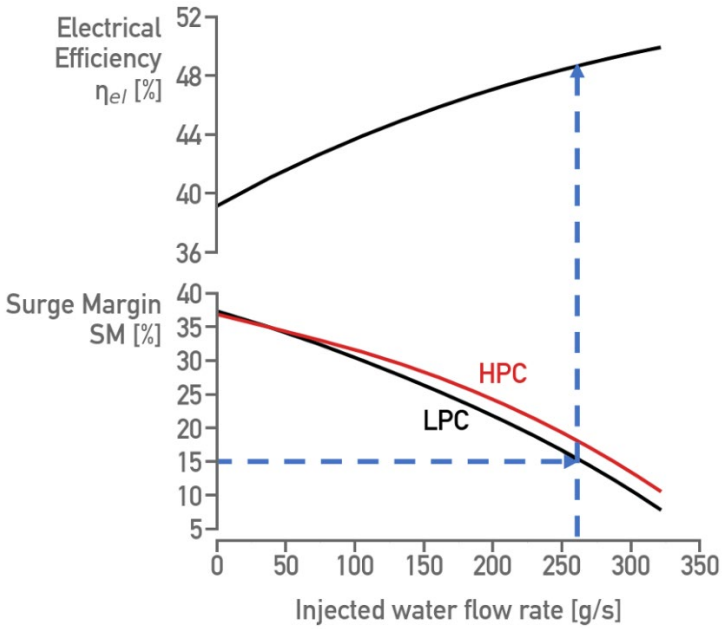

Figure 3.24 – Electrical efficiency as a function of the amount of injected water mass flow rate (upper). Surge margin of the Low Pressure and High Pressure Compressors with an increasing amount of water. SM is decreasing faster for the LPC. The electrical efficiency increases up to almost 10 % at a SM_{LPC} of 15 %.

The results of the exergy and electrical efficiency indicate that condensation of the flue gases needs to be applied with an external heat sink. This will allow the cycle to be able to absorb the heat stored in the flue gases.

3.3. ESR6

3.3.1. Introduction

The future of decentralized power production with renewables as the main driver necessitates small-scale units such as micro gas turbines (mGTs) that are reliable and flexible in operation. Similar to large-scale gas turbines, mGTs operate based on the Brayton cycle, while providing added flexibility by variable rotational speed. To continuously monitor the condition of mGTs and maintain a reliable operation, an accurate model of the engine is required which predicts the expected operation of the engine in its healthy status.

Here an accurate model for individual mGT that is fast and accurate enough to be utilized for condition monitoring purposes is presented. Due to the role of mGTs in the power generation system as backup for renewables, they operate frequently in part-load conditions to provide the remaining required power for the electric grid. Therefore, the model should provide accurate predictions for both design and off-design operations. The development of an engine model and the extensive adaptation process are presented during which the characteristics of the gas turbine components are optimized in order to meet the experimental data within a range of operational conditions. The adaptive approach is validated by the experimental results extracted from a test rig of a mGT unit such that the model can be subsequently used as a reliable tool for condition monitoring of that mGT.

To guarantee the availability of power generation units such as micro gas turbines, a condition monitoring (CM) system for assessing the operational health of the engine is required [53]. Manufacturers are adopting CM approach to optimize maintenance intervals and avoid unwanted shutdowns. A CM system monitors the performance of the engine by collecting the sensors' data and assessing the health status of the components. The core element in a model-based CM system is a model of the so-called "healthy engine" that can predict the expected behavior of the unit in which none of the components had endured any deterioration [54]. After the model is prepared, it will be implemented in the condition monitoring platform and deviations between model predictions and sensors' data from the unit will be investigated to assess the health status of the engine. In this procedure, the healthy-engine model should be able to operate with the same inputs as the real engine and provide the same information that is available through the sensors.

Two main approaches are available to provide predictions for the healthy engine: physics-based and data-based. In the physics-based approach, the engine is presented by component models connected to each other by applying the law of thermodynamics. Each component is modeled based on the characteristics of the components extracted from experiments (such as component maps) together with thermodynamic laws. In a data-based approach, the model is constructed exclusively based on operational data extracted from the engine. In this approach, artificial intelligence methods will be used to construct and train the model, based on the data collected from the healthy engine.

Both physics-based and data-based models have their merits and shortcomings: the physics-based models are usually more complicated to construct as it is elaborated with models of each individual component. The components require characteristic curves or correlations that represent the behavior of the flow passing through them. Whereas with the data-based model, no information about the components' behavior is required since the model is constructed based on the black-box assumption of the whole system. The efforts to build a physics-based model are rewarded by providing insights into engine's behavior by providing flow properties at each component's inlet/outlet. Moreover, since predictions from the model are physics-informed, they can provide acceptable predictions for a range of operational conditions, while the data-based model fails to provide good predictions for the operational range that was not included in the training dataset.

Even with a detailed physics-based model, it is common to see deviations in model predictions from real-life engine data. The main reason is imperfect component models due to mismatches between employed maps and correlations, and the actual behavior of the components. To overcome this issue, the components' model should be tuned or "adapt" to real-life components data.

In this project, an accurate physics-based model of a micro gas turbine is developed in which empirical correlations are employed together with thermodynamic equations to provide the components' model. Proper adaptation parameters are implemented inside the component's correlations and adaptation is performed to find the best set of parameters to increase the accuracy of the model in a range of operations.

3.3.2. Developed Model

The developed model for the mGT system is a computer code written in Python language and is constructed based on connecting models for each of the principal components of the engine. Each of the components are represented by the lumped assumption in which the flow condition at inlet and outlet are considered uniform. Required inputs for the solver are: demanded power and ambient conditions, namely: ambient pressure, ambient temperature and relative humidity.

Values for fuel flow rate and rotational speed is initially guessed by the solver, as well as air mass flow rate at inlet to the engine. Then the simulation is started by entering the first component with fully determined flow condition at inlet: pressure and temperature from defined ambient condition and the guessed mass flowrate. The outlet condition is calculated based on the thermodynamic equations and behavioral correlations/maps of the component and is passed as input to the next component. After a complete course of calculation is performed from the first component to the last one, the outlet pressure is compared to ambient value. According to the error in outlet pressure, the guessed air mass flowrate is modified until convergence in pressure is achieved. This is the innermost loop of the code. Two other loops are present in the code in which fuel flowrate and rotational speed are the modifying parameter and output power and turbine outlet temperature (TOT) is the controlling parameters respectively. At each modification step of these loops, the Secant method has been implemented which assures fast convergence. The algorithm behind the computer model is presented in Figure 3.25.

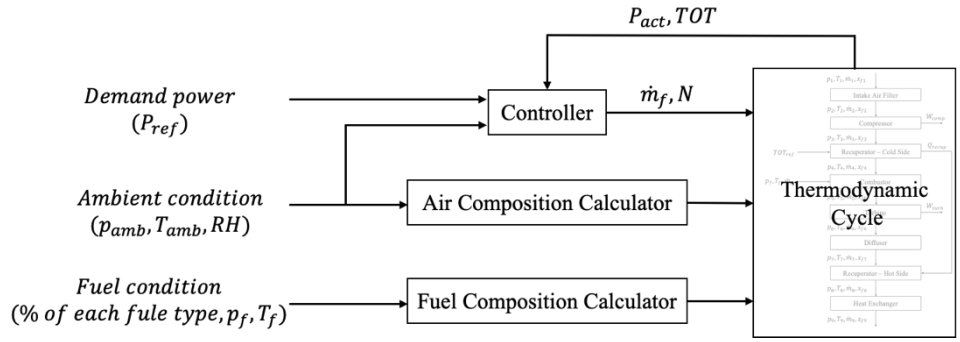

Figure 3.25 – Structure of the developed model, showing the data flow between 4 principal modules

The component models are defined as functions, in which flow properties at component inlets are input arguments, and the output arguments are outlet flow conditions. Inside each component, principal thermodynamic equations are solved with steady-state assumption, together with the behavior correlations. These correlations are often dependent on flow properties (e.g., heat capacity) which are functions of molecular composition as well as thermodynamic pressure and temperature. To accurately evaluate flow properties, the composition of the working fluid is evaluated inside each component.

The composition of the working fluid is humid air before the combustion chamber. By defining relative humidity, the actual composition of air is calculated based on the dry air composition and the ambient pressure. Detailed calculation and formulas can be found in [55]. Downstream of the combustor, the working fluid is a mixture of combustion products and excess air. The molecular composition depends on the fuel type (composition), air composition, and air/fuel ratio. The air/fuel ratio depends on the operational point, which imposes different inlet air flow rate and different fuel flow rates. Therefore, the concentration of the fuel is defined (Eq. 3.13) and calculated for each simulation point:

$$x_f = \dot{m}_f / \dot{m} \tag{3.13}$$

In above equation, is total mass flow rate. Knowing the air composition and the fuel concentration in the working fluid, the weight fraction of each element is calculated.

$$\vec{C}_w f = \left(x_{(O_2)}, x_{(N_2)}, x_A r, x_{(SO_2)}, x_{(CO_2)}, x_{(H_2O)}, x_H e\right) \tag{3.14}$$

The flow properties in each component are calculated based on the pressure and temperature of the flow:

$$k = k(\vec{C}_w f, T_s), c_p = c_p(\vec{C}_w f, T_s), c_v = c_p - R \tag{3.15}$$

$$M_w f = M_w f(\vec{C}_w f), R = R(M_w f), p_s = \rho R T_s \tag{3.16}$$

The thermodynamic equations inside components are well-known mass, momentum and energy conservation which is common among all components. However, characteristic curves (maps) and correlations are specific to each component which requires adaptation to each specific engine. The adaptation procedure is in fact calibration of these characteristic curves and correlations to better match with experimental data.

Most of the components are modeled by correlations, however, for the compressor and turbine, the behavioral maps have been implemented which are provided through tabular data. At first, it seems that conducting linear interpolation or extrapolation for the points that are not included in the tables can be a good approximate. However, try and errors has shown smooth fit to the tabular data can provide better predictions. To this end, machine learning tools have been employed to provide a smooth interpolation and extrapolation of the map data.

Here, a smooth map for turbine and compressor is provided utilizing artificial neural networks (ANN), which provides a smooth surface as the points accurately lay on them (Figure 3.26).

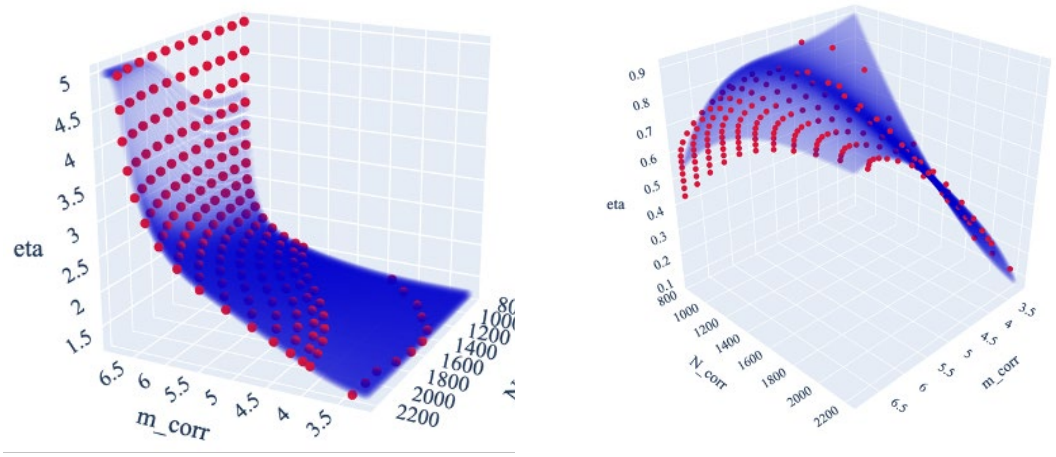

Figure 3.26 – turbine map. Blue is the fitted model and red is the map data

Developing a data-based model begins with choosing a proper machine learning algorithm that is flexible enough to imitate a non-linear behavior that comes from a system. Among various methods, artificial neural networks (ANN) have proven to be a powerful tool for modeling gas turbine systems. ANN is comprised of connected layers of nodes called artificial neurons. The most common structure of neural networks is layers of fully connected neurons, in which each neuron of a layer is connected to all of the neurons of the previous layer. Every connection line is an indicator of value transmitted while multiplied by a weight. Inside an artificial neuron, all weighted inputs are summarized and passed as input to a function called the activation function. The output of the neuron is the output of the activation function, which can be a linear or nonlinear form. In Figure 3.27 (a), the structure of an artificial neuron is depicted. The inputs () are from the upstream neurons (located at the upstream layer). Other than the inputs from the upstream layer, a bias term is added to the summation of inputs, which has been shown to improve the performance of ANNs. The Bias term has a value of unity and is also multiplied by a weight.

By placing a number of neurons with the same inputs and the same activation functions, a layer of fully connected neurons is shaped. To construct the simplest artificial neural network or a single-layer perceptron, a layer of artificial neurons is connected to a layer called the input layer. The input layer is simply a row of nodes, each accepting only one input (unlike an artificial neuron) and passing the value without any changes. The outcome of the input layer goes into the fully connected layers of neurons which provide the output of the whole network. If layer(s) of neurons are placed in between the input and output layer, then a multilayer perceptron is shaped with a number of hidden layers. As an example, Figure 3.27 (b) shows a multilayer perceptron with two hidden layers. There are 8 neurons in the first hidden layer and 6 in the second. The network has 4 inputs and 2 outputs which imposes the number of the neurons in the input and output layers.

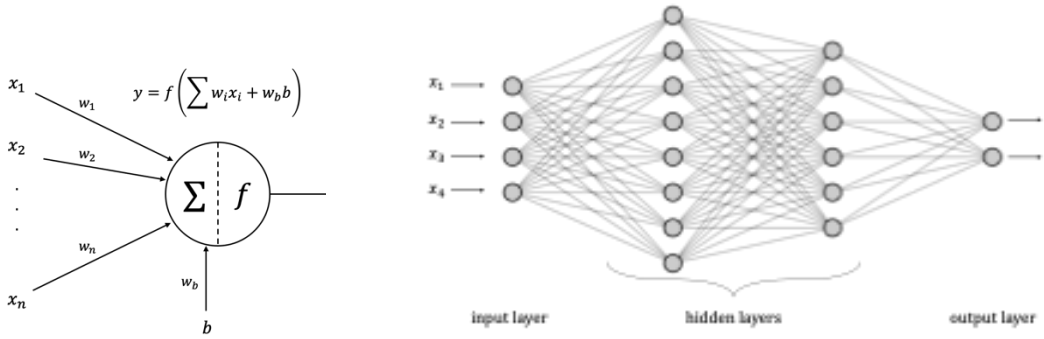

(a) (b)

Figure 3.27 – Structure of (a) an artificial neuron and (b) a multilayer perceptron

The engine modelled in this work is AE-T100 which is a recuperated micro gas turbine manufactured by Ansaldo Energia. At design point, the engine produces 100 kW power with 30% electrical efficiency while running at 70,000 rpm. The cycle pressure ratio at this point is about 4.5 and the turbine inlet temperature is around 950°C. The engine is designed to operate with turbine outlet temperature not higher than 645°C. T100 PH version of this model is equipped with a bottoming heat exchanger which increases the total efficiency (fuel utilization factor) of the unit to 80%. More detailed information about this engine can be found in (Technical Description Microturbine Turbec T100).

A schematic figure of the engine with the main components are presented in Figure 3.28. The flow at different location of the engine is distinguished by a number, which will be used inside correlations and maps. The correlations are empirically extracted from several studies conducted on the same engine and presented as functions of flow properties. Inside the correlations, the tuning parameters are implemented.

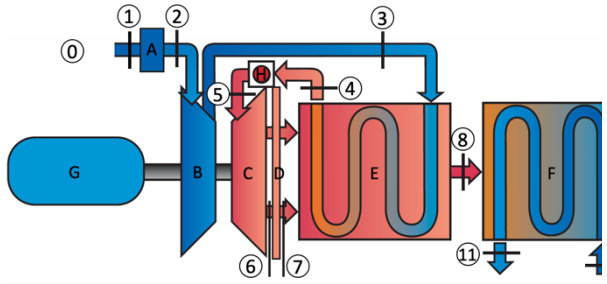

A	Intake filter
B	Compressor
C	Turbine
D	Diffuser
E	Recuperator
F	Heat Exchanger
G	Generator
H	Combustor

Figure 3.28 – Schematic of the components in AE-T100 (PH) micro gas turbine

3.3.3. Methodology of Optimization

While the developed model presented in previous section is capable of predicting engine behavior, the accuracy of each prediction point is dependent on how the characteristic curves and correlations match the behavior of the components in an actual engine. In most cases, the performance of the real engine shows deviation from those predefined characteristics which can be due to one or several of the reasons listed below:

1. Most of the characteristic maps and correlations are extracted from tests of isolated components. These results can be different from the integrated engine. One reason for such deviation is that even a sophisticated test stand fails to provide exact flow property distribution that occur in a real engine.
2. In some cases, the maps are generated by computer for the points where there is insufficient

experimental data available. For such points, interpolation and extrapolations are employed which can be different from actual experimental results.

3. Some physical properties that are involved in the maps might be difficult to measure (e.g., high temperatures), in which calculation will be used to fill the gap and therefore causing calculation error.
4. The accuracy of measurements during the component tests can affect the accuracy of the generated map, which can lead to deviations.
5. If the characteristic maps are generated from measurements in an engine, some deviations can be observed compared to other engines, due to manufacturing tolerances.
6. Even if the maps were accurate at certain time, aging of the engine and several thousand hours of operation can cause small deformations which created deviation of performance from previously accurate map.

To utilize the model in the condition monitoring platform, it is necessary to optimize it with the experimental data from the healthy engine, to avoid misclassification of aforementioned deviations as engine faults. The calibration of component characteristics with actual engine data is called model adaptation.

Model adaptation can also be helpful in cases that actual maps of the components (even imperfect version) are not available since they are considered proprietary to the manufacturer. In those cases, maps from similar components can be implemented in the model and then modified by proper adaptation procedure.

The process of adaptation starts with defining adequate adaptation coefficients in characteristics of different components. These coefficients must be able to calibrate the component behavior while retaining the overall behavioral pattern. The adaptation parameters will be modified so that the prediction of the integrated model reach closer to the experimental data from the actual engine. Therefore, the whole process can be defined as an optimization problem:

$$X_{opt} = argmin\left(\sum_{i=1}^{m}\frac{\alpha_i}{\Delta Y_{i,ref} n}\sum_{j=1}^{n}\left|Y_{exp,j} - Y_{model,j}(X)\right|\right) \quad (3.17)$$

In the equation 30 above, represents the set of adaptation parameters and includes the target properties to assess the adaptation of the model to experimental data. By definition of objective function as summation of errors on different target parameters, multiple objectives of the optimization (i.e., the multiple targets), are reduced to a single value. Mean absolute error (MAE) for each of target parameter extracted from the model and from different operation points are then normalized with a reference error value. By implementing weights for each target parameter, the importance of each target parameter is defined. The optimum set of adaptation parameters will minimize this objective function.

3.3.4. Results and Discussion

To examine the presented methodology, adaptation of the developed model to experimental data available from a test rig of AE-T100 is performed. The test rig is at Paul Scherrer Institute (PSI), Switzerland, which is installed and equipped with additional sensors for research purposes. The engine with principal flow-based components is presented in Figure 3.29.

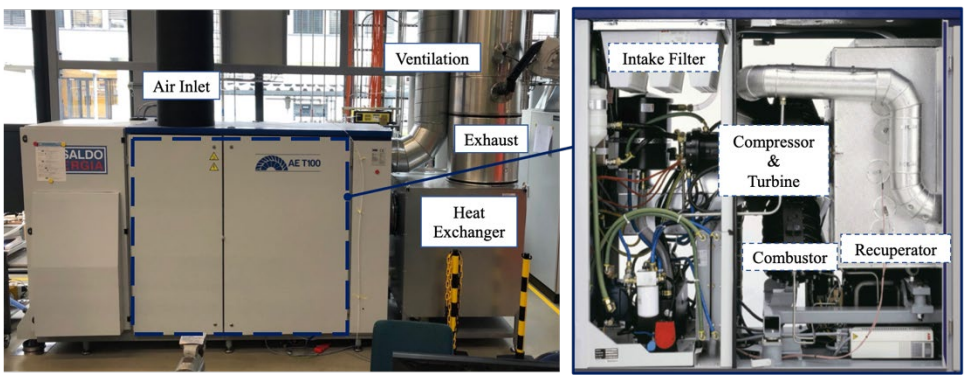

Figure 3.29 – AT-T100 at PSI with components from outside (left), engine inside with components (right). The right picture is from (ANSALDO ENERGIA)

Table 3.5 Flow-path measurements in the MGT

Location	Description	Built-in Measurements	Additional Measurements
1	Engine inlet		
2	After inlet air filter		
3	After compressor	-	
4	After recuperator cold side	-	
7	After diffuser		-
9	Engine outlet		-
10	Before heat exchanger cold side		-
11	After heat exchanger cold side		-

Other than main flow-path measurements provided in Table 3.5, cycle measurements are available from built-in sensor, such as shaft rotational speed, produced power and fuel flow rate.

The data log from the engine includes a complete envelop of operation, from start-up to load changes and to shut down and hot restarts. Since the model of the engine is developed based on steady-state assumptions, only steady state data points from the experiments were extracted to be employed in model adaptation process. From all logs of sensors collected from running the engine over 24 days, about 10,800 operation points were proved to be steady state. Since running the model for all these points takes long time, a smaller subset was chosen randomly, which is representative for the whole dataset. The 100 data points chosen for adaptation purpose is well distributed in terms of power range and ambient conditions. The distribution for ambient condition is shown in Figure 3.30. The produced electrical power by engine is distributed between 70 kW to 110 kW. Note that over 100 kW electrical power production albeit in the data, the manufacturer does not recommend operating the engine with that power rate.

The adaptation is performed in two separate steps to avoid conducting high dimensional optimizations with high calculation costs. Since the models for recuperators cold side and hot side are convoluted with each other, the only possible separating point is the outlet of the compressor. Intake and compressor are adapted in the first step (5 parameters) and the remaining 12 parameters are adapted in the second step.

For each adaptation parameter, proper bound is defined by verifying feasibility of the results from the model at max and min values. The first step is conducted with objective function, based on pressure and temperature after intake and compressor. For the second step, the temperature of air after cold side of the recuperator, the turbine outlet temperature and the net power output is chosen as target parameters for the adaptation. All errors are optimized with a normalized value and the weight factors. The weights are chosen based on the importance of each objective parameter and also through a try and error procedure, searching for the best weight set that guides the optimization to reduce the errors for each objective parameter down to their accepted tolerance. Since the data from experiment are noisy, even after noise cancelation, mean absolute error is chosen so that the objective function will be less affected by the presence of noise. The units used in equations below are kW for power, Celsius for temperatures and bar for pressure (absolute values). The optimization problem is solved with genetic algorithm embedded in SciPy library [56].

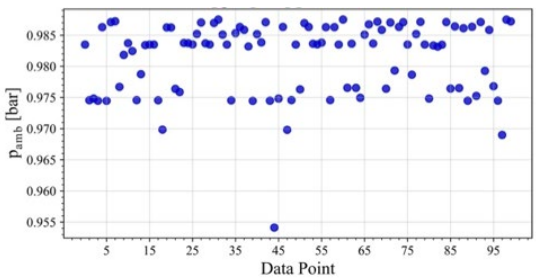

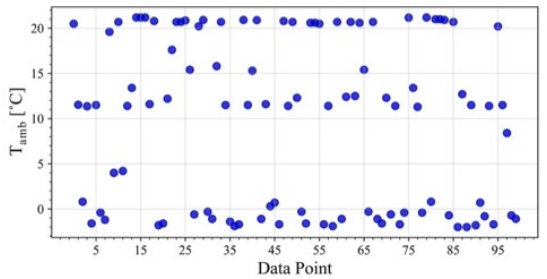

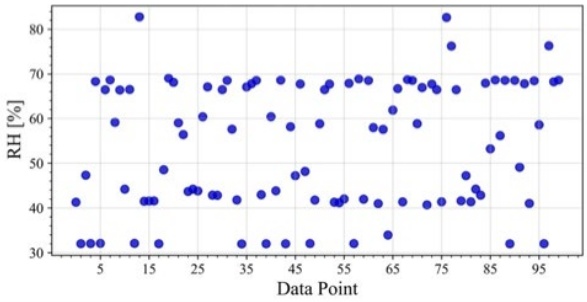

Figure 3.30 – Distribution of ambient pressure, ambient temperature and relative humidity in dataset used for adaptation

To start the optimization process, initial population was chosen randomly, with 3 times the number of adaptation parameters. Mutation is imposed during the optimization to avoid convergence to local minimum. The evolution of objective function for the second step is shown in Figure 3.31 as an example. During each optimization step, uneven number of model runs have been conducted. For instance, at first optimization iteration, the simulation ran for 72 times over 100 data points, which means 7200 times of calling and running the model. Average time for model run is 0.3 seconds which resulted 36 minutes for the first iteration of optimization, however the number of model runs is decreased as the optimization proceeds. Duration of whole process was 8 hours and 27 minutes. For the first adaptation step only 7 iterations of optimization were conducted which took less than 3 hours, as there was only 5 parameters to optimize. In total, the model with 17 adaptation parameters was adapted with less than 11 hours of run.

The bounds specified for each of the adaptation parameters with their final adapted values are presented in Table 3.6. Since the final optimized values lie between the maximum and minimum bounds, adequacy of specification of the bounds is reassured.

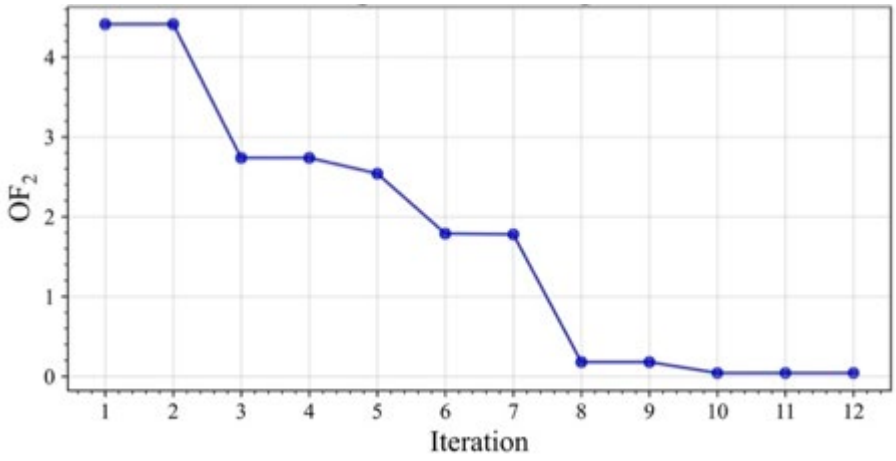

Figure 3.31 – Objective function during adaptation step 2.

Table 3.6 - Adaptation parameters with bounds, associated objective function and optimum values

No.	Parameter	Bound	Adapted value	Objective Function	No.	Parameter	Bound	Adapted value	Objective Function
1	$\Delta p^*_{coeff,intk}$	(0.50, 2.00)	1.735	OF_1	10	$\eta^*_{coeff1,rcp}$	(0.80, 1.20)	0.864	OF_2
2	$\Delta T^*_{coeff,intk}$	(0.50, 2.00)	1.051	OF_1	11	$\eta^*_{coeff2,rcp}$	(0.80, 1.20)	0.900	OF_2
3	$\Delta T^*_{incpt,intk}$	(0.50, 2.00)	1.503	OF_1	12	$Q^*_{loss,rcp}$	(0.05, 5.00)	2.612	OF_2
4	$\dot{m}^*_{coeff,cmp}$	(0.50, 2.00)	1.001	OF_1	13	$\Delta p^*_{coeff,rcp,cs}$	(0.50, 3.00)	2.901	OF_2
5	$\eta^*_{coeff,cmp}$	(0.50, 2.00)	0.977	OF_1	14	$\Delta p^*_{coeff,rcp,hs}$	(1.00, 3.00)	2.719	OF_2
6	$\dot{m}^*_{coeff,trb}$	(0.70, 1.20)	1.007	OF_2	15	$\Delta p^*_{coeff,cmb}$	(0.08, 1.70)	1.029	OF_2
7	$\eta^*_{coeff,trb}$	(0.70, 1.20)	1.046	OF_2	16	$Q^*_{loss,cmb}$	(0.10, 5.00)	2.769	OF_2
8	$\dot{m}^*_{opt,rcp}$	(0.80, 1.10)	1.04	OF_2	17	$P^*_{incpt,cnvr}$	(0.10, 2.00)	0.796	OF_2
9	$\eta^*_{opt,rcp}$	(0.80, 1.05)	1.030	OF_2					

To evaluate the performance of the adapted model, another set of 100 points were chosen from the steady state dataset, again assuring that it covers a good range of power and ambient condition by choosing randomly. An overview of model prediction errors (both MAE and maximum) for target parameters before and after adaptation is presented in Table 3.7. By looking at the error values associated with the adapted column, the maximum prediction error of power is less than 2 kW which is fairly accurate for an engine with 100 kW baseload power and minimum of 50 kW at part-load operation. Less than 5˚C of maximum error is achieved for TOT, however the maximum error for T_4 is close to 10˚C. The reason behind this is the implemented correlation for heat transfer in the recuperator.

Table 3.7 - Model prediction error for target parameters before and after adaptation

No.	Parameter	Original Model		Adapted Model	
		MAE	Absolute of Maximum Error	MAE	Absolute of Maximum Error
1	p_2	0.0025 bar	0.0027 bar	0.0010 bar	0.0012 bar
2	T_2	275.99 ˚C	330.83˚C	0.16 ˚C	0.64 ˚C
3	p_3	0.0634 bar	0.1534 bar	0.043 bar	0.069 bar
4	T_3	1.74 ˚C	5.20 ˚C	0.27 ˚C	0.86 ˚C
5	T_4	269.69˚C	323.07 ˚C	3.54 ˚C	9.74 ˚C
6	TOT	275.99 ˚C	330.83˚C	1.79 ˚C	4.94 ˚C
7	P	30.60 kW	41.80 kW	0.66 kW	1.67 kW

Figure 3.32 presents an overview of adaptation results, for target parameters of the second step of adaptation, namely power, temperature at outlet of the cold side of the recuperator and the turbine outlet temperature. As it is obvious from the left side figures, the model prediction was far from experimental data at the beginning. The adapted model predictions are depicted on the right side of Figure 3.32 which show a satisfactory compliance with experimental data. The results from before adaptation has high errors, mainly due to correlations for the components were extracted from different works and references, which were derived from using data collected from different engines. However, the configuration of the correlations was proper and compliant with the component behavior since by tuning the coefficients, a high accuracy of prediction is achieved.

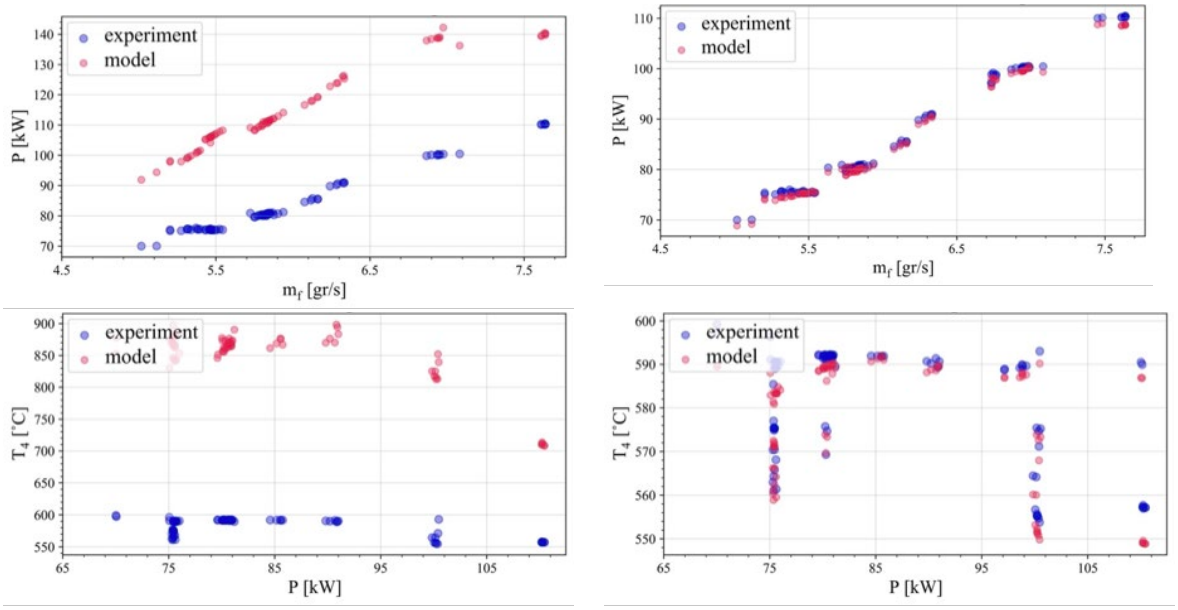

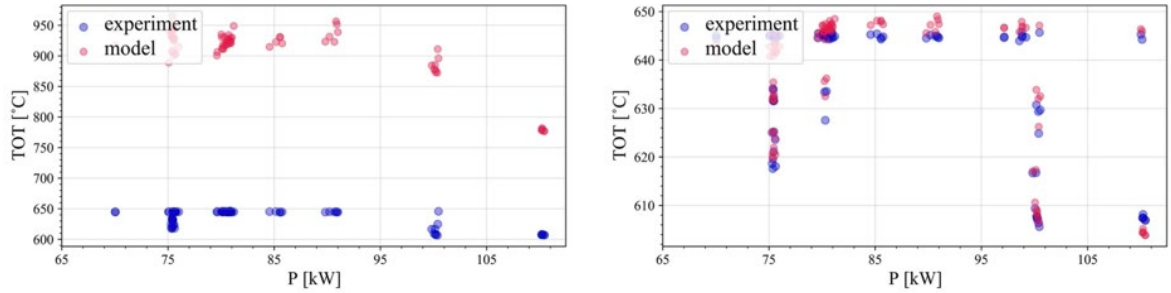

Figure 3.32 – Model prediction and experimental data for power, TOT and T_4. Left figures are from the model before adaptation and right figures are from the adapted model.

References – Chapter 3

[1] FCHEA, "Road Map to a US Hydrogen Economy," 2020.

[2] Fuel Cells and Hydrogen 2 Joint Undertaking, "Hydrogen Roadmap Europe: A sustainable Pathway for the European Energy Transition," Luxembourg, 2019.

[3] Hydrogen and Fuel Cell Strategy Council, "The Strategic Road Map for Hydrogen and Fuel Cells," 2019.

[4] Ministry of Energy, Government of Chile, "National Green Hydrogen Strategy," Santiago, 2020.

[5] C. P. a. D. M. a. P. O. a. S. C. a. A. P. M, "Substantial contribution to climate change mitigation a framework to define technical screening criteria for the EU taxonomy," Publications Office of the European Union, Luxembourg, 2021.

[6] National Renewable Energy Laboratory. Golden, CO, *System Advisor Model Version 2020.11.29 (SAM 2020.11.29).*

[7] National Renewable Energy Laboratory. Golden, CO, *PySAM Version 2.2.0.*.

[8] A. Godula-Jopek, "Fundamentals of Water Electrolysis," in *Hydrogen Production: by electrolysis*, 2015, p. 34.

[9] S. G. a. V. F. a. D. B. a. P. Millet, "Current status, research trends, and challenges in water electrolysis science and technology," *International Journal of Hydrogen Energy,* vol. 45, no. 49, pp. 26036-26058, 2020.

[10] D. S. L. G.-R. Antonio Escamilla, "Assessment of power-to-power renewable energy storage based on the smart integration of hydrogen and micro gas turbine technologies," *International Journal of Hydrogen Energy,* vol. 47, no. 40, pp. 17505-17525, 2022.

[11] I. H. a. W. J. a. Q. S. a. L. V. Bell, "Pure and Pseudo-pure Fluid Thermophysical Property Evaluation and the Open-Source Thermophysical Property Library CoolProp," *Industrial & Engineering Chemistry Research,* vol. 53, no. 6, pp. 2498-2508, 2014.

[12] IDEALHY, *H2020 IDEALHY (grant agreement no. 278177.*

[13] Hydrogen Council, "Path to Hydrogen Competitiveness: A Cost Perspective," Paris, 2020.

[14] International Energy Agency (IEA), "The Future of Hydrogen," Paris, 2019.

[15] IRENA, "Green Hydrogen Cost Reduction," 2020.

[16] J. R. M. a. T. A. a. G. G. a. J. G. a. A. T. a. M. Torrell, Hidrógeno: Vector energético de una economía descarbonizada, Madrid: Fundación Naturgy, 2020.

[17] U. Lucia, "Overview on fuel cells," *Renewable and Sustainable Energy Reviews,* vol. 30, pp. 164-169, 2014.

[18] S. T. a. K. V. a. F. A. a. E. M. a. M. H. a. A. Ghoniem, "Fuel flexibility, stability and emissions in premixed hydrogen-rich gas turbine combustion: Technology, fundamentals, and numerical simulations," *Applied Energy,* vol. 154, pp. 1020-1047, 2015.

[19] S. M. a. A. Bentebbiche, "Numerical study of blended fuel natural gas-hydrogen combustion in rich/quench/lean combustor of a micro gas turbine," *International Journal of Hydrogen Energy,* vol. 44, no. 29, pp. 15610-15621, 2019.

[20] H.-Y. S. a. C.-R. Liu, "A computational study on the combustion of hydrogen/methane blended fuels for a micro gas turbines," *International Journal of Hydrogen Energy,* vol. 39, no. 27, pp. 15103-15115, 2014.

[21] A. d. G. a. F. R. a. F. C. a. P. Massoli, "A dynamic model of a 100 kW micro gas turbine fuelled with natural gas and hydrogen blends and its application in a hybrid energy grid," *Energy,* vol. 129, pp. 299-320, 2017.

[22] European Turbine Network (ETN), "Hydrogen Gas Turbines: The path towards a zero-carbon gas turbine," 2020.

[23] HYFLEXPOWER-H2020, *HYdrogen as a FLEXible energy storage for a fully renewable European POWER system.*

[24] ROBINSON-H2020, *Smart integRation Of local energy sources and innovative storage for flexiBle, secure and cost-efficIent eNergy Supply ON industrialized islands.*

[25] D. T. S. L. G.-R. Antonio Escamilla, "Exergy Analysis of Green Power-to-Hydrogen Chemical Energy Storage," in *Turbo Expo: Power for Land, Sea, and Air*, 2022.

[26] Xiao, G., Yang, T., Liu, H., Ni, D., Ferrari, M. L., Li, M., Luo, Z., Cen, K., and Ni, M., "Recuperators for micro gas turbines: A review," Applied Energy, vol. 197, pp. 83–99, July 2017.

[27] Traverso, A., 2005, "TRANSEO Code for the Dynamic Performance Simulation of Micro Gas Turbine Cycles,".

[28] di Gaeta, A., Reale, F., Chiariello, F., and Massoli, P., 2017, "A dynamic model of a 100 kW micro gas turbine fuelled with natural gas and hydrogen blends and its application in a hybrid energy grid," Energy, 129(C), pp. 299–320.

[29] Henke, M., Monz, T., and Aigner, M., 2016, "Introduction of a New Numerical Simulation Tool to Analyze Micro Gas Turbine Cycle Dynamics," Journal of Engineering for Gas Turbines and Power, 139(4), 11.

[30] Blotenberg, W., 1993, "A Model for the Dynamic Simulation of a Two-Shaft Industrial Gas Turbine with Dry Low NOx Combustor," Vol. Volume 3C: General of Turbo Expo: Power for Land, Sea, and Air.

[31] Bettocchi, R., Spina, P. R., and Fabbri, F., 1996, "Dynamic Modeling of Single-Shaft Industrial Gas Turbine," Vol. Volume 4: Heat Transfer; Electric Power; Industrial and Cogeneration of Turbo Expo: Power for Land, Sea, and Air.

[32] Gaitanis A, Laterre A, Contino F, De Paepe W. Towards real time transient mGT performance assessment: effective prediction using accurate component modelling techniques. Journal of the Global Power and Propulsion Society. 2022; 6:96-105. doi: https://doi.org/10.33737/jgpps/150359

[33] Bell, I. H., Wronski, J., Quoilin, S., and Lemort, V., 2014, "Pure and pseudo-pure fluid thermophysical property evaluation and the open-source thermophysical property library coolprop," Industrial & Engineering Chemistry Research, 53(6), pp. 2498–2508.

[34] Gaitanis, A., Contino, F., and De Paepe, W. (September 26, 2022). "Real Time MGT Performance Assessment Tool: Comprehensive Transient Behaviour Prediction with Computationally Effective Techniques." ASME. J. Eng. Gas Turbines Power. doi: https://doi.org/10.1115/1.4055785

[35] McDonald, C. F., Recuperator considerations for future higher efficiency microturbines, Applied Thermal Engineering 23 (2003) 1463 - 1487.

[36] Goldstein, L., Hedman, B., Knowles, D., Freedman, S. I., Woods, R., Schweizer T., Gas-Fired Distributed Energy Resource Technology Characterizations, National Renewable Energy Laboratory, Oak ridge, Tennessee, U.S.A., 2003.

[37] McDonald, C. F., Rodgers C., Ceramic recuperator and turbine: The key to achieving a 40 percent efficient microturbine, ASME Conference Proceedings 2005 (2005) 963 - 971.

[38] Lagerstrom, G., Xie M., High performance and cost e ective recuperator for micro-gas turbines, in: ASME Conference Proceedings, ASME paper GT2002-30402, 2002, pp. 1003 - 1007.

[39] Galanti, L., Massardo, A. F., Micro gas turbine thermodynamic and economic analysis up to 500kWe size, Applied Energy 88 (2011) 4795 - 4802.

[40] Mochizuki, K., Shibata, S., Inoue, U., Tsuchiya, T., Sotouchi, H., Okamoto, M., New concept of a micro gas turbine based co-generation package for performance improvement in practical use, in: ASME conference proceedings, ASME Paper PWR2005-50364, 2005, pp. 1305 - 1310.

[41] Delattin, F., Bram, S., Knoops, S., De Ruyck, J., Effects of steam injection on microturbine efficiency and performance, Energy 33 (2008) 241 - 247.

[42] Lee, J. J., Jeon, M. S., Kim, T. S., The influence of water and steam injection on the performance of a recuperated cycle microturbine for combined heat and power application, Applied Energy 87 (2010) 1307 - 1316.

[43] Parente, J., Traverso, A., Massardo, A. F., Micro humid air cycle: Part B - thermoeconomic analysis, in: ASME conference proceedings, ASME paper GT2003-38328, 2003, pp. 231- 239.

[44] Ferrari, M. L., Pascenti, M., Traverso, A. N., Massardo, A. F., Hybrid system test rig: Chemical composition emulation with steam injection, Applied Energy 97 (2012) 809 - 815. Energy Solutions for a Sustainable World - Proceedings of the Third International Conference on Applied Energy, May 16-18, 2011 - Perugia, Italy.

[45] De Paepe, W., Contino, F., Delattin, F., Bram, S., De Ruyck, J., Optimal waste heat recovery in micro gas turbine cycles through liquid water injection, Appl Therm Eng, 70 (1) (2014), pp. 846-856.

[46] Aurelia Turbines Oy, (2018). https://aureliaturbines.com/.

[47] Malkamaki, M., Jaatinen-V¨arri, A., Honkatukia, J., Backman, J., and Larjola, J., 2015. "A High Efficiency Microturbine Concept". In 11th European Conference on Turbomachinery Fluid Dynamics and Thermodynamics, ETC11, March 23-27, Madrid, Spain.

[48] Yanus A. Cengel and Michael A. Boles. Thermodynamics: an engineering approach. ISBN 007-125084-0. McGraw Hill, 2006.

[49] Parente, J., Traverso, A., and Massardo, A.. Micro Humid Air Cycle: Part A – Thermodynamic and technical aspects. In Proceedings of ASME Turbo Expo 2003, number GT2003-38326, pages 221–229, 2003.

[50] Jaatinen-Värri, A., Nerg, J., Uusitalo, A., Ghalamchi, B., Uzhegov, N., Smirnov, A., Sikanen, E., Grönman, A., Backman, J., & Malkamäki, M. "Design of a 400 kW Gas Turbine Prototype." Proceedings of the ASME Turbo Expo 2016: Turbomachinery Technical Conference and Exposition. Volume 8: Microturbines, Turbochargers and Small Turbomachines; Steam Turbines. Seoul, South Korea. June 13–17, 2016. V008T23A007. ASME. https://doi.org/10.1115/GT2016-56444

[51] El-Masri, M. A., A modified, high-efficiency, recuperated gas turbine cycle, Journal of Engineering for Gas Turbines and Power 110 (1988) 233 - 242.

[52] Walsh, P., Fletcher, P.P., Gas turbine performance, Blackwell Science Publications, Oxford, UK, 2004.

[53] Tahan, M., Tsoutsanis, E., Muhammad, M., and Abdul Karim, Z. A., "Performance-based health monitoring, diagnostics and prognostics for condition-based maintenance of gas turbines: A review," *Appl Energy*, vol. 198, pp. 122–144, Jul. 2017, doi: 10.1016/j.apenergy.2017.04.048.

[54] Cruz-Manzo, S., Panov, V., and Zhang, Y., "Gas Path Fault and Degradation Modelling in Twin-Shaft Gas Turbines," *Machines*, vol. 6, no. 4, p. 43, Oct. 2018, doi: 10.3390/MACHINES6040043.

[55] Banihabib, R. and Assadi, M., "Dynamic Modelling And Simulation Of A 100 kW Micro Gas Turbine Running with Blended Methane/Hydrogen Fuel," in *ASME Turbo Expo*, 2022.

[56] Virtanen, P., *et al.*, "SciPy 1.0--Fundamental Algorithms for Scientific Computing in Python," *ArXiv - Computer Science - Mathematical Software*, vol. 17, no. 3, pp. 261–272, Jul. 2019, doi: 10.1038/s41592-019-0686-2.

4. Conclusions and the way forward

4.1. ESR2

ESR 2 is focused on the development of a software tool that enables to analyse the different layouts that can be adopted when it comes to adopting Power-to-Power Energy Storage Systems when using micro-Gas turbine as the mean to produce power. The main conclusions drafted from the different studies and ongoing work done by ESR2 is that Power-to-Power ESS owns a very low round-trip efficiency < 20%. Additionally, the footprint of this systems is tremendously high when considering its design without grid support since the Power-to-Gas systems need to be oversized to cope with the time when renewable energy is not available. However, even though the disadvantages already exposed, this energy storage system remains as the only available solution to store energy at big scale. Moreover, this energy storage system is foreseen as a technology that will allow to increase the share of renewable energy to high percentages.

When it comes to improve the round-trip efficiency of the P2P with mGT, it is foreseen that the round-trip efficiency of the storage system increases to around 40% in the next decades as micro-gas turbine becomes more energy efficient as well as electrolysers.

Next steps for ESR-2 are to do a techno-economic analysis of a P2P with mGT with the aim to characterise the performance and economic parameters of this technology at different geographical locations. This will be carried out with and without grid support.

4.2. ESR3

ESR3, in Chapter 3.2.2, focused on the development of a dynamic model of micro GT that could assist in the development and design of micro GT cycles in future energy production. The model was developed in Python programming language and the calculation methods that were used for each component of the cycle were demonstrated extensively. The main objective was to decrease the complexity and the computation time of the calculations by adopting grey box techniques. The correct and smooth modelling of the performance maps is achieved by using fitting equations and adopting the ones which present the lower RMSE. A viable UA value coupled with a 1-D heat exchanger model ensures the accurate calculation of the outlet temperatures of the Recuperator. Finally, the model was validated at steady state and transient conditions with minor deviations in the key simulated parameters of the engine. A detailed pressure losses calculation using experimental values and a less simplistic control system could assist in the minimisation of the observed deviations.

In Chapter 3.2.3, ESR3 studied the water injection in the High Pressure Compressor outlet of a 2-spool micro GT with a series of simulations performed in Python programming language. The additional amount of water in the cycle increased the overall performance of the engine as the electrical efficiency significantly increased. The maximum potential for water injection was investigated. With a SM_{LPC} as 15% the absolute efficiency increase is 9.57 % at 263 g/s of water mass flow rate. At this specific amount of water, the exergy efficiency reaches 88.75 % which is lower that the indicated maximum value from the literature which makes the design of this water-injected cycle feasible. Next step will be the performance analysis of various water injection schemes in this cycle including the intercooler component to determine which cycle layout is the optimum from a thermodynamic point of view.

The final aim of this study is to plan an efficient control strategy for the 2-spool micro GT at steady state and transient conditions and include this cycle into the micro GT dynamic model which is demonstrated in chapter 3.2.1. The behaviour of key parameters of the cycle such as the Surge Margin (SM) and the Turbine Inlet Temperature (TIT) will be established. Also, the transition between loads will be compared with the T100.

4.3. ESR4

ESR4 examines the operation of a bladeless expander, developed at the University of Genoa, Italy, in reversible mode (compressor mode). The reversible operation revealed several issues related to the rotor and stator design which affected overall performance. A numerical study is conducted to improve the performance of the bladeless compressor by examining the rotor and stator with different parameters. Rotor-only analysis reveals that the axial distance between two disks affects Tesla compressor performance significantly: peak performance is observed at Ekman number 1.6 and DR-2.5, where the optimal Reynolds number is 10, and the disk gap is three times the thickness of the boundary layer. As a result, the DR-2.5 rotor model demonstrated a higher efficiency of over 95.5% for both the outer and inner diameters. As compared to a modified rotor model with DR-2.5 and a disk gap of 0.2 mm, the prototype rotor model demonstrated an 18% reduction in total-to-total efficiency. In this case, if the existing prototype model is replaced with the modified model, the disk and disk gap of the prototype rotor model will be reduced by 33%. As a result of the computational analysis of the rotor-stator and rotor-statorless configuration, it has been revealed that the diffuser must be modified in order to operate the Tesla turbine in reverse mode (as a Tesla compressor). Moreover, results show that the proposed diffuser by Tiwari has better performance in total to static and static to static pressure ratios. The performance and pressure ratio were slightly higher in a volute casing, i.e. statorless configuration. DR-2.5 rotor model with volute casing achieves overall efficiency of 55% at a mass flow rate of 0.40 g/s, while prototype rotor model with diffuser achieves a mass flow rate of 36% at 0.40 g/s.

It is the first-time noise characterization of bladeless turbomachinery is carried out which indicates that the overall sound intensity levels are 98, 87, and 72 dB at 30 krpm, 20 krpm, and 10 krpm. Similarly, at a fixed distance of 0.5 m, sound pressure levels (SPL-dB) of 93 dB, 82 dB, and 67 dB are detected respectively at 30krpm, 20krpm, and 10krpm. The sound pressure level trend increases proportionally with angular speed, whereas the sound pressure level trend decreases quadratically with distance, in accordance with elementary reference models. A final bladeless blower noise result is conducted against a conventional bladed blower as a final step. Tesla blowers have a lower overall acoustic emission at the same rotor tip speed of 27 m/s, with a noise level of 53 (SPL-dB) compared to 83.5 (SPL-dB) for conventional bladed blowers. As a result of frequent blade interaction and pressure fluctuations, the sound is generated at the blade surfaces, but this is minimized in bladeless turbomachinery because there are no blades. According to the results, Tesla's machine is quieter than conventional bladed devices under equivalent operating conditions. Thus, Tesla-type devices would be beneficial in low-noise turbomachinery applications in order to reduce acoustic emissions.

4.4. ESR5

A novel radial compressor is proposed to investigate the advantages of the contra-rotating concept. The main goal is to increase the pressure ratio and improve the adiabatic efficiency, which is usually low for a radial compressor. The single impeller is split into two individual rotors to decrease the high flow turn and, consequently, the related losses.

A comparative study, based on numerical analysis, is conducted in order to assess the performance improvement between this novel CRRC and the baseline configuration. CFD results show that the total-to-total pressure ratio for the CRRC increases by 2.91% while the total-to-total adiabatic efficiency is 1.93% higher. When comparing to the baseline compressor, the low-speed structures that exit the CRRC, have lower energy and smaller shape. This increases the available channel area, reduces the jet-wake effect and improves the adiabatic efficiency of the CRRC. The excessive turn at the exit of the baseline configuration impacts also the exit velocity profile, forming a variable shape. On the contrary, the contra-rotating concept improves the outlet velocity profile and decreases the exit static entropy by almost 40%.

Future work should include an investigation on the effect of distance between rotor 1 and rotor 2 of the CRRC. Off-design simulations should be carried out to generate the compressor characteristic lines. The position of the splitting line of the CRRC should be studied. Finally, the potential advantages of running the two rotors of the CRRC in different rotational speeds should be examined.

4.5. ESR6

In this report a comprehensive overview of the development of a computer model for a micro gas turbine operating in steady-state condition is provided. The code is constructed with lumped assumption for all of the principal gas turbine components, employing thermodynamic equations and empirical correlations to model each components behavior. Proper adaptation parameters were implemented during the modelling which led to a total number of 17 adaptation parameters.

The adaptation process was conducted through two separate courses of optimization, employing a genetic algorithm method. At each course of optimization, a number of parameters were tuned to decrease the error between model predictions and experimental data collected from an micro GT test rig. The results showed high accuracy of the adapted model which proves the suitability of the employed method, to provide an accurate model that can be utilized for condition monitoring purposes. For further improvements, a more flexible correlation for the modelling of the recuperator is expected to improve the accuracy of the predictions even more, however at the expense of increased computational cost.

While artificial intelligence methods were employed inside the physics-based model, another approach will be pursued where the whole engine model will be build utilizing those methods. This will lead to a model with faster response, making it suitable choice for condition monitoring. Instead of the optimization process taken for adaptation, the model will be retrained by optimizing the ANN wights to the new set of data. In general, a model developed by data show good performance within the domain of trained data, however, for extrapolation purposes the accuracy will decrease. In such cases, the physics-based model (presented in this report) could be helpful, and a hybrid approach will provide accurate answers.